

1 2 May, 2020

2

3 Dear Editor,

4

5 We have incorporated all of reviewers' comments in revising our manuscript as explained in our  
6 response to reviewers' comments in the Interactive Discussion.

7 The remaining pages of this document show the changes we have made using the track option in  
8 Word since our last submission.

9 In particular,

- 10 1) we have moved text from the Appendix to the main document to support our case that  
11 the BGC and COU configurations are the preferred simulations to diagnose the feedback  
12 parameters,  
13 2) modified our abstract substantially to report the values of the feedback parameters,  
14 3) moved the figure showing individual model results from the main text to the appendix,  
15 and  
16 4) made the analysis related to transient climate response to cumulative emissions a bit  
17 more prominent.

18

19 Best regards,

20 Vivek Arora (on behalf of all co-authors).

21

22

23

24

25

Carbon-concentration and carbon-climate  
feedbacks in CMIP6 models, and their  
comparison to CMIP5 models

Vivek. K. Arora<sup>1</sup>, Anna Katavouta<sup>2,3</sup>, Richard G. Williams<sup>2</sup>, Chris D. Jones<sup>4</sup>, Victor Brovkin<sup>5,6</sup>,  
Pierre Friedlingstein<sup>7</sup>, Jörg Schwinger<sup>8</sup>, Laurent Bopp<sup>9</sup>, Olivier Boucher<sup>9</sup>, Patricia Cadule<sup>9</sup>,  
Matthew A. Chamberlain<sup>10</sup>, James R. Christian<sup>1</sup>, Christine Delire<sup>11</sup>, Rosie A. Fisher<sup>12,17</sup>, Tomohiro  
Hajima<sup>13</sup>, Tatiana Ilyina<sup>5</sup>, Emilie Joetzjer<sup>11</sup>, Michio Kawamiya<sup>13</sup>, Charles Koven<sup>14</sup>, John P.  
Krasting<sup>15</sup>, Rachel M. Law<sup>16</sup>, David M. Lawrence<sup>17</sup>, Andrew Lenton<sup>10</sup>, Keith Lindsay<sup>17</sup>, Julia  
Pongratz<sup>3,18</sup>, Thomas Raddatz<sup>3</sup>, Roland Séférian<sup>11</sup>, Kaoru Tachiiri<sup>13</sup>, Jerry F. Tjiputra<sup>8</sup> Andy  
Wiltshire<sup>4</sup>, Tongwen Wu<sup>19</sup>, Tilo Ziehn<sup>16</sup>

<sup>1</sup>Canadian Centre for Climate Modelling and Analysis, Environment Canada, University of Victoria,  
Victoria, B.C., V8W 2Y2, Canada  
<sup>2</sup>School of Environmental Sciences, Liverpool University, Liverpool, United Kingdom  
<sup>3</sup>National Oceanography Centre, Liverpool, United Kingdom  
<sup>4</sup>Met Office Hadley Centre, Exeter, United Kingdom  
<sup>5</sup>Max Planck Institute for Meteorology, Bundesstraße 53, 20146 Hamburg, Germany  
<sup>6</sup>CEN, Universität Hamburg, Germany  
<sup>7</sup>College of Engineering, Mathematics and Physical Sciences, University of Exeter, Exeter, EX4 4QF, UK  
<sup>8</sup>NORCE Norwegian Research Centre, Bjerknes Centre for Climate Research, Bergen, Norway  
<sup>9</sup>IPSL, CNRS, Sorbonne Université, Paris, France  
<sup>10</sup>CSIRO Oceans and Atmosphere, Hobart, Tasmania, Australia  
<sup>11</sup>CNRM, Université de Toulouse, Météo-France, CNRS, Toulouse, France  
<sup>12</sup>Centre Européen de Recherche et de Formation Avancée en Calcul Scientifique, (CERFACS). Toulouse,  
France.  
<sup>13</sup>Research Institute for Global Change, Japan Agency for Marine-Earth Science and Technology,  
Yokohama 236-0001, Japan  
<sup>14</sup>Climate and Ecosystem Sciences Division, Lawrence Berkeley National Lab, Berkeley California, USA  
<sup>15</sup>NOAA/Geophysical Fluid Dynamics Laboratory, Princeton, New Jersey, United States of America  
<sup>16</sup>CSIRO Oceans and Atmosphere, Aspendale, Victoria, Australia  
<sup>17</sup>Climate and Global Dynamics Laboratory, National Center for Atmospheric Research, Boulder, CO, USA  
<sup>18</sup>Ludwig-Maximilians University, Munich  
<sup>19</sup>Beijing Climate Center, China Meteorological Administration, 46 Zongguancun Nandajie, Haidian  
District, Beijing, China

**Deleted:** <sup>3...</sup>, Victor Brovkin<sup>5,6</sup>, Pierre Friedlingstein<sup>5...</sup>, Jörg Schwinger<sup>6...</sup>, Laurent Bopp<sup>7...</sup>, Olivier Boucher<sup>97...</sup>, Patricia Cadule<sup>7...</sup>, Matthew A. Chamberlain<sup>8...</sup>, James R. Christian<sup>1</sup>, Christine Delire<sup>9...</sup>, Rosie A. Fisher<sup>10...</sup>, Tomohiro Hajima<sup>11...</sup>, Tatiana Ilyina<sup>4...</sup>, Emilie Joetzjer<sup>9...</sup>, Michio Kawamiya<sup>11...</sup>, Charles Koven<sup>12...</sup>, John P. Krasting<sup>13...</sup>, Rachel M. Law<sup>14...</sup>, David M. Lawrence<sup>15...</sup>, Andrew Lenton<sup>8...</sup>, Keith Lindsay<sup>15...</sup>, Julia Pongratz<sup>54...</sup>, Thomas Raddatz<sup>...</sup>, Roland Séférian<sup>9...</sup>, Kaoru Tachiiri<sup>11...</sup>, Jerry F. Tjiputra<sup>6...</sup>,...Andy Wiltshire<sup>3...</sup>, Tongwen Wu<sup>17...</sup>, Tilo Ziehn<sup>14</sup> ... [1]

**Deleted:** <sup>1</sup>

**Formatted:** Superscript

**Formatted:** Space After: 0 pt

**Formatted** ... [2]

**Deleted:** <sup>3</sup>

**Deleted:** <sup>4</sup>

**Commented [VB1]:** From Feb 2020, I have to add my second affiliation, sorry about mess with affiliation numbers. I can ask my student assistant to clean it up after everyone confirm affiliations.

**Deleted:** <sup>11</sup>  
5

**Deleted:** <sup>6</sup>

**Deleted:** <sup>7</sup>

**Deleted:** <sup>8</sup>

**Deleted:** <sup>9</sup>

**Deleted:** <sup>9</sup>National Center for Atmospheric Research, Boulder, CO, USA and

**Deleted:** <sup>1</sup>

**Deleted:** <sup>2</sup>

**Deleted:** <sup>3</sup>

**Deleted:** <sup>4</sup>

**Deleted:** <sup>5</sup>

**Deleted:** <sup>6</sup>

**Deleted:** <sup>7</sup>

139 **Abstract**

140

141 Results from the fully- and biogeochemically-coupled simulations in which CO<sub>2</sub> increases at a rate  
 142 of 1% per year (1pctCO<sub>2</sub>) from its pre-industrial value are analyzed to quantify the magnitude of  
 143 carbon-concentration and carbon-climate feedback parameters which measure the response of  
 144 ocean and terrestrial carbon pools to changes in atmospheric CO<sub>2</sub> concentration and the resulting  
 145 change in global climate, respectively. The results are based on eleven comprehensive Earth  
 146 system models from the most recent (sixth) Coupled Model Intercomparison Project (CMIP6) and  
 147 compared with eight models from the fifth CMIP (CMIP5). The strength of the carbon-  
 148 concentration feedback is of comparable magnitudes over land (mean ± standard deviation =  
 149 0.97±0.40 PgC ppm<sup>-1</sup>) and ocean (0.79±0.07 PgC ppm<sup>-1</sup>) while the carbon-climate feedback over  
 150 land (-45.1±50.6 PgC °C<sup>-1</sup>) is about three times larger than over ocean (-17.2±5.0 PgC °C<sup>-1</sup>). The  
 151 strength of both feedbacks is an order of magnitude more uncertain over land than over ocean  
 152 as has been seen in existing studies. These values and their spread from eleven CMIP6 models  
 153 have not changed significantly compared to CMIP5 models. The absolute values of feedback  
 154 parameters are lower for land with models that include a representation of nitrogen cycle. The  
 155 transient climate response to cumulative emissions (TCRE) from the eleven CMIP6 models  
 156 considered here is 1.77±0.36 °C EgC<sup>-1</sup> and is similar to that found in CMIP5 models (1.63±0.48 °C  
 157 EgC<sup>-1</sup>) but with somewhat reduced model spread. The expressions for feedback parameters  
 158 based on the fully- and biogeochemically-coupled configurations of the 1pctCO<sub>2</sub> simulation are  
 159 simplified when the small temperature change in the biogeochemically-coupled simulation is  
 160 ignored. Decomposition of the terms of these simplified expressions for the feedback parameters  
 161 are used to gain insight into the reasons for differing responses among ocean and land carbon  
 162 cycle models.

163

164

Deleted: -,

Deleted: , and radiatively-

Deleted: two

Deleted: characterize the coupled carbon-climate system. These feedback parameters quantify

Deleted: The comparison of model results from two CMIP phases shows that, for both land and ocean, the model mean values of the feedback parameters and their multi-model spread

Deleted: s

Deleted: across the two CMIP phases

Deleted: somewhat higher than fifteen

Deleted: ased on a published study

Deleted: The sensitivity of feedback parameters to the three different ways in which they may be calculated is shown and, consistent with existing studies, the most relevant definition is that calculated using results from

Deleted: . Based on these two simulations

Deleted: expressions for the feedback parameters are obtained

Deleted: allows identification of

184

## 185 1. Introduction

186

187 The Earth system responds to the perturbation of atmospheric CO<sub>2</sub> concentration ([CO<sub>2</sub>]), caused  
188 by anthropogenic emissions of CO<sub>2</sub> or any other forcing, via changes in its physical climate. The  
189 changes in the globally-averaged temperature, and the subsequent changes in other components  
190 of physical climate, due to changes in radiative forcing associated with [CO<sub>2</sub>] are larger than what  
191 would be expected from the blackbody response alone. The reason for this is that the positive  
192 feedbacks associated with various aspects of the climate system enhance the initial warming.  
193 These primarily include changes in atmospheric water vapor, tropospheric lapse rate, surface  
194 albedo resulting from ice and snow, and clouds (Hansen et al., 1984; Gregory et al., 2009a; Ceppi and  
195 Gregory, 2017).

196

197 The biogeochemical cycling of carbon is also affected by changes in [CO<sub>2</sub>] and the physical  
198 climate. In fact, changes in both the physical climate and the biogeochemical carbon cycle affect  
199 each other through multiple feedbacks. The response of the Earth's carbon cycle for both land  
200 and ocean components has been characterized in terms of carbon-concentration and carbon-  
201 climate feedback parameters which quantify their response to changes in [CO<sub>2</sub>] and the physical  
202 climate, respectively (Friedlingstein et al., 2006; Arora et al., 2013). The carbon-concentration  
203 feedback ( $\beta$ ) quantifies the response of the carbon cycle to changes in [CO<sub>2</sub>] and is expressed in  
204 units of carbon uptake or release per unit change in [CO<sub>2</sub>] (PgC ppm<sup>-1</sup>). The carbon-climate  
205 feedback ( $\gamma$ ) quantifies the response of the carbon cycle to changes in physical climate and is

**Deleted:** its

**Deleted:** fossil fuel and land use change

**Deleted:** both

**Deleted:** and the biogeochemical carbon cycle

**Field Code Changed**

**Formatted:** Font: (Default) Calibri

**Deleted:** (Hansen et al., 1984; Gregory et al., 2009)

**Formatted:** Font: (Default) +Body (Calibri), 11 pt, Check spelling and grammar

**Deleted:** C

**Deleted:** The surface-atmosphere exchange of CO<sub>2</sub> over both land and ocean is modulated by the changes in physical climate and [CO<sub>2</sub>], and the resulting changes in [CO<sub>2</sub>] modulates the physical climate, among other climate forcings. ¶

**Field Code Changed**



217 expressed in units of carbon uptake or release per unit change in global mean temperature (PgC  
218 °C<sup>-1</sup>). The changes in physical climate, in this framework, are expressed simply in terms of  
219 changes in global mean near surface air temperature although, of course, the carbon cycle also  
220 responds to other aspects of changes in climate (in particular precipitation over land and  
221 circulation changes in the ocean). The assumption is that the effect of other aspects of changes  
222 in climate on the carbon cycle can be broadly expressed in terms of changes in near surface air  
223 temperature. These feedback parameters can be calculated from Earth system model (ESM)  
224 simulations globally, separately over land and ocean, regionally, or over individual grid cells which  
225 makes somewhat more sense over land than over ocean, to investigate their geographical  
226 distribution (Yoshikawa et al., 2008; Boer and Arora, 2010; Tjiputra et al., 2010; Roy et al., 2011;  
227 Friedlingstein et al., 2006; Arora et al., 2013). The feedback analysis has shown that the carbon-  
228 concentration feedback is negative from the atmosphere's perspective. That is, an increase in  
229 [CO<sub>2</sub>] leads to an increased carbon uptake by land and ocean which leads to a decrease in [CO<sub>2</sub>]  
230 thereby slowing CO<sub>2</sub> accumulation in the atmosphere. The carbon-climate feedback, in contrast,  
231 has been shown to be positive in ESM simulations (at the global scale) from the atmosphere's  
232 perspective since an increase in temperature decreases the capacity of land and ocean to take  
233 up carbon, thereby contributing to a further increase in atmospheric CO<sub>2</sub>.

235 The carbon-concentration and carbon-climate feedback parameters serve several purposes.  
236 First, these feedback parameters allow comparison of models in a simple and straightforward  
237 manner despite their underlying complexities and different model structures. Inter-model  
238 comparisons offer several benefits, including common standards and experiment protocol,

Deleted: (

Deleted: )

Field Code Changed

Deleted: ,

Deleted: of course,

Deleted: several

244 coordination, and documentation that facilitates the distribution of model outputs and the  
 245 characterization of the mean-model response (Eyring et al., 2016), as has been shown for  
 246 multiple model intercomparison projects (MIPs). Second, they allow the quantification of the  
 247 contribution of the two feedback processes to allowable anthropogenic emissions for a given CO<sub>2</sub>  
 248 pathway. For example, (Arora et al., 2013) and (Gregory et al., 2009) showed that the  
 249 contribution of the carbon-concentration feedback to allowable diagnosed emissions is about 4-  
 250 4.5 times larger than the carbon-climate feedback. Third, they allow the comparison of feedbacks  
 251 between climate and the carbon cycle to other feedbacks operating in the climate system as was  
 252 done by Gregory et al. (2009). Fourth, the feedback parameters can be considered as emergent  
 253 properties of the coupled carbon-cycle climate system which can potentially be constrained by  
 254 observations as Wenzel et al. (2014) attempted for the carbon-climate feedback parameter over  
 255 land.

256  
 257 Here, we build on the work done in earlier studies that compared the strength of the carbon-  
 258 concentration and carbon-climate feedback in coupled general circulation models with land and  
 259 ocean carbon cycle components. Friedlingstein et al. (2006) (hereafter F06) reported the first  
 260 such results from the Coupled Climate Carbon Cycle Models Intercomparison Project (C<sup>4</sup>MIP).  
 261 Arora et al. (2013) (hereafter A13) compared the strength of the carbon-concentration and  
 262 carbon-climate feedbacks from models participating in the fifth phase of the Coupled Model  
 263 Intercomparison Project (CMIP5, <http://cmip-pcmdi.llnl.gov/cmip5/forcing.html>, (Taylor et al.,  
 264 2012)). The A13 study found that the strength of the two feedbacks was weaker and the spread  
 265 between models was smaller in their study than in F06. However, the results from these two

Field Code Changed

Formatted: Font: (Default) Calibri, 12 pt, Do not check spelling or grammar

Field Code Changed

Field Code Changed

Field Code Changed

Deleted: (

Deleted: .,

Deleted: (

Deleted: .,

Field Code Changed

Deleted: (

Deleted: .,

Field Code Changed

Deleted: (

Deleted: .,

Deleted: While this comparison is useful, the primary caveat when

Deleted: comparing

Deleted: between

278 studies are not directly comparable because of several reasons. The results from the F06 study  
279 were based on the SRES A2 emissions scenario, while those in the A13 study were based on the  
280 1% per year increasing CO<sub>2</sub> experiment in which the atmospheric CO<sub>2</sub> concentration increases  
281 from its pre-industrial value of around 285 ppm until it quadruples over a 140-year period  
282 (referred to as the 1pctCO2 experiment in the framework of the Coupled Model Intercomparison  
283 Project, CMIP). The absolute values of the feedback parameters are known to be dependent on  
284 the state of the system, the timescale of forcing (i.e. underlying emissions/concentration  
285 scenario) and the approach used to calculate them (Plattner et al., 2008; Zickfeld et al., 2011;  
286 Hajima et al., 2014; Gregory et al., 2009; Boer and Arora, 2010). The varying approaches  
287 employed over the past decade have made the cross-comparison of feedbacks among the studies  
288 and different generations of Earth System Models difficult.

289  
290 In order to address the diversity of approaches to diagnose climate carbon cycle feedbacks, and  
291 to promote a robust standard moving forward, the C<sup>4</sup>MIP community has endorsed a framework  
292 of tiered experiments (Jones et al., 2016) that builds upon the core pre-industrial control and  
293 1pctCO2 experiments performed as part of the CMIP DECK (Diagnostic, Evaluation and  
294 Characterization of Klima) experiments (Eyring et al., 2016). Here, we compare carbon-  
295 concentration and carbon-climate feedbacks from models participating in the C<sup>4</sup>MIP (Jones et al.,  
296 2016) contribution to the sixth phase of CMIP (CMIP6, Eyring et al., 2016). To maintain continuity  
297 and consistency, feedback parameters are derived from the 1pctCO2 experiments as was done  
298 in A13. The 1pctCO2 experiment is a DECK experiment in the CMIP6 framework. All participating

**Deleted:** is that their results are based on different scenarios

**Field Code Changed**

**Formatted:** Font: (Default) Calibri, 12 pt

**Deleted:** (Jones et al., 2016, 201)

**Formatted:** Font: (Default) +Body (Calibri), 11 pt, Check spelling and grammar

**Field Code Changed**

**Deleted:** preindustrial

**Field Code Changed**

**Field Code Changed**

302 modelling groups are expected to perform DECK experiments to help document basic  
303 characteristics of models across different phases of CMIP (Eyring et al., 2016).

Field Code Changed

304

## 305 2. Feedbacks metrics in the coupled climate-carbon system

306

307 We largely follow the climate carbon cycle feedbacks framework presented in A13 (which in turn  
308 was built on F06) but with some additional modifications that are explained below. Only the  
309 primary equations are presented here while the bulk of the framework is summarized in the  
310 Appendix for completeness. We also provide some history of how the carbon feedbacks analysis  
311 reached its current stage.

312

313 Carbon feedbacks analysis is traditionally based on simulations run with fully-, radiatively-, and  
314 biogeochemically-coupled model configurations of an Earth system model. The objective of these  
315 simulations is to isolate feedbacks discussed above. In a biogeochemically-coupled simulation  
316 (referred to here as the BGC simulation), biogeochemical processes over land and ocean respond  
317 to increasing atmospheric CO<sub>2</sub> while the radiative transfer calculations in the atmosphere use a  
318 CO<sub>2</sub> concentration that remains at its pre-industrial value. Small climatic changes occur in the

Deleted: preindustrial

319 BGC simulation due to changes in evaporative (or latent heat) flux resulting from stomatal closure  
320 over land (associated with increasing [CO<sub>2</sub>]), changes in vegetation structure, and changes in  
321 vegetation coverage and composition (in models which dynamically simulate competition  
322 between their plant functional types) all of which affect latent and sensible heat fluxes at the  
323 land surface. In a radiatively-coupled simulation (referred to here as the RAD simulation)

325 increasing atmospheric CO<sub>2</sub> affects the radiative transfer processes in the atmosphere and hence  
 326 climate but not the biogeochemical processes directly over land and ocean, for which the ~~pre-~~  
 327 industrial value of atmospheric CO<sub>2</sub> concentration is prescribed. In a fully-coupled simulation  
 328 (referred to here as the COU simulation) both the biogeochemical and the radiative processes  
 329 respond to increasing CO<sub>2</sub>.

Deleted: preindustrial

330  
 331 Following the F06 methodology which uses time-integrated fluxes (which are the same as the  
 332 changes in carbon pool sizes), the changes in land ( $L$ ) or ocean ( $O$ ) carbon pools ( $\Delta C_X, X = L, O$ )  
 333 can be expressed using three equations corresponding to the BGC, RAD, and COU experiments,  
 334 as shown in equation (1) (see also the Appendix).

335  
 336 Radiatively coupled simulation  $\Delta C_X^+ = \int F_X^+ dt = \gamma_X T^+$  (1a)

337 Biogeochemically coupled simulation  $\Delta C_X^* = \int F_X^* dt = \beta_X c' + \gamma_X T^*$  (1b)

338 Fully coupled simulation  $\Delta C_X' = \int F_X' dt = \beta_X c' + \gamma_X T'$  (1c)

339  
 340 where  $F^+$ ,  $F^*$ , and  $F'$  are the CO<sub>2</sub> flux changes (PgC year<sup>-1</sup>),  $\Delta C_X^+$ ,  $\Delta C_X^*$ , and  $\Delta C_X'$  the changes in  
 341 global carbon pools (PgC), and  $T^+$ ,  $T^*$ , and  $T'$  the temperature changes (°C) in the RAD, BGC, and  
 342 COU simulations, respectively, and the subscript  $X = L, O$  refers to either the land or ocean  
 343 model components.  $c'$  is the change in [CO<sub>2</sub>]. Here and elsewhere uppercase  $C$  is used to denote  
 344 pools and lowercase  $c$  is used to denote atmospheric CO<sub>2</sub> concentration, [CO<sub>2</sub>]. All changes are  
 345 defined relative to a pre-industrial equilibrium state represented by the pre-industrial control  
 346 simulation. In the context of a specified-concentration simulation (the 1pctCO2 experiment in

Deleted: .

349 our case),  $c'$  is the same in BGC and COU simulations. There is no  $\beta_X c'$  term in the RAD simulation  
350 since the biogeochemistry sees pre-industrial value of  $[\text{CO}_2]$  although  $T^+$  is a function of  
351 increasing  $c'$  that is seen only by the radiative transfer calculations.

Deleted: and therefore  $c' = 0$

352  
353 These equations assume linearization of the globally integrated surface-atmosphere  $\text{CO}_2$  flux (for  
354 land and ocean components) in terms of global mean temperature and  $[\text{CO}_2]$  change (compared  
355 to a pre-industrial control run) and serve to define the carbon-concentration ( $\beta_X$ ) and carbon-  
356 climate ( $\gamma_X$ ) feedback parameters. A similar set of equations can be written that define the  
357 instantaneous values of the feedback parameters and is based on fluxes rather than their time-  
358 integrated values (see equations A4 and A5 in the Appendix). Both the time-integrated flux and  
359 instantaneous flux-based versions of the feedback parameters evolve over time in an experiment  
360 as shown in A13.

Deleted: a

Deleted:

361  
362 There are several different ways in which the feedbacks ( $\beta_X$  and  $\gamma_X$ ) in a coupled climate and  
363 carbon cycle system may be evaluated: 1) the experiments may use specified (concentration-  
364 driven) or freely evolving (emissions-driven)  $[\text{CO}_2]$ , 2) any two of the three configurations of an  
365 experiment (COU, RAD, and BGC) may be used to calculate the two feedback parameters, and 3)  
366 the experiment may be based on an idealized scenario (like the 1pctCO2 experiment) or a more  
367 realistic emissions scenario. In addition, the small temperature change in the BGC simulation,  $T^*$ ,  
368 may be ignored, and other external forcings such as nitrogen (N) deposition, or land use change,  
369 which directly affect carbon fluxes may or may not be taken into account. The original framework  
370 proposed by F06 used COU and BGC versions (referred to as coupled and uncoupled in the F06

374 study) of an emissions-driven simulation for the SRES A2 scenario. The F06 framework assumed  
375 that the small temperature change in the BGC simulation can be ignored. A13 used BGC and RAD  
376 versions of the 1pctCO2 experiment in which the evolution of [CO<sub>2</sub>] is specified and took into  
377 account the small global mean temperature change in the BGC simulation.

378

379 With regard to the use of concentration-driven versus emissions-driven simulations, Gregory et  
380 al. (2009) recommended the use of specified concentration simulations, which ensures  
381 consistency of [CO<sub>2</sub>] across models, and this recommendation has now been adopted since  
382 CMIP5. C<sup>4</sup>MIP has also adopted the use of the 1pctCO2 simulation, i.e., an idealized scenario is  
383 preferred over a more realistic scenario. The 1pctCO2 experiment provides an ideal experiment  
384 to compare carbon-climate interactions across models as the experiment does not include the  
385 confounding effects of other climate forcings (including land use change, non-CO<sub>2</sub> greenhouse  
386 gases, and aerosols) and is a CMIP DECK experiment, as mentioned earlier.

387

388 Using equation (1) as an example, Table 1 shows how any two combinations of the three  
389 configurations of an experiment can be used to calculate the values of the two feedback  
390 parameters. The A13 study showed that under the assumption of a linear system and if the  
391 conditions  $F' = F^+ + F^*$  and  $T' = T^+ + T^*$  are met, i.e. if the sum of flux and temperature changes  
392 in the RAD and BGC simulations is the same as that in the COU simulation, then all approaches  
393 yield exactly the same solution. However, this is not the case because of the non-linearities

394 involved (Gregory et al., 2009b; Zickfeld et al., 2011; Schwinger et al., 2014).

395

Deleted:

Deleted: . This recommendation was also made by Gregory et al. (2009).

Deleted: (see also

Field Code Changed

Formatted: Font: (Default) Calibri, 12 pt

Deleted: (Schwinger et al., 2014; Zickfeld et al., 2011)

Formatted: Font: (Default) +Body (Calibri), 11 pt, Check spelling and grammar

401 The use of BGC and RAD simulations that have only biogeochemistry or radiative forcing  
 402 responding to increases in  $[\text{CO}_2]$  to find the feedback parameters is attractive since these  
 403 simulations were designed to isolate the feedbacks. In the RAD simulation (whose purpose is to  
 404 quantify the carbon-climate feedback,  $\gamma_X$ ) the pre-industrial global carbon pools for both land  
 405 and ocean typically decrease in response to an increase in global temperature (hence the positive  
 406 carbon-climate feedback and the negative value of  $\gamma_X$ ). Consequently, negative values of  $\gamma_X$   
 407 (positive carbon-climate feedback) are obtained when using the RAD-BGC and RAD-COU  
 408 approaches (see Table 1). If, however,  $\gamma_X$  is determined using the BGC and COU simulations in  
 409 both of which the globally-summed carbon pools for land and ocean are increasing in response  
 410 to increasing  $[\text{CO}_2]$ , the calculated value of  $\gamma_X$  is different than that obtained using the RAD-BGC  
 411 and RAD-COU approaches. In the ocean, the RAD simulation mainly measures the loss of near-  
 412 surface carbon owing to warming of the surface ocean layer (Schwinger et al., 2014). The RAD  
 413 simulation misses the suppression of carbon drawdown to the deep ocean due to weakening  
 414 ocean circulation, because there is no buildup of a strong carbon gradient from the surface to  
 415 the deep ocean in contrast to the BGC and COU simulations. Therefore, the absolute value of  $\gamma_X$   
 416 for ocean is smaller (less negative) when calculated using the RAD-BGC and RAD-COU approaches  
 417 compared to the BGC-COU approach (Schwinger et al., 2014). Over land, in the RAD simulation  
 418 carbon is lost in response to increasing temperatures primarily due to an increase in  
 419 heterotrophic respiration. However, an increase in temperature also potentially increases  
 420 photosynthesis at high latitudes, and this increase compensates for carbon lost due to increased  
 421 heterotrophic respiratory losses, especially in the presence of continuously increasing  $[\text{CO}_2]$  seen  
 422 in the COU configuration. Therefore  $\gamma_X$  value for land calculated using RAD-BGC and RAD-COU

**Deleted:** BGC-COU approach, then  $\gamma_X$  is calculated using

**Deleted:** . As a result

**Field Code Changed**

**Deleted:** simulation

**Field Code Changed**



426 approaches may be higher or lower than that calculated using the BGC-COU approach. These are  
427 some mechanisms that lead to non-linearities. Since the ongoing climate change (predominantly  
428 caused by increasing [CO<sub>2</sub>]) is best characterized by the COU simulation, it can be argued that  
429 feedback parameters are more representative when calculated using the BGC-COU approach.  
430 Here, we propose to use the COU and BGC configurations of an experiment as the standard set  
431 from which to calculate the feedback parameters as recommended in the C<sup>4</sup>MIP protocol (Jones  
432 et al., 2016). However, we also quantify the values of feedback parameters when using the RAD  
433 simulation for comparison. The calculated values of the carbon-concentration feedback  
434 parameter ( $\beta_X$ ) in contrast, are less sensitive to the approach used as shown in A13.

435  
436 There is no broad consensus on whether temperature change in the BGC simulation should be  
437 assumed to be zero ( $T^* = 0$ ) as standard practice when calculating the strengths of the  
438 feedbacks, as done in F06. While the globally-averaged value of  $T^*$  is an order of magnitude  
439 smaller than  $T'$ , the spatial pattern of  $T^*$  is quite different from that of  $T'$ . The spatial pattern of  
440 temperature change in the COU simulation ( $T'$ ) is dominated by radiative forcing of increased  
441 [CO<sub>2</sub>] with greater warming at high latitudes and over land than over ocean. In contrast, the  
442 spatial pattern of temperature change in the BGC simulation ( $T^*$ ) is determined primarily by  
443 reduction in latent heat flux associated with stomatal closure as [CO<sub>2</sub>] increases which reduces  
444 transpiration from vegetation (Bounoua et al., 1999; Ainsworth and Long, 2005). This process  
445 leads to a much more spatially variable pattern of temperature change (than  $T'$ ) and the  
446 associated changes in precipitation patterns due to soil moisture-atmosphere feedbacks  
447 (Chadwick et al., 2017; Skinner et al., 2017). The difference in spatial patterns of temperature

Deleted:

Field Code Changed

and precipitation change in the RAD versus the COU simulation is another reason that the values of the carbon-climate feedback ( $\gamma_X$ ) depend on the simulation used, and this is another pathway for non-linearities to occur. A complete analysis of the effect of differences in spatial patterns of climate change and the carbon state on the calculated value of  $\gamma_X$  when using the RAD versus the COU simulation, and if or not the assumption of  $T^* = 0$  should be a standard practice, is beyond the scope of this study but remains a topic for additional scientific investigation. In the

interim, we report here values of  $\beta_X$  and  $\gamma_X$  both by considering  $T^*$  and by ignoring it (i.e.  $T^* = 0$ ) when using the BGC-COU approach.

Deleted: by explicitly

Deleted: but also assuming

Deleted: .

Following Table 1, when using results from the BGC and the COU configurations of a specified-concentration experiment the values of the feedback parameters are written as

Deleted: versions

$$\beta_X = \frac{1}{c'} \left( \frac{\Delta C_X^* T' - \Delta C_X' T^*}{T' - T^*} \right) \quad (2)$$

$$\gamma_X = \frac{\Delta C_X' - \Delta C_X^*}{T' - T^*} \quad (3)$$

Equations (2) and (3) may be rearranged to explicitly calculate the effect of the  $T^* = 0$  assumption on calculated values of feedback parameters, as shown in equations (4) and (5). Here, the  $T^*$  term is retained only in the second part of the equations whose contribution becomes zero when  $T^*$  is ignored.

$$\beta_X = \frac{\Delta C_X^*}{c'} + \frac{1}{c'} \left[ \frac{(\Delta C_X' - \Delta C_X^*) T^*}{(T' - T^*)} \right] \quad (4)$$

$$\gamma_X = \frac{\Delta C_X' - \Delta C_X^*}{T'} + \frac{(\Delta C_X' - \Delta C_X^*) T^*}{T' (T' - T^*)} \quad (5)$$

475

476 Finally, in regards to other external forcings such as nitrogen (N) deposition that directly affect  
477 carbon fluxes, the C<sup>4</sup>MIP protocol for CMIP6 (Jones et al., 2016) recommended performing  
478 additional simulations for BGC and COU versions of the 1pctCO<sub>2</sub> experiment with time varying N  
479 deposition in addition to their standard versions which keep N deposition rates at their pre-  
480 industrial level. Simulations with N deposition can only be performed for models that explicitly  
481 model the N cycle and its interactions with the carbon (C) cycle. The rationale for recommending  
482 increasing N deposition, in conjunction with temperature and CO<sub>2</sub> increase, is to be able to  
483 quantify the response of feedback parameters to this third forcing. However, here we restrict  
484 ourselves to the traditional analysis that considers the climate and CO<sub>2</sub> forcings only. We do  
485 highlight, however, which models include coupled C-N cycle interactions over land. Analysis of  
486 runs with N deposition forcing is left for future studies.

487

## 488 2.1. Reasons for differences in feedback parameters among models

489

490 As shown later in this paper, the contribution of the second term involving  $T^*$  in expressions for  
491 the carbon-concentration ( $\beta_X$ ) and carbon-climate ( $\gamma_X$ ) feedback parameters (in equations 4 and  
492 5, when using the BGC-COU approach) is around 1% to 5%. This allows the reasons for differences  
493 in the feedback parameters to be investigated across models as the expressions for the feedback  
494 parameters can be simplified in terms of the changes in the sizes of carbon pools ( $\Delta C'_X$  and  $\Delta C^*_X$ ),  
495 the temperature change in the COU simulation ( $T'$ ) and the specified change in [CO<sub>2</sub>] ( $c'$ ) as  
496 follows.

Deleted: to investigate

498

$$\beta_X \approx \frac{\Delta C_X^*}{c'} \quad (6)$$

$$\gamma_X \approx \frac{\Delta C_X' - \Delta C_X^*}{T'} \quad (7)$$

501

### 502 2.1.1.1 Land

503

504 Over land, equations (6) and (7) can be expanded to investigate, firstly, the contributions from  
 505 changes in live vegetation pool ( $\Delta C_V$ ) and dead litter plus soil carbon pools ( $\Delta C_S$ ), to the strength  
 506 of the feedback parameters, since  $\Delta C_L = \Delta C_V + \Delta C_S$ . Secondly, equation (6) can be further  
 507 decomposed to gain insight into the reasons for differences across models, in a manner similar  
 508 to Hajima et al. (2014).

$$\begin{aligned} \beta_L \approx \frac{\Delta C_L^*}{c'} = \frac{\Delta C_V^* + \Delta C_S^*}{c'} &= \left( \frac{\Delta C_V^*}{\Delta NPP^*} \frac{\Delta NPP^*}{\Delta GPP^*} \frac{\Delta GPP^*}{c'} \right) + \left( \frac{\Delta C_S^*}{\Delta R_h^*} \frac{\Delta R_h^*}{\Delta LF^*} \frac{\Delta LF^*}{c'} \right) \\ &= \tau_{veg\Delta} \cdot CUE_{\Delta} \cdot \frac{\Delta GPP^*}{c'} + \tau_{soil\Delta} \frac{\Delta R_h^*}{\Delta LF^*} \frac{\Delta LF^*}{c'} \end{aligned} \quad (8)$$

$$\gamma_L \approx \frac{\Delta C_L' - \Delta C_L^*}{T'} = \frac{\Delta C_V' - \Delta C_V^*}{T'} + \frac{\Delta C_S' - \Delta C_S^*}{T'} \quad (9)$$

512 The superscript \* in equation (8) implies that the terms are calculated here using the BGC version  
 513 of the 1pctCO2 experiment. In equation (8),  $\Delta NPP$  and  $\Delta GPP$  represent the change in net and  
 514 gross primary productivity (GPP),  $\Delta LF$  the change in litterfall flux, and  $\Delta R_h$  the change in  
 515 heterotrophic respiration, compared to the pre-industrial control experiment. The multiplicative  
 516 terms in equation (8) do indeed have physical meaning although they are based on change in the

Deleted: ¶

Deleted: ,

Field Code Changed

Deleted: (

Deleted: preindustrial

Deleted: some

522 magnitude of quantities as opposed to their absolute magnitudes. We note here explicitly that  
 523 as such, these terms cannot be compared directly to the terms which are based on absolute  
 524 magnitudes.

525 The term  $\frac{\Delta NPP}{\Delta GPP}$  (fraction) is the fraction of GPP (above its pre-industrial value) that is turned into  
 526 NPP after autotrophic respiratory losses are taken into account. We use the term carbon use  
 527 efficiency (CUE) but subscripted by  $\Delta$  ( $CUE_{\Delta}$ ) to represent  $\frac{\Delta NPP}{\Delta GPP}$ . The subscripted  $\Delta$  allows  $CUE_{\Delta}$   
 528 to be differentiated from  $CUE$  as used in the existing literature (Choudhury, 2000) which  
 529 represents the fraction of absolute GPP that is converted to NPP rather than its change over some  
 530 time period, as well as the point that we consider globally-integrated rather than locally-derived  
 531 quantities. Similarly, the term  $\frac{\Delta C_V}{\Delta NPP}$  represents a measure of turnover or residence timescale of  
 532 carbon in the vegetation pool ( $\tau_{veg\Delta}$ , years). The term  $\frac{\Delta GPP}{c'}$  ( $\text{PgC yr}^{-1} \text{ ppm}^{-1}$ ) is a measure of the  
 533 strength of the globally-integrated  $\text{CO}_2$  fertilization effect. However, in the models that  
 534 dynamically simulate changes in vegetation cover, the effect of changes in vegetation coverage is  
 535 implicitly included in this term. The term  $\frac{\Delta C_S}{\Delta R_h}$  is a measure of the average residence time of carbon  
 536 in the dead litter and soil carbon pools ( $\tau_{soil\Delta}$ , years). However, as with CUE, this quantity cannot  
 537 be compared directly to the residence time of carbon in the litter plus soil carbon pool calculated  
 538 using the absolute values of  $C_S$  and  $R_h$ . Nor can it be compared to the changes in carbon residence  
 539 time due to the “false priming effect” associated with the increase in NPP inputs, as  $[\text{CO}_2]$   
 540 increases, into the dead carbon pools (Koven et al., 2015).  $\frac{\Delta R_h}{\Delta LF}$  (fraction) is a measure of the  
 541 increase in heterotrophic respiration per unit increase in litterfall rate, and  $\frac{\Delta LF}{c'}$  ( $\text{PgC yr}^{-1} \text{ ppm}^{-1}$ )

Field Code Changed

indicates global increase in litterfall rate per unit increase in  $\text{CO}_2$ , which in principle, should be close to the change in net primary productivity per unit increase in  $\text{CO}_2$ ,  $\left(CUE_{\Delta} \frac{\Delta GPP}{c'}\right)$ . Comparison of these terms across models can potentially yield insight into the reasons for large differences in land carbon uptake across models.

546

## 2.1.2 Ocean

548

Assuming changes in biological organic carbon inventory are small, the change in the ocean carbon inventory,  $\Delta C_O$ , is defined by an integral of the change in the dissolved inorganic carbon,  $\Delta DIC$ , and density over the ocean volume,

$$\Delta C_O = 12 \text{ gC mol}^{-1} \int_V \Delta DIC \, dV \times 10^{-15} \quad (10)$$

where  $\Delta C_O$  is in PgC, the ocean dissolved inorganic carbon,  $DIC$  in  $\text{mol m}^{-3}$  and the ocean volume  $V$  in  $\text{m}^3$ , and the multiplier  $10^{-15}$  converts g to Pg of carbon.

555

To gain insight into how the ocean carbon distribution is controlled, the ocean dissolved inorganic carbon,  $DIC$ , may be defined in terms of separate carbon pools (Ito and Follows, 2005; Williams and Follows, 2011; Lauderdale et al., 2013; Schwinger and Tjiputra, 2018):

$$\begin{aligned} DIC &= DIC_{preformed} + DIC_{regenerated} \\ &= DIC_{sat} + DIC_{disequilib} + DIC_{regenerated} \end{aligned} \quad (11)$$

Deleted: T

Formatted: Font: Italic

Field Code Changed

561 where the preformed carbon,  $DIC_{preformed}$ , is the amount of carbon in a water parcel when in  
 562 the mixed layer at the time of subduction, and the regenerated carbon,  $DIC_{regenerated}$ , is the  
 563 amount of dissolved inorganic carbon accumulated below the mixed layer due to biological  
 564 regeneration of organic carbon. The preformed carbon is affected by the carbonate chemistry  
 565 and ocean physics. To gain further insight into how close the ocean is to an equilibrium with the  
 566 atmosphere, the preformed carbon,  $DIC_{preformed}$ , is further split into saturated,  $DIC_{sat}$ , and  
 567 disequilibrium,  $DIC_{disequib}$  components. The saturated component represents the  
 568 concentration in surface water fully equilibrated with the contemporary atmospheric  $CO_2$   
 569 concentration. The disequilibrium component represents the extent that surface water is  
 570 incompletely equilibrated before subduction, which is affected by the strength of the ocean  
 571 circulation altering the residence time in the mixed layer and the ocean ventilation rate. Each of  
 572 these components is affected by the increase in atmospheric  $CO_2$  and the changes in climate.

573

574 The change in the global ocean carbon inventory,  $\Delta C_O$ , relative to the ~~pre-industrial~~ may then be  
 575 related to the global volume integral of the change in each of these DIC pools,

Deleted: preindustrial

$$\begin{aligned}
 \Delta C_O &= \Delta C_{preformed} + \Delta C_{regenerated} \\
 &= \Delta C_{sat} + \Delta C_{disequib} + \Delta C_{regenerated}
 \end{aligned}
 \tag{12}$$

577 where  $\Delta C_{preformed}$  is the preformed carbon inventory,  $\Delta C_{sat}$  is the saturated carbon inventory,  
 578  $\Delta C_{disequib}$  is the disequilibrium carbon inventory and  $\Delta C_{regenerated}$  is the regenerated carbon  
 579 inventory.

580

The simplified expressions for carbon-cycle feedback parameters [in equations \(6\) and \(7\)](#) based on the air-sea flux changes to the ocean may then be approximated by the global ocean carbon inventory changes, which may be expressed in terms of these different global ocean carbon pools [\(Williams et al., 2019\)](#):

$$\beta_O \approx \frac{\Delta C_O^*}{C'} = \frac{\Delta C_{preformed}^*}{C'} + \frac{\Delta C_{regenerated}^*}{C'} \quad (13)$$

$$= \frac{\Delta C_{sat}^*}{C'} + \frac{\Delta C_{disequilib}^*}{C'} + \frac{\Delta C_{regenerated}^*}{C'}$$

$$\gamma_O \approx \frac{\Delta C_O' - \Delta C_O^*}{T'} = \frac{\Delta C_{preformed}' - \Delta C_{preformed}^*}{T'} + \frac{\Delta C_{regenerated}' - \Delta C_{regenerated}^*}{T'}$$

$$= \frac{\Delta C_{sat}' - \Delta C_{sat}^*}{T'} + \frac{\Delta C_{disequilib}' - \Delta C_{disequilib}^*}{T'} + \frac{\Delta C_{regenerated}' - \Delta C_{regenerated}^*}{T'} \quad (14)$$

The anomalies for each of these carbon pools are calculated as

$$\Delta DIC_{regenerated} = -R_{CO} \Delta AOU + \frac{1}{2} (\Delta Alk - \Delta Alk_{pre} - R_{NO} \Delta AOU) \quad (15)$$

$$\Delta DIC_{sat} = f(pCO_2^{atm}, T_o, S_o, P, Si, Alk_{pre})_t - f((pCO_2^{atm}, T_o, S_o, P, Si, Alk_{pre})_{t=0}) \quad (16)$$

$$\Delta DIC_{disequilib} = \Delta DIC - \Delta DIC_{regenerated} - \Delta DIC_{sat} \quad (17)$$

where  $R_{CO}$  and  $R_{NO}$  are constant stoichiometric ratios,  $\Delta AOU$  is the change in apparent oxygen utilization from its pre-industrial value (where preformed oxygen is assumed to be approximately saturated with respect to atmospheric oxygen),  $\Delta Alk$  is the change in alkalinity,  $T_o$  and  $S_o$  are the ocean temperature and salinity, respectively,  $P$  and  $Si$  are the phosphate and silicate concentrations, and  $\Delta Alk_{pre}$  is the change in preformed alkalinity (Ito and Follows, 2005; Williams and Follows, 2011; [Appendix of](#) Lauderdale et al., 2013). [In equation \(16\),  \$\Delta DIC\_{sat}\$  is](#)

**Field Code Changed**

**Formatted:** Font: (Default) Calibri, 12 pt

**Deleted:** (Williams et al., 2019)

**Formatted:** Font: (Default) +Body (Calibri), 11 pt, Check spelling and grammar



600 calculated using the partial pressure of  $\text{CO}_2$  in the atmosphere ( $p\text{CO}_2^{\text{atm}}$ ) and preformed alkalinity  
 601 as represented by the function  $f$  following the iterative solution for the ocean carbon system of  
 602 Follows et al. (2006) and by considering the small contribution of minor species (borate,  
 603 phosphate, silicate) to the preformed alkalinity, at time  $t$  and the pre-industrial values at time  
 604  $t=0$ . In equation (16), the calculation uses the preformed alkalinity, the alkalinity at the time of  
 605 water subduction, instead of the total instantaneous alkalinity to remove the effect of  $\text{CaCO}_3$   
 606 dissolution from the time the water parcel lost contact with the atmosphere. The preformed  
 607 alkalinity is estimated from a multiple linear regression using salinity and the conservative tracer  
 608 PO ( $\text{PO}=\text{O}_2-\text{R}_{\text{O}_2:\text{P}}$ ) (Gruber et al., 1996), with the coefficients of this regression estimated based  
 609 on the upper ocean (first 10 meters) alkalinity, salinity, oxygen and phosphate in each model. Our  
 610 diagnostics of the ocean feedbacks and carbon pools depend primarily upon changes in DIC, the  
 611 preformed and regenerated pools, relative to the pre-industrial; although differences in the pre-  
 612 industrial ocean in our suite of models do affect the saturated DIC changes relative to the pre-  
 613 industrial by ~5% or less due to the non-linearity of the carbonate chemistry.

Formatted: Subscript

Formatted: Font: (Default) Calibri, 12 pt

Formatted: Font: (Default) Calibri, 12 pt

Deleted: In equation (16),  $\Delta\text{DIC}_{\text{sat}}$  is calculated using values of  $p\text{CO}_2^{\text{atm}}$ ,  $T_o$ ,  $S_o$ ,  $P$ ,  $\text{Si}$ , and  $\text{Alk}_{\text{pre}}$  at time  $t$  and the pre-industrial values at time  $t=0$ .

Deleted: The small contribution from minor species (borate, silicate, phosphate) to the alkalinity is removed from the total alkalinity before using it for estimates of the carbon system following the algorithm of (Follows et al., 2006).

Deleted: pre

Deleted: ,

Formatted: Font: (Default) +Body (Calibri), 12 pt

Deleted: although differences in the pre-industrial ocean do slightly affect the saturated DIC due to the non-linearity of the carbonate chemistry

### 615 3. Model descriptions

616

617 Table 2 summarizes the primary features of the eleven comprehensive ESMs that contributed  
 618 results to this study. Brief descriptions of land and ocean carbon cycle components of these ESMs  
 619 are provided in the Appendix. The eleven ESMs, in alphabetical order, are the 1) Commonwealth  
 620 Scientific and Industrial Research Organisation (CSIRO) ACCESS-ESM1.5, 2) Beijing Climate Centre

633 (BCC) BCC-CSM2-MR, 3) Canadian Centre for Climate Modelling and Analysis (CCCma) CanESM5,  
634 4) Community Earth System Model, version 2 (CESM2), 5) Centre National de Recherches  
635 Météorologiques (CNRM) CNRM-ESM2-1, 6) Institut Pierre-Simon Laplace (IPSL) IPSL-CM6A-LR,  
636 7) Japan Agency for Marine-Earth Science and Technology (JAMSTEC) in collaboration with the  
637 University of Tokyo and the National Institute for Environmental Studies (Team MIROC) MIROC-  
638 ES2L, 8) Max Planck Institute for Meteorology (MPI) MPI-ESM1.2-LR, 9) Geophysical Fluid  
639 Dynamics Laboratory (GFDL) NOAA-GFDL-ESM4, 10) Norwegian Climate Centre (NCC) NorESM2-  
640 LM, and 11) United Kingdom (UK) UKESM1-0-LL.

641

642 In contrast to the A13 study where only two of the eight participating comprehensive ESMs had  
643 terrestrial N cycle implemented and coupled to their C cycle, in this study six of the eleven  
644 participating ESMs represent coupling of terrestrial C and N cycles. These six models are the  
645 ACCESS-ESM1.5, CESM2, MIROC-ES2L, MPI-ESM1.2-LR, NorESM2-LM, and UKESM1-0-LL. Note  
646 that CESM2 and NorESM2-LM employ the same land surface component – the version 5 of the  
647 Community Land Model (CLM5) so we expect the land carbon cycle to respond very similarly in  
648 the two models. Three of the ESMs have land components that dynamically simulate vegetation  
649 cover and competition between their PFTs - NOAA-GFDL-ESM4, MPI-ESM1.2-LR, and UKESM1-0-  
650 LL.

651

## 652 4. Results

653

Deleted: which

Deleted: d

#### 656 4.1. Global surface CO<sub>2</sub> fluxes and temperature change

657

658 Figure 1 shows the simulated changes in temperature in the three model configurations (COU,  
659 BGC, and RAD) of the 1pctCO<sub>2</sub> experiment. Here and in subsequent figures, results are also  
660 shown for the eight comprehensive ESMs that participated in the A13 study. The eight models in  
661 the A13 study are a subset of eleven models considered in this study although they have been  
662 updated since CMIP5.

663

664 As expected, temperature change is higher in the COU and RAD simulations, than in the BGC  
665 simulation, since the radiative forcing responds to increasing [CO<sub>2</sub>] in these simulations. The small  
666 temperature change in the BGC simulation is due to a number of contributing but also  
667 compensating factors: 1) reduction in transpiration, and hence latent heat flux, due to stomatal  
668 closure in response to increasing [CO<sub>2</sub>] (Cao et al., 2010), 2) increase in vegetation leaf area index  
669 (LAI), which decreases land surface albedo and hence increases absorbed solar radiation, 3)  
670 increase in vegetation fraction in models that explicitly simulate competition between their plant  
671 functional types (PFTs) over land (NOAA-GFDL-ESM4, MPI-ESM1.2-LR, and UKESM1-0-LL) which  
672 also leads to reduced land surface albedo. As a result, temperature change in the COU simulation  
673 is higher than in the RAD simulation since these biogeochemical processes are active and  
674 contribute to a small additional warming. This is seen in panel (a) for CMIP6 models and panel  
675 (b) for CMIP5 models.

676

**Deleted:** The values show the model mean and the range across the ten participating models, since results from the RAD configuration of the NorESM2-LM model were not available at the time of writing of this manuscript.

**Deleted:** model mean

**Deleted:** to allow a direct comparison between CMIP5 and CMIP6 models.

684 When comparing CMIP5 and CMIP6 models, the CMIP6 models are on average slightly warmer  
 685 than CMIP5 models in the COU and RAD simulations. In Figure 1a, the globally-averaged near  
 686 surface temperature change at CO<sub>2</sub> quadrupling in the COU simulation is 4.87 °C in CMIP6  
 687 models, compared to 4.74 °C in CMIP5 models. The CMIP6 ensemble considered here includes  
 688 some high climate sensitivity models including CanESM5, CESM2, CNRM-ESM2-1, IPSL-CM6A-LR,  
 689 and UKESM1-0-LL. The globally-averaged temperature change at CO<sub>2</sub> quadrupling in the COU  
 690 simulation for the eight models that are common to this (CMIP6) and the A13 (CMIP5) studies,  
 691 are 4.97 and 4.74 °C, respectively. The temperature change in the BGC simulation in CMIP6  
 692 models (0.2<sup>1</sup> °C) is, however, slightly lower than in the CMIP5 models (0.26 °C). The values in  
 693 Figure 1 for participating CMIP5 models are slightly different than those reported in A13 study  
 694 because those numbers also included the UVic Earth System Climate Model (an intermediate  
 695 complexity model) which we have omitted here to keep the comparison consistent between  
 696 comprehensive ESMs. In addition, in contrast to A13, the temperature at the end of the  
 697 simulations in this study is calculated after fitting a 4<sup>th</sup> order polynomial in R to the model mean  
 698 values rather than using the actual model mean value at the end of the simulation which can be  
 699 higher or lower than that calculated using the polynomial fit due to inter-annual variability. A 4<sup>th</sup>  
 700 order polynomial fit has been shown to yield a good estimate of the forced response of global  
 701 mean temperature response and to minimize the potential influence of internal variability  
 702 (Hawkins and Sutton, 2009).

Deleted: fully-coupled

Deleted: 5.00 °C (

Deleted: when NorESM2-LM is included)

Deleted: fully-coupled

Deleted: 4

Deleted: smaller

Deleted: a

Formatted: Superscript

Formatted: Font: 12 pt

Formatted: Font: 12 pt, Superscript

Formatted: Font: 12 pt

Formatted: Font: 12 pt

Formatted: Font: 12 pt

Formatted: Font: 12 pt

Field Code Changed

704 Figure 2 and 3 show simulated model mean values and the range across models for annual  
 705 simulated atmosphere-land and atmosphere-ocean CO<sub>2</sub> fluxes and their cumulative values for

713 participating CMIP6 and CMIP5 models from the COU, BGC, and RAD configurations of the  
714 1pctCO<sub>2</sub> experiment. The general results from CMIP6 models are broadly similar in nature to  
715 those from CMIP5 models, as would be expected, with higher annual and cumulative values of  
716 atmosphere-land and atmosphere-ocean CO<sub>2</sub> fluxes in the BGC simulation compared to the COU  
717 simulation in which the radiative warming caused by increasing CO<sub>2</sub> weakens the land and ocean  
718 sinks. In the RAD simulation, where land and ocean carbon cycle components do not respond to  
719 increasing [CO<sub>2</sub>], both components lose carbon, for reasons discussed below.

**Deleted:** fully-, biogeochemically- and radiatively-coupled

**Deleted:** Here, in contrast to Figure 1, results from all eleven models are included since model mean cumulative atmosphere-land and atmosphere-ocean CO<sub>2</sub> fluxes are not particularly sensitive to inclusion/exclusion of the NorESM2-LM models for which results from the RAD simulation were not available.

720  
721 Over land, the model mean rate of increase of atmosphere-land CO<sub>2</sub> flux declines and even  
722 becomes negative in the COU and BGC simulations as the terrestrial CO<sub>2</sub> fertilization effect  
723 saturates and the carbon pools build up, which increases the respiratory losses. The biggest  
724 difference between the CMIP5 and CMIP6 models is that the cumulative land carbon uptake in  
725 the COU simulation is about 25 % higher in CMIP6 ( $635 \pm 258$  PgC, mean  $\pm$  standard deviation)  
726 models than in CMIP5 ( $505 \pm 297$  PgC) models, although this increase is not statistically significant  
727 across the model ensemble (Mann-Whitney test). Here and hereafter, we use sample (not

728 population) standard deviation. The cumulative value of carbon loss in the RAD simulation is  
729 similar in both CMIP6 and CMIP5 models,  $239 \pm 120$  vs.  $252 \pm 158$  PgC, respectively. This carbon

**Deleted:** 50

**Deleted:** 1

730 loss occurs due both to increased heterotrophic respiration per unit carbon mass and reduced  
731 GPP (and consequently NPP) in the RAD simulation (not shown). While NPP declines globally in  
732 response to increase in temperature, mid- to high-latitude net primary production increases  
733 (Qian et al., 2010) so the reduction in global NPP comes largely from the reduction in the tropics.

734 The large spread across CMIP6 land carbon cycle models, seen also in earlier F06 and A13 studies,

**Deleted:** range

744 has not changed significantly compared to CMIP5 models, and its implications will be discussed in  
 745 more detail in Section 5. As discussed later in Section 4.3, the standard deviation of land carbon-  
 746 climate feedback increases from CMIP5 to CMIP6 models, while it decreases somewhat for the  
 747 land carbon-concentration feedback.

**Deleted:** meaningfully declined for CMIP6 models participating in this study

**Deleted:** This is also seen later

**Deleted:** in Figure 6 which compares the absolute magnitude and the standard deviation of the strength of the feedback parameters from CMIP5 and CMIP6 models

**Deleted:** .

748  
 749 Over the ocean, the response to increasing [CO<sub>2</sub>] and changing climate remains fairly similar  
 750 across CMIP5 and CMIP6 models. The cumulative ocean carbon uptake in the COU simulation is  
 751 593 ± 54 and 611 ± 50 PgC in CMIP6 and CMIP5 models, respectively. Unlike the land uptake,  
 752 however, the ocean carbon uptake does not saturate over the length of the simulation in the BGC  
 753 simulation (Figure 3, panels a and b); it keeps on increasing albeit at a declining rate. The  
 754 cumulative ocean carbon loss in the RAD simulation is 23 ± 19 and 37 ± 17 PgC in CMIP6 and  
 755 CMIP5 models, respectively, and is primarily associated with warmer temperatures which reduce  
 756 CO<sub>2</sub> solubility (Goodwin and Lenton, 2009; Schwinger et al., 2014).

**Commented [A[3]:** Ric/Anna is it okay to say “primarily” since changes in ocean circulation do not contribute to loss of C from ocean in the RAD simulation. This is in response to Kirsten’s question.

**Deleted:** (Goodwin and Lenton, 2009)

**Field Code Changed**

**Formatted:** Font: (Default) Calibri, 12 pt

**Formatted:** Font: 11 pt, Check spelling and grammar

**Deleted:** Figure 4 shows results from individual CMIP6 models for which model means and ranges were shown in Figures 1, 2, and 3. Figure 4 allows identification of models which behave differently compared to the majority of models. In Figure 4, panels a and c, CanESM5 shows the largest temperature increase, and NorESM2-LM and MIROC-ES2L the smallest, in response to increase in [CO<sub>2</sub>] for the COU and RAD simulations, respectively. For cumulative atmosphere-land CO<sub>2</sub> flux in the COU simulation (panel d), CanESM5 simulates the largest land carbon uptake and ACCESS-ESM1.5 the smallest. This is not the case for the BGC simulation (panel e) where land carbon uptake from the BCC-CSM2-MR and CNRM-ESM2.1 are the largest among all models, while land carbon uptake from the ACCESS-ESM1.5 is the lowest. Finally, in the RAD simulation (panel f) the loss of carbon from land in response to increasing temperatures is lowest in the MPI-ESM1.2-LR and largest in the BCC-CSM2-MR. Over the ocean, while most models behave very similarly, the carbon uptake in the BCC-CSM2-MR, ACCESS-ESM1.5, and NOAA-GFDL-ESM4 are larger than most models in the COU and BGC simulations. In the RAD simulation, almost all models simulate a loss of carbon from the ocean, but the CNRM-ESM2.1 shows a small uptake. Reasons for divergent response of some models are presented later. ¶

757  
 758 As in F06 and A13, the range in cumulative atmosphere-land CO<sub>2</sub> fluxes among models at the end  
 759 of the COU simulation, in response to changes in atmospheric CO<sub>2</sub> concentration and surface  
 760 temperature, is three to four times larger than for the atmosphere-ocean CO<sub>2</sub> fluxes. Figure A1  
 761 shows results from individual CMIP6 models for which model means and ranges were shown in  
 762 Figures 1, 2, and 3 and allows identification of models which behave differently compared to the  
 763 majority of models.

**Deleted:** ¶

## 797 4.2. Carbon budget terms

798

799 Figure 4a shows the carbon budget components of the diagnosed cumulative fossil fuel emissions  
800 at the end of the 140-year period of the 1pctCO<sub>2</sub> COU experiment when CO<sub>2</sub> concentration  
801 quadruples ( $\tilde{E}_{4\times\text{CO}_2}$  or simply  $\tilde{E}$ ), from CMIP6 models. Cumulative emissions can similarly also  
802 be calculated at 2×CO<sub>2</sub> ( $\tilde{E}_{2\times\text{CO}_2}$ ). The term “carbon budget” in this context refers to the  
803 accounting of carbon internal to individual ESMs. The sum of ocean ( $\Delta C'_O$ ) and land ( $\Delta C'_L$ ) sinks  
804 and the resulting change in atmospheric carbon burden ( $\Delta C'_A$ ) yields cumulative fossil fuel  
805 emissions which are consistent with the specified CO<sub>2</sub> pathway (the 1pctCO<sub>2</sub> scenario in this  
806 case) as indicated in the appendix [\(Equation A6\)](#). The corollary to this is that, in a specified  
807 emissions simulation, if the respective fossil fuel emissions were to be used in their models, each  
808 model will yield CO<sub>2</sub> concentrations that rise at a rate of 1% per year. The term “diagnosed”  
809 implies that the cumulative fossil fuel emissions are calculated from changes in atmosphere, land  
810 and ocean carbon pools in the specified-concentration 1pctCO<sub>2</sub> experiment. Figure 4b shows the  
811 terms of the budgets as fractional components for atmosphere (A), land (L) and ocean (O) based  
812 on equation (A7), where  $f_A$  is the airborne fraction of emissions and  $f_L$  and  $f_O$  are the fractions  
813 of emissions take up by land and ocean, respectively. More details are provided in [Section A1 of](#)  
814 the Appendix.

Deleted: 5

Deleted: atmospheric CO<sub>2</sub> growth rate

Deleted: after the fact

Deleted: In Figure 5a, the results are arranged in an ascending order according to models' diagnosed cumulative fossil fuel emissions.

Deleted: 5

$$815 \quad \Delta C'_A + \Delta C'_L + \Delta C'_O = \int_0^t E \, dt = \tilde{E} \quad (18)$$

$$816 \quad f_A + f_L + f_O = 1 \quad (19)$$

824 All panels in Figure 4 identify models whose land component includes a representation of the N  
825 cycle – the cumulative land carbon uptake (panels a and c) and fractional emissions taken up by  
826 land (panels b and d) for these models are shown in red.

Deleted: 5

827  
828 Consistent with Figures 2 and 3, and CMIP5 results reported in the A13 study, the differences  
829 among models are primarily due to the diverse response of the land carbon cycle components.

Deleted: Finally, model mean values are also shown for all models and for models whose land components include and do not include a representation of the land N cycle. For comparison, panels c and d in Figure 5 show the same results but for CMIP5 models reported in A13.¶

830 While the model mean cumulative carbon uptake by the ocean is fairly similar between  
831 participating CMIP5 ( $611 \pm 50$  PgC) and CMIP6 ( $593 \pm 54$  PgC) models, the land uptake is higher  
832 in CMIP6 ( $635 \pm 258$  PgC) compared to CMIP5 ( $505 \pm 297$  PgC) models, as mentioned earlier. This

Deleted: 4,

833 is the case even when the CanESM5, the model with the largest land carbon uptake, is omitted  
834 from CMIP6 models (model mean land carbon uptake for the remaining ten models is  $578 \pm 185$   
835 PgC). As a result, model mean cumulative diagnosed emissions from CMIP6 models ( $3031 \pm 242$   
836 PgC) are about 4% higher than for CMIP5 models ( $2927 \pm 294$  PgC). In Figure 5a, the land carbon  
837 uptake in CESM2 (656 PgC) and NorESM2-LM (652 PgC) model are very similar; as noted above

838 these models employ the same land component. Model mean estimates that are reported  
839 separately for models whose land component do and do not include a representation of N cycle,

Deleted: ¶  
¶

840 for both CMIP5 and CMIP6 models, show that model-mean land carbon uptake is lower for  
841 models that explicitly represent the N cycle. As a consequence, the airborne fraction of emissions  
842 is also higher for models that represent land N cycle and their diagnosed cumulative fossil fuel  
843 emissions are lower (Figure 4). Six of the eleven CMIP6 ESMs considered in this study represent

Deleted: 5

844 N cycle over land compared to only two of the eight considered in the A13 study based on CMIP5  
845 models. Yet, the model-mean land carbon uptake over land is higher in this study than in the A13



857 study. This is partly because of the three models with the largest land carbon uptake (CNRM-  
 858 ESM2-1, BCC-CSM2-MR, and CanESM5) which do not include land N cycle (Figure 4a). In addition,  
 859 inclusion of N cycle does not universally imply lower land C uptake. In Figure 4a, IPSL-CM6A-LR  
 860 and NOAA-GFDL-ESM4, both of which do not include land N cycle, yield lower land carbon uptake  
 861 than four of the models that do include land N cycle.

862  
 863 Figure 4a and 4c allow direct comparison of models from the same modelling group. CanESM2,  
 864 from the CCCma, which had below average land carbon uptake among CMIP5 models, has  
 865 evolved to CanESM5, a model with the largest land carbon uptake among CMIP6 models. The  
 866 reason for this is an increase in the strength of its CO<sub>2</sub> fertilization effect following the retuning  
 867 of its photosynthesis downregulation parameters, using carbon budget constraints over the  
 868 historical period, as explained in (Arora and Scinocca, 2016). CESM1, which had one of the lowest  
 869 land carbon uptake among CMIP5 models, because of its apparently excessive nitrogen limitation  
 870 effect in CLM4, has evolved to CESM2 (with CLM5 land component) with near average land  
 871 carbon uptake among CMIP6 models. The transition of CLM from CLM4 to CLM5, and the  
 872 reduction in its nutrient constraints on photosynthesis and the parametric controls on  
 873 fertilization responses are discussed in Wieder et al. (2019) and Fisher et al. (2019), respectively.  
 874 The land carbon uptake in MIROC-ESM increased from the lowest among CMIP5 models to near  
 875 average for MIROC-ES2L, among CMIP6 models, due to a new terrestrial biogeochemical  
 876 component (Ito and Inatomi, 2012). Although the CO<sub>2</sub> fertilization effect in this new land model  
 877 is weaker likely due to the incorporation of the nitrogen cycle, the model yields relatively higher  
 878 NPP (Hajima et al., 2020), due to a higher CUE<sub>Δ</sub> (as confirmed later in section 4.4.1). The land

Deleted: ¶

Deleted: 5

Deleted: 5

Deleted: Canadian Centre for Climate Modelling and Analysis

Deleted: (Wieder et al., 2019)

Formatted: Font: (Default) +Body (Calibri), 11 pt, Check spelling and grammar

Deleted: (

Field Code Changed

Deleted: ,

Formatted: Font: (Default) Calibri, 12 pt

Formatted: Font: (Default) Calibri, 12 pt

Deleted: (149 PgC)

Deleted: 701 PgC

Field Code Changed

Formatted: Font: 12 pt

Deleted: (Hajima et al., 2019b)

Formatted: Font: (Default) +Body (Calibri), Check spelling and grammar

Field Code Changed

889 carbon uptake in the IPSL-CM5A-LR model decreased from being the second largest in CMIP5  
890 models to below average for the IPSL-CM6A-LR model due to implementation of terrestrial  
891 photosynthesis downregulation, as a function of CO<sub>2</sub> concentration, which leads to a decrease in  
892 GPP across all latitudes, with the largest decrease in the tropics. For the MPI ESM, the decrease  
893 in land carbon uptake in MPI-ESM-LR for CMIP5 to MPI-ESM1.2-LR for CMIP6 is associated with  
894 implementation of nitrogen cycle model (Goll et al., 2017) and a new soil carbon model YASSO  
895 (Goll et al., 2015). Compared to its predecessor HadGEM2-ES, UKESM1-0-LL represents a  
896 prognostic treatment of terrestrial nitrogen including its impact on carbon storage in vegetation  
897 biomass and soil organic matter. Limitation on terrestrial productivity from available nitrogen is  
898 likely also the main reason for reduced land carbon storage in UKESM1-0-LL compared to  
899 HadGEM2-ES.

Deleted: (741 PgC)

Deleted: (477 PgC)

901 The ocean carbon uptake in the IPSL model decreased from being the largest among CMIP5  
902 models in IPSL-CM5A-LR to being lower than average for IPSL-CM6A-LR, and this change is  
903 attributed to a greater ocean stratification in the IPSL-CM6A-LR. The annual mean mixed layer  
904 depth is 46.7 m and 40.2 m in IPSL-CM5A-LR and IPSL-CM6A-LR, respectively. While NorESM1-  
905 ME was one of the CMIP5 models with the largest ocean carbon uptake, NorESM2-LM has an  
906 ocean carbon uptake close to the CMIP6 model mean. This change is a consequence of changes  
907 in the simulated (shallower depth and weaker strength) Atlantic meridional overturning  
908 circulation and reduced mixed layer biases particularly at high latitudes (less deep winter mixing).  
909 Due to these modifications, the efficiency of carbon export below the mixed layer in NorESM2-  
910 LM is considerably reduced compared to the NorESM1-ME. This, in turn, leads to less excess

Deleted: at 670 PgC

Deleted: 579 PgC

Deleted: (667 PgC)

Deleted: (599 PgC)

917 carbon stored in the North Atlantic Deep Water (below 2000 m) as well as in the Antarctic  
918 Intermediate Water.

919  
920 Figure A2 in the appendix shows a version of Figure 4 but at the time of CO<sub>2</sub> doubling (at year  
921 70). Interestingly, the ordering of the models according to their diagnosed cumulative emissions  
922 at 2×CO<sub>2</sub> is different from that at 4×CO<sub>2</sub>. As expected, however, the model mean fractional  
923 emissions taken up by land and ocean at 2×CO<sub>2</sub> are higher than at 4×CO<sub>2</sub>, because both land and  
924 ocean carbon sinks relatively weaken as CO<sub>2</sub> continues to increase.

925

#### 926 4.3. Feedback parameters

927 Figure 5, panels a and b, compares the carbon-concentration ( $\beta_L$ ) and carbon-climate feedback  
928 ( $\gamma_L$ ) parameters over land from participating CMIP6 models calculated using results at the end of  
929 the BGC, RAD, and COU simulations. The plots show feedback parameters from different models  
930 as coloured dots but also their mean  $\pm 1$  standard deviation as a box. Three primary observations  
931 can be made from Figure 5. First and foremost, the spread in the magnitude of carbon-  
932 concentration and carbon-climate feedback over land in CMIP6 models is of similar magnitude  
933 to that of CMIP5 models (panels c and d). Second, the carbon-climate feedback ( $\gamma_L$ ) is more  
934 sensitive to the approach used (and hence the type of simulations used) to derive its value than  
935 the carbon-concentration feedback ( $\beta_L$ ). The absolute value of  $\beta_L$  varies by around 7%, while  $\gamma_L$   
936 varies by up to 26%, depending on the approach used. Third, in the model mean sense, the  
937 absolute strength of the feedback parameters is weaker for models that include a representation

**Deleted:** For the MPI ESM, the decrease in land carbon uptake from 825 PgC in MPI-ESM-LR for CMIP5 to 586 PgC in MPI-ESM1.2-LR for CMIP6 is associated with implementation of nitrogen cycle model (Goll et al., 2017) and a new soil carbon model YASSO (Goll et al., 2015). Compared to its predecessor HadGEM2-ES, UKESM1 represents a prognostic treatment of terrestrial nitrogen including its impact on carbon storage in vegetation biomass and soil organic matter. Limitation on terrestrial productivity from available nitrogen is the main reason for reduced land carbon storage in UKESM1-0-LL (408 PgC) compared to HadGEM2-ES (768 PgC).

**Deleted:** ¶

**Deleted:** 1

**Deleted:** the

**Deleted:** 5

**Deleted:** 6

**Deleted:** . The feedback parameters are calculated using all of the four approaches that are summarized in Table 1 to illustrate their sensitivity to the approach used. In addition, models whose land component includes a representation of the N cycle are identified by an additional circle around their coloured dots. Figure 6 also shows the mean  $\pm 1$  standard deviation values separately for models that do and do not include a representation of the land N cycle using the BGC-COU approach, in an attempt to understand the reason for the diverse responses of the land models. Results from CMIP5 models in the A13 study are shown in a similar format for comparison in panels c and d

**Deleted:** ¶

¶

**Deleted:** 6

968 of the N cycle, for both CMIP5 and CMIP6 models. Both the carbon gain due to increase in  
969 atmospheric CO<sub>2</sub> concentration and the carbon loss due to increase in globally average  
970 temperature in models with representation of land N cycle is much lower than in models that do  
971 not include the N cycle. This response is most likely explained by the N limitation of  
972 photosynthesis as CO<sub>2</sub> increases and additional release of N from dead organic matter as  
973 warming increases which boosts productivity thereby compensating for carbon lost due to  
974 increased respiratory losses, as also discussed in A13. The values of the feedback parameters,  
975 however, overlap between models that do and do not include a representation of the N cycle,  
976 given the wider spread in the feedback parameter values among models that do not include a  
977 representation of land N cycle, compared to models that do.

978

979 Figure 6, panels a and b, compare the carbon-concentration ( $\beta_o$ ) and carbon-climate feedback  
980 ( $\gamma_o$ ) parameters over the ocean from participating CMIP6 models. For both CMIP5 and CMIP6  
981 models, the absolute spread in the magnitude of the feedback parameters across the  
982 participating models is an order of magnitude smaller for the ocean C cycle component compared  
983 to the land C cycle component, as was also seen in F06 and A13. Similar to the land, the calculated  
984 values of the ocean carbon-climate feedback ( $\gamma_o$ ) are more sensitive to the approach used (and  
985 hence the type of simulations used) than the ocean carbon-concentration feedback ( $\beta_o$ ). In  
986 agreement with (Schwinger et al., 2014), the absolute values of  $\gamma_o$  are 2-3 times larger when  
987 calculated using the COU and BGC simulations, compared to cases when RAD simulation is used,  
988 for reasons mentioned earlier. Figures 5 and 6 show also that while the strength of the carbon-

Deleted: 7

Deleted: As in Figure 6, the feedback parameters are calculated using all of the four approaches that are summarized in Table 1 and results from CMIP5 models are shown for comparison in panels c and d.

Field Code Changed

Deleted: 6

Deleted: 7

996 concentration feedback is similar over land and ocean, the strength of the carbon-climate  
997 feedback parameter over ocean is much weaker than over land.

998  
999 Figures 5 and 6 provide justification for using the BGC-COU approach, over the RAD-BGC and  
1000 RAD-COU approaches, in calculating the feedback parameters as discussed below. In Figure 6,  
1001 the absolute magnitude of  $\gamma_o$  when using the BGC-COU approach is about twice in CMIP5 models,  
1002 and more than three times in CMIP6 models, compared to its model-mean value calculated using  
1003 the RAD-BGC and RAD-COU approaches. The reason for this is that the RAD simulation misses the  
1004 suppression (due to weakening of the ocean circulation) of carbon drawdown to the deep ocean  
1005 due to lack of buildup of a strong carbon gradient from the atmosphere to the deep ocean, as  
1006 mentioned earlier. This process is important when climate change is forced by increasing  
1007 atmospheric CO<sub>2</sub>, and therefore feedback parameters calculated using the BGC-COU approach  
1008 are more likely to include all processes relevant to application for realistic scenarios. In Figure 6  
1009 value of  $\gamma_o$  changes sign for the CNRM-ESM2-1 model from positive when calculated using the  
1010 RAD-BGC or RAD-COU approaches to negative when calculated using the BGC-COU approach and  
1011 this further illustrates the sensitivity of feedback parameters to the approach used to calculate  
1012 them. Section A2 discusses the reasons for this sensitivity in the CNRM-ESM2-1 model.

1013  
1014 In Figure 5, although the carbon-climate feedback parameter over land ( $\gamma_l$ ) is larger in absolute  
1015 amount, it is comparatively less sensitive to the approach used, than over ocean, because over  
1016 land an increase in temperature not only increases the respiratory losses but also affects

1017 photosynthetic processes especially in conjunction with increasing CO<sub>2</sub>. Warmer temperatures  
 1018 increase photosynthesis over mid to high latitude regions where photosynthesis is currently  
 1019 limited by temperature and more so with increasing CO<sub>2</sub>, but decrease photosynthesis over  
 1020 tropical regions where the temperatures are already too warm for optimal photosynthesis. The  
 1021 net result of these compensating processes plays out very differently in different models and in  
 1022 the model-mean sense this results in less sensitivity of the calculated value of carbon climate  
 1023 feedback parameter over land ( $\gamma_L$ ) to the different approaches than over ocean. This is seen in  
 1024 both CMIP5 and CMIP6 models. Over land, photosynthesis is also affected by temperature (with  
 1025 widely varying responses between models) in addition to respiration and the  $\gamma_L$  values vary  
 1026 widely between models between the RAD-BGC/RAD-COU approach and the BGC-COU approach.  
 1027 This is seen, for example, for ACCESS-ESM1.5, IPSL-CM6A-LR, and CanESM5 models in Figure 5b.

1029 Figures 5 and 6 also show that the effect of assuming  $T^*$  (the temperature change in the BGC  
 1030 simulation) zero is around 1% for the calculated value of the carbon-concentration feedback  
 1031 parameter ( $\beta_X, X = L, O$ ) and around 5% for the carbon-climate feedback parameter ( $\gamma_X, X =$   
 1032  $L, O$ ). This small effect of  $T^*$  on the calculated global values of the feedback parameter allows  
 1033 investigation of the reasons for differences among model by using simplified forms of  $\beta_X$  and  $\gamma_X$   
 1034 as presented in equations (6) and (7).

1036 For completeness, Table A1 in the appendix summarizes the values of feedback parameters for  
 1037 both land and ocean from CMIP6 and CMIP5 models (corresponding to Figures 5 and 6) at 4×CO<sub>2</sub>

**Deleted:** Section A2 in the appendix discusses how Figures 6 and 7 and corroborate existing studies for the preferred use of the BGC and COU simulations for finding the feedback parameters.

**Deleted:** 6

**Deleted:** 7

**Formatted:** Font: Italic

**Formatted:** Font: Italic

**Deleted:** 6

**Deleted:** 7

1045 but also at 2×CO<sub>2</sub>. Table A1 also shows the value of parameter α, the linear transient climate  
1046 sensitivity to CO<sub>2</sub>, following F06 (their equation 6) which is calculated using values at the end of  
1047 COU simulation as

1048 
$$T' = \alpha c' \quad (20)$$

1049 **4.4. Reasons for differences among models**

1050 **4.4.1 Land**

1051 Equations (8) and (9) in Section 2.1.1 are used to gain insight into reasons for differing responses  
1052 of land models. In the BGC-COU approach and assuming T\*=0 (equation 8), the carbon uptake in  
1053 the BGC simulation is used to calculate the carbon-concentration feedback parameter ( $\beta_L$ ).  
1054 Figure 7 shows how this carbon uptake over land is separated into vegetation and soil+litter  
1055 components both in absolute (panel a) and fractional terms (panel b). Figure 7b shows that  
1056 models vary widely in terms of how the carbon uptake over land is split into vegetation and  
1057 soil+litter components. The model mean values indicate that slightly more of the carbon  
1058 sequestered is allocated to vegetation (55%) than to the soil+litter pools (45%).

1059  
1060 Figure 8 shows the individual components of equation (8) which contribute to terms  
1061 corresponding to changes in vegetation ( $\Delta C_V$ ) and soil+litter ( $\Delta C_S$ ) carbon pools. Panel (a) of  
1062 Figure 7 is repeated in Figure 8 for easy correspondence of individual components of equation  
1063 (8) with their models. The model mean values of individual terms do not take into account the  
1064 results from the BCC-CSM2-MR model as explained in the figure caption. In essence, the terms in

Deleted:

Deleted: at 4 xCO<sub>2</sub>.¶

Deleted: 8

Deleted: The models are arranged from lowest to highest in terms of their land carbon uptake in the BGC simulation. The partitioning into vegetation and soil+litter components is not shown for the BCC-CSM2-MR model because total land carbon uptake in this model exceeded the sum of changes in the vegetation and soil+litter carbon pools by more than 10% likely because of incomplete accounting of pool sizes.

Deleted: 8

Deleted: 9

Deleted: 8

Deleted: 9

Deleted: terms

Figure 8 are emergent properties of the land models of the individual ESMs and result from their multiple interacting processes. The comparison of the individual terms of equation (8) provides additional insight into the reasons for differences in land models. For example, the CNRM-ESM2-1 model has the highest land carbon uptake among all models in the BGC simulation. However, this is not caused by a strong CO<sub>2</sub> fertilization effect (the  $\frac{\Delta GPP}{c'}$  term), but rather by the relatively high  $\tau_{veg\Delta}$  and  $\tau_{soil\Delta}$  values. The CO<sub>2</sub> fertilization effect is strongest for the three models that simulate vegetation cover dynamically (NOAA-GFDL-ESM4, MPI-ESM1.2-LR, and UKESM1-0-LL) since the  $\frac{\Delta GPP}{c'}$  term also implicitly includes the effect of increasing vegetation cover as CO<sub>2</sub> increases. The tree cover in the NOAA-GFDL-ESM4 model, for example, increases in the BGC simulation – particularly in dry, high-latitude regions above 50° N (not shown). However, these models do not simulate the largest land carbon uptake because of their lower than average  $\tau_{veg\Delta}$  and  $\tau_{soil\Delta}$  values. The  $\frac{\Delta GPP}{c'}$  term is unable to capture the CO<sub>2</sub> fertilization effect separately from increasing vegetation cover and this illustrates the challenge in comparing models that do and do not simulate vegetation cover dynamically. The CanESM5 model exhibits higher than average land carbon uptake despite its near average strength of the CO<sub>2</sub> fertilization effect, and  $\tau_{veg\Delta}$  and  $\tau_{soil\Delta}$  values. However, its  $CUE_{\Delta}$  is the highest and therefore a much larger fraction of GPP is converted to NPP. Although  $CUE_{\Delta}$  is not the same as  $CUE$ , we found that  $CUE_{\Delta}$  and  $CUE$  (calculated at the end of the 1pctCO<sub>2</sub> simulation at 4xCO<sub>2</sub>) are strongly correlated with a correlation of around 0.90 (not shown). Similarly,  $\tau_{veg\Delta}$  is strongly correlated, with a correlation of 0.96, to  $\tau_{veg} = C_V/NPP$  calculated at the end of the simulation. The ACCESS-ESM1.5 model exhibits the lowest land carbon uptake because of its weak CO<sub>2</sub> fertilization effect and the lowest  $CUE_{\Delta}$  of all models.

Deleted: 9

Deleted:  $\frac{\Delta GPP}{c'} = 0.141, 0.128, \text{ and } 0.117 \text{ PgC yr}^{-1} \text{ ppm}^{-1}$  for

Deleted: , respectively

Deleted:

Deleted: x



1107 Finally, the  $\frac{\Delta R_h}{\Delta LF}$  term shows the least variability across models, which is reflective of the fact that  
 1108 the magnitude of the heterotrophic respiration flux is dominated by NPP inputs into the dead  
 1109 carbon pools (Koven et al., 2015). Several of these individual terms are strongly correlated. The  
 1110  $\frac{\Delta GPP}{c'}$  and  $\frac{\Delta LF}{c'}$  terms have a correlation of 0.77, and  $CUE_{\Delta}$   $\frac{\Delta GPP}{c'}$  and  $\frac{\Delta LF}{c'}$  have a correlation of  
 1111 0.94, since a stronger CO<sub>2</sub> fertilization effect also implies a larger litter fall flux per unit CO<sub>2</sub>.  
 1112 Surprisingly,  $CUE_{\Delta}$  and  $\tau_{veg}$  are negatively correlated (correlation = -0.49) across models  
 1113 indicating that models which retain a higher fraction of GPP as NPP typically get rid of vegetation  
 1114 carbon sooner via litter fall as indicated by a faster turnover of vegetation (lower  $\tau_{veg}$ ), there by  
 1115 partially compensating for higher  $CUE_{\Delta}$ .

Field Code Changed

1117 Figure 9 investigates the reasons for varying magnitudes of the carbon-climate feedback over  
 1118 land ( $\gamma_L$ ). In equation (9),  $\gamma_L$  is a function of change in land carbon (divided into vegetation and  
 1119 soil+litter components) in the COU relative to the BGC simulation and the temperature change  
 1120 in the COU simulation ( $T'$ ). Over land, the higher temperatures in the COU relative to the BGC  
 1121 simulation affect both autotrophic and heterotrophic respiratory fluxes, from live and dead  
 1122 vegetation pools, respectively, but also gross photosynthesis rates. The primary effect of this  
 1123 temperature change in COU versus the BGC simulation is the loss of carbon from the soil+litter  
 1124 carbon pool (hence the negative sign of  $\gamma_L$  for most models, Figure 6b and 6d) but changes in the  
 1125 vegetation carbon pool also occur. Although  $\gamma_L$  also depends on  $T'$ , Figure 9 arranges models in  
 1126 order from largest to smallest loss of land carbon in COU relative to the BGC simulation to  
 1127 illustrate the varying response of the models. This ordering of models changes slightly if the

Deleted: While Figure 9 investigates reasons for differences among models that lead to different values of their carbon-concentration feedback over land ( $\beta_L$ ),

Deleted: 10

Deleted: 10

1133 carbon loss (or gain in the CanESM5 model) is divided by the temperature change  $T'$  in the COU  
1134 simulation (yielding the value of  $\gamma_L$  which assumes  $T^*=0$  as in equation 9).

1135

1136 As shown in Figure 9, all models lose carbon from the soil+litter carbon pool but with widely  
1137 varying magnitudes. Although typically smaller than the change in soil+litter carbon pool, the  
1138 change in the vegetation carbon pool in the COU relative to the BGC simulation is not of the same  
1139 sign across models. Six of the eleven participating models lose carbon in the vegetation pool in  
1140 the COU relative to the BGC simulation thereby contributing to increasing the absolute  
1141 magnitude of  $\gamma_L$ , while the remaining five exhibit an increase in the vegetation carbon pool  
1142 thereby decreasing the absolute magnitude of  $\gamma_L$ . The largest increase in the vegetation carbon  
1143 pool is seen in the CanESM5 model that more than compensates for the carbon loss from the  
1144 soil+litter carbon pool yielding a positive value of  $\gamma_L$  in contrast to other models. This case is one  
1145 of the few times a positive value of  $\gamma_L$  is seen in an Earth system model. Thornton et al. (2009)  
1146 reported positive  $\gamma_L$  after their first attempt to include N cycle in the CLM. Preliminary analysis  
1147 of CanESM5 data shows the increase in vegetation carbon, in the COU relative to the BGC  
1148 simulation, is caused by the increase in GPP and the resulting vegetation growth at mid-to-high  
1149 latitudes in response to warming temperatures and increasing CO<sub>2</sub>. Interestingly, this response  
1150 is not seen at 2×CO<sub>2</sub> (see Table A1 in the Appendix), and  $\gamma_L$  is still negative for CanESM5.

1151

1152 The loss in land carbon in the COU relative to the BGC simulation (except the CanESM5 model  
1153 that gains carbon), indicated by the orange bar in Figure 9, is strongly correlated with the carbon

Deleted: 10

Deleted: (

Deleted: .,

Deleted: doesn't happen

Deleted: . At 2×CO<sub>2</sub>

Deleted: 10

1160 gain in the BGC simulation (Figure [A1, panel e](#)) (correlation is 0.59 for all models and 0.87 when  
 1161 CanESM5 is excluded) but not with the absolute amount of total land carbon. Figure [A3](#) in the  
 1162 appendix shows the absolute amount of carbon in soil+litter and vegetation pools, and their  
 1163 change from the beginning, for the BGC simulation. The models vary widely in terms of the  
 1164 absolute size of the carbon pools, especially for the soil+litter pool. There are two implications of  
 1165 models losing more carbon in the COU relative to BGC simulation when they take up more carbon  
 1166 in the BGC simulation alone. First, the transient behaviour of a model is determined primarily by  
 1167 its response [to](#) CO<sub>2</sub> and temperature perturbations and not by the absolute amount of land  
 1168 carbon. Second, that carbon-concentration ( $\beta_X$ ) and carbon-climate ( $\gamma_X$ ) feedback parameters  
 1169 must be correlated as well. Indeed, this is the case over land for both CMIP5 and CMIP6 models,  
 1170 but also true for ocean [feed](#)backs although the correlations are somewhat weaker over the  
 1171 ocean. These correlations are shown in Table 3 and are negative since higher positive values of  
 1172  $\beta_X$  are correlated with higher negative values of  $\gamma_X$  indicating that models that take up more  
 1173 carbon with increasing CO<sub>2</sub> also release more carbon when they “see” the associated higher  
 1174 temperatures.

Deleted: 4

Deleted: 2

Deleted: of

1175

#### 1176 4.4.2 Ocean

1177 The time-integrated air-sea flux of carbon provides the dominant contribution to the increase in  
 1178 the global ocean carbon through changes in the DIC inventory. However, the global ocean carbon  
 1179 inventory is also affected by the land to ocean carbon flux from river runoff, and the carbon burial  
 1180 in ocean sediments (see Table A2 in the appendix).

1184

1185 Ocean carbon cycle feedbacks are defined in terms of ocean carbon inventory changes for the  
1186 COU simulation, and the differences in COU relative to the BGC simulation. To fully understand  
1187 the ocean carbon-cycle feedbacks, it is necessary to understand the ocean carbon distributions  
1188 for the pre-industrial and then analyze the carbon anomalies relative to the pre-industrial for  
1189 these climate model experiments.

Deleted: preindustrial

Deleted: preindustrial

1190

#### 1191 4.4.2.1 Ocean carbon distribution

1192 The ocean dissolved inorganic carbon distribution, DIC, is controlled by a combination of physical,  
1193 chemical and biological processes. For the pre-industrial period, there is less DIC in warmer  
1194 waters of the upper ocean and more DIC in colder mid-depth and bottom waters (Figure 10a,  
1195 11a); illustrated here for UKESM1-0-LL as a representative example and Figs S1 to S7 show similar  
1196 distributions for all the diagnosed Earth system models. The vertical extent of the low DIC follows  
1197 the undulations of the thermocline, which is defined by strong vertical temperature and density  
1198 gradients, and is deeper over the subtropical gyres at 30°N and 30°S, and shallower in the  
1199 equatorial zone and at high latitudes. The greater DIC at depth is a consequence of greater  
1200 solubility in colder waters and the accumulation of DIC from the regeneration of organic matter.

Deleted: preindustrial

Deleted: 1

Deleted: 2

Deleted:

Deleted:

1201

1202 To gain insight into how the ocean carbon distribution is controlled, the DIC is separated into  
1203 three pools,  $DIC_{sat}$ ,  $DIC_{disequib}$ , and  $DIC_{regenerated}$ , as defined earlier. The DIC distribution for both

1211 the pre-industrial period and after 140 years in the 1pctCO2 simulation reveal the following key  
1212 features for each of these carbon pools (Figures 10a,b and 11a,b):

- 1213 • The saturated carbon pool provides the dominant contribution to the DIC, holding more than  
1214  $2.15 \text{ mol C m}^{-3}$ , particularly within cooler waters below the thermocline;
- 1215 • The regenerated carbon pool enhances the carbon stored below the surface waters, typically  
1216 providing an additional  $0.2 \text{ mol C m}^{-3}$  within the Southern Ocean and older waters spreading  
1217 from the Southern Ocean into the Atlantic and below the thermocline in the Pacific;
- 1218 • The disequilibrium carbon is small close to the surface, representing waters close to an  
1219 equilibrium with the atmosphere. There is sometimes a positive disequilibrium of up to  $0.05$   
1220  $\text{mol C m}^{-3}$  in some surface waters, which is associated with upwelling transferring carbon-rich  
1221 deeper waters to the surface. The disequilibrium carbon is more strongly negative below the  
1222 thermocline, typically reaching  $-0.1 \text{ mol C m}^{-3}$  in the Atlantic and  $-0.02 \text{ mol C m}^{-3}$  in the  
1223 Southern Ocean and Pacific. In the pre-industrial, the undersaturation in carbon below the  
1224 thermocline is due to the subduction of cold waters at high latitudes that have not  
1225 equilibrated fully with the atmosphere, which then spread by advection along density  
1226 surfaces. In the model integrations reaching year 140, the carbon below the thermocline  
1227 become further undersaturated relative to the contemporary atmosphere due to the rapid  
1228 rise in  $[\text{CO}_2]$ .

1229  
1230 Next we consider the anomalies in the DIC at year 140 in the COU configurations of the 1pctCO2  
1231 simulation calculated relative to the pre-industrial period. The carbon anomaly,  $\Delta \text{DIC}$ , in the  
1232 COU configuration is positive over the upper thermocline over the Atlantic and Pacific basins,

Deleted: preindustrial

Deleted: 1

Deleted: 2

Deleted:

Deleted:

Deleted:

Deleted: preindustrial

Deleted: preindustrial

1241 reaching  $+0.3 \text{ mol C m}^{-3}$ , coinciding with regions that are well ventilated. This gain in carbon is  
1242 made up of an increase in the saturated carbon over all depths due to higher atmospheric  $\text{CO}_2$ .

1243 There is a dipole in the disequilibrium anomaly (Figures 10b,c and 11b,c), generally weakly  
1244 positive in the upper ocean and more strongly negative in deeper waters below the thermocline  
1245 reaching up to  $-0.2 \text{ mol C m}^{-3}$ . This negative disequilibrium anomaly in deeper waters is smallest  
1246 in the relatively well-ventilated mid-depth waters of the North Atlantic, but extends over nearly  
1247 all of the more poorly ventilated mid-depth waters of the Pacific (Figures 10b and 11b).

1249 The regenerated carbon anomaly is relatively small in magnitude reaching less than  $0.05 \text{ mol C}$   
1250  $\text{m}^{-3}$  and varies regionally, enhanced within much of the North Atlantic and the thermocline of the  
1251 Pacific, but with little change in the deep waters of the Pacific (Figures 10b and 11b). The increase  
1252 in regenerated carbon is due to a weakening of ocean overturning leading to an increase in  
1253 residence time and an associated accumulation of DIC from the regeneration of biologically-  
1254 cycled carbon (Bernardello et al., 2014; Schwinger et al., 2014). The regenerated carbon signal  
1255 does not change in the mid depths and deep Pacific as 140 years is too short an integration  
1256 timescale for any effect to be detected.

1257  
1258 To diagnose the carbon-cycle feedback parameters, the ocean carbon response needs to be  
1259 considered for the BGC configuration where there is only limited warming from the increase in  
1260 atmospheric  $\text{CO}_2$  and therefore limited change in climate and ocean circulation. The resulting DIC  
1261 anomalies are generally very similar to those for the COU configuration (Figures 10b,c and 11b,c),

Deleted: 1

Deleted: 2

Deleted:

Deleted: 1

Deleted: 2

Deleted: 1

Deleted: 2

Field Code Changed

Deleted:

Deleted: no additional

Deleted:

Deleted: 1

Deleted: 2

1274 which is to be expected as the dominant effect for the ocean carbon response is the enhanced  
1275 ocean uptake of carbon in response to the increase in [CO<sub>2</sub>]. There is a weakening in ventilation  
1276 in the COU configuration due to the additional radiative forcing. In comparison, in the BGC  
1277 configuration, there is no change in the circulation as there is no radiative warming effect, so that  
1278 there is slightly more carbon uptake in the northern North Atlantic, such as revealed at around  
1279 50°N, compared with the COU configuration. For the BGC configuration, the saturated carbon  
1280 pool is slightly greater at depth due to the water masses being cooler than in the COU  
1281 configuration, the disequilibrium anomaly shows a less negative anomaly in the northern North  
1282 Atlantic because there is little or no change in ventilation, and there are only slight differences in  
1283 the regenerated pool.

1284

1285 The climate response to rising [CO<sub>2</sub>] is now considered in terms of the difference in the COU and  
1286 BGC configurations, which includes the combined effects of warming and circulation changes  
1287 (Figures 10d and 11d). The surface warming drives a decrease in solubility, an increase in  
1288 stratification and a reduction in ventilation, which leads to an overall decrease in carbon uptake  
1289 over the Southern Ocean and Pacific basins, and much of the Atlantic basin. There is a decrease  
1290 in the saturated carbon pool associated with the warming acting to inhibit carbon uptake. The  
1291 regenerated carbon anomaly is enhanced in the deep northern North Atlantic and in the  
1292 Southern Ocean. The regenerated carbon anomaly for this climate response is very similar to that  
1293 for the COU configuration, suggesting that the regenerated carbon anomaly is mainly due to  
1294 circulation changes: the gain in regenerated carbon anomaly is consistent with the expected  
1295 longer residence time from a weaker overturning and ventilation. There is a more negative

Deleted: 1

Deleted: 2

1298 disequilibrium anomaly in the deep waters of the North Atlantic, which is a consequence of  
1299 weaker ventilation.

1300

1301 To gain more insight into the disequilibrium response, the ocean DIC response is also considered  
1302 for the radiatively-coupled integration (RAD), where there is no increase in  $[\text{CO}_2]$ . The additional  
1303 warming leads to a weakening in the overturning, which enhances the residence time in the  
1304 surface waters and so generally decreases the magnitude of the disequilibrium anomaly in the  
1305 North Atlantic (Figure S8), making the disequilibrium less negative relative to the ~~pre-industrial~~  
1306 and so forming a positive disequilibrium anomaly at year 140. In comparison the COU-BGC  
1307 captures the effect of the warming under rising  $[\text{CO}_2]$  leading to the disequilibrium anomaly  
1308 instead becoming more negative at depth, since the weakening in the ventilation leads to more  
1309 of the anthropogenic carbon remaining at the surface rather than being transferred into the  
1310 deeper ocean (Schwinger et al., 2014).

Deleted: preindustrial

Field Code Changed

1311

#### 1312 4.4.2.2 Changes in ocean carbon pools for diagnosing feedback parameters

1313 The ocean carbon-concentration feedback parameter,  $\beta_O$ , is diagnosed from the changes in the  
1314 ocean carbon inventories for the BGC configuration, which does not include radiative warming  
1315 due to increasing  $[\text{CO}_2]$  (equation 13). There is a consistent increase in ocean carbon storage  
1316 across all models with a model mean value of around 670 PgC (Figure 12, light blue bars). This  
1317 increase in ocean carbon storage is made up of an increase in the saturated carbon inventory,  
1318  $\Delta C_{\text{sat}}$ , by about 3100 PgC from the increase in  $[\text{CO}_2]$  (Figure 12, red bars). This increase is partly

Deleted: 3

Deleted: 3



1322 offset by a more negative disequilibrium carbon,  $\Delta C_{disequilib}$ , of typically -2500 PgC (Figure 12,  
 1323 dark blue bars), representing how the ocean carbon uptake cannot keep up with the rate of  $[CO_2]$   
 1324 increase. There is relatively little change in the regenerated carbon inventory,  $\Delta C_{regenerated}$ . The  
 1325 resulting  $\beta_o$  is positive and mainly explained by the chemical response involving the rise in ocean  
 1326 saturation with no significant biological changes, although the physical uptake of carbon within  
 1327 the ocean is unable to keep pace with the rise in  $[CO_2]$ .

Deleted: 3

1329 The ocean carbon-climate feedback parameter,  $\gamma_o$ , is diagnosed from the difference between  
 1330 the COU model configuration and the BGC configuration, and so includes the effect of an  
 1331 increasing surface warming under rising  $[CO_2]$  (equation 14). There is a broadly consistent  
 1332 response across models, with a model mean decrease in carbon inventory of around 80 PgC due  
 1333 to the additional warming in the COU configuration relative to the BGC configuration (Figure 13,  
 1334 light blue bars). The effect of this additional warming and the associated climate change leads to  
 1335 a decrease in both the saturated carbon and disequilibrium carbon of typically -60 and -70 PgC  
 1336 (Figure 13, orange and dark blue bars), representing the decrease in solubility and decreased  
 1337 ocean ventilation. There is an increase in the regenerated carbon of typically 50 PgC (Figure 13,  
 1338 green bars), which is due to a weaker circulation leading to a longer residence time of  
 1339 thermocline and deep waters, so that there is more time for the accumulation of regenerated  
 1340 carbon below the mixed layer. The resulting  $\gamma_o$  is negative, indicating that the ocean takes up  
 1341 less carbon in response to the combination of surface warming and a weakening in ocean  
 1342 ventilation. This response involves a combination of chemical, physical and biological changes  
 1343 where the warming reduces the solubility of the carbon in the ocean and a weakening in the

Deleted:

Deleted: 4

Deleted: 4

Deleted: 4

1349 circulation decreases the disequilibrium pool, but lengthens the residence time and so increases  
1350 the regenerated pool.

1351

1352 Overall, the ocean carbon inventory increases in the BGC configuration by  $666 \pm 53$  Pg\_C (model  
1353 mean  $\pm$  ensemble standard deviation), and decreases in COU relative to BGC by  $-80 \pm 15$  Pg\_C. The  
1354 resulting  $\beta_O$  is very similar across all the models ( $0.78 \pm 0.06$  Pg\_C ppm<sup>-1</sup>), reflecting the strong  
1355 control of carbonate chemistry by rising atmospheric CO<sub>2</sub> (Katavouta et al., 2018) but also the  
1356 use of similar carbonate chemistry schemes and bulk parameterizations of air-sea CO<sub>2</sub> fluxes  
1357 across marine biogeochemical models (Séférian, R., et al., 2020: Tracking improvement in  
1358 simulated marine biogeochemistry between CMIP5 and CMIP6, Current Climate Change Reports,  
1359 in revision). The dominant contributions are composed of a positive contribution from the  
1360 saturated carbon ( $3.66 \pm 0.16$  Pg\_C ppm<sup>-1</sup>) and a negative contribution from the disequilibrium  
1361 carbon ( $-2.98 \pm 0.16$  Pg\_C ppm<sup>-1</sup>) (see Table A3 in the Appendix); these inter-model differences  
1362 are relatively small with ratios of the standard deviation to model mean of only 0.05 and 0.06  
1363 respectively. The regenerated contribution is over two orders of magnitude smaller than the sum  
1364 of the saturated and disequilibrium contributions, and so may be neglected for evaluating  $\beta_O$ .

1365

1366 The values of  $\gamma_O$  differ more strongly across the models ( $-16.95 \pm 5.62$  Pg\_C °C<sup>-1</sup>) and arise from  
1367 differences in the extent of the surface warming and the dynamical changes in the ocean  
1368 circulation and resulting changes in ventilation, residence time and biological regeneration (Table  
1369 A3). The contributions to  $\gamma_O$  include negative contributions from the saturated ( $-12.78 \pm 2.50$  Pg

Deleted:

Field Code Changed

1371 C °C<sup>-1</sup>) and disequilibrium (-16.36±5.31 Pg\_C °C<sup>-1</sup>) components, which are partly opposed by a  
 1372 positive contribution from the regenerated component (12.25±8.53 Pg\_C °C<sup>-1</sup>). The largest  
 1373 intermodel differences are in the regenerated and disequilibrium responses and a relatively small  
 1374 spread in the saturated response, with the ratios of the standard deviation to the model mean  
 1375 are 0.70, 0.33 and 0.20 respectively (Table A3).

1376

#### 1377 4.5. Transient climate response (TCR) and transient climate response to cumulative 1378 emissions (TCRE)

1379

1380 The idealized 1pctCO2 simulation is also used for calculating two other climate metrics routinely.  
 1381 The first is the transient climate response (TCR) which is defined as the temperature change,  
 1382 relative to the pre-industrial state, at the time of CO<sub>2</sub> doubling ( $\Delta T_{2\times CO_2}$ ), that occurs at 70 years  
 1383 after the start of the simulation. The second is the transient climate response to cumulative  
 1384 carbon emissions (TCRE) which is defined as the ratio of TCR to cumulative fossil fuel emissions  
 1385 also at the time of CO<sub>2</sub> doubling ( $\tilde{E}_{2\times CO_2}$ ) (Matthews et al., 2009) typically expressed in units of  
 1386 °C/EgC (1 EgC = 1000 PgC).

$$1387 \quad TCRE = \frac{\Delta T_{2\times CO_2}}{\tilde{E}_{2\times CO_2}} \quad (21)$$

1388 It has been shown that TCRE is approximately constant over a wide range of cumulative emissions  
 1389 and emission pathways (MacDougall, 2016). Although non-CO<sub>2</sub> GHGs and other climate forcings  
 1390 (e.g. aerosols and land use change) also affect the realized warming, TCRE is a considered to be

**Deleted:** Other than the feedbacks associated with the coupled carbon cycle and climate system, t

**Deleted:** preindustrial

**Deleted:** diagnosed

**Field Code Changed**

**Field Code Changed**

**Deleted:** Therefore, a

1396 a straightforward measure of peak warming caused by anthropogenic CO<sub>2</sub> emissions. The TCRE  
 1397 metric has gained significant policy relevance (Frame et al., 2014; IPCC, 2014; Millar et al., 2016)  
 1398 and it is a central component of frameworks used to calculate the remaining allowable carbon  
 1399 emissions to reach a specified temperature change target above the pre-industrial level (Millar  
 1400 et al., 2017; Rogelj et al., 2018, 2019).

Moved (insertion) [3]

Field Code Changed

Deleted: preindustrial

Field Code Changed

1402 Table 4 lists TCR,  $\tilde{E}_{2 \times CO_2}$ , and TCRE from the eleven CMIP6 models considered in this study. We  
 1403 calculate TCR, following the standard approach, as the average temperature of 20 years (year 60-  
 1404 79) centered on the year when CO<sub>2</sub> doubles (year 70). The mean  $\pm$  standard deviation for TCR,  
 1405  $\tilde{E}_{2 \times CO_2}$ , and TCRE from the eleven CMIP6 models considered here are  $1.97 \pm 0.39$  °C,  $1121 \pm 73$   
 1406 PgC, and  $1.77 \pm 0.37$  °C EgC<sup>-1</sup>, respectively. For fifteen CMIP5 models, Gillett et al. (2013)  
 1407 calculated TCRC to be  $1.63 \pm 0.48$  °C EgC<sup>-1</sup> and a 5%-95% range for its observationally constrained  
 1408 value as 0.7-2.0 °C EgC<sup>-1</sup>. The CMIP5 and CMIP6 mean values quoted are not statistically different  
 1409 given the small sample size of available models, some of which duplicate processes or  
 1410 components.

Deleted: ¶

We do not discuss here TCR and TCRC in detail since the focus of our study is on carbon feedbacks. However, both these quantities are readily calculated using results presented in this study.

Deleted: A

Deleted: in the appendix

Deleted:

Formatted: Subscript

Deleted: range

Deleted: 9

Deleted: 44

Deleted: 3

Deleted: 8

Deleted: 41

Field Code Changed

Deleted: (

Deleted: .,

Deleted: the mean  $\pm$  standard deviation range for

**Moved up [3]:** The TCRC metric has gained significant policy relevance (Frame et al., 2014; Millar et al., 2016) and it is used to calculate the remaining allowable carbon emissions to reach a specified temperature change target above the preindustrial level (Millar et al., 2017; Rogelj et al., 2019).

1439 with land N-cycle total  $1088 \pm 34$  PgC compared to  $1160 \pm 91$  PgC for models without N-cycle  
 1440 (from Table 4). For the results reported here from eleven CMIP6 models, however, the  
 1441 uncertainty in TCR (mean  $\pm$  standard deviation =  $1.97 \pm 0.39$  °C), as indicated by standard  
 1442 deviation normalized by mean, is three times as big as the uncertainty in  $\tilde{E}_{2 \times CO_2}$  ( $1121 \pm 73$  PgC).  
 1443 As a result, TCR contributes about 90% of the total variance in the calculated TCRC value ( $1.77 \pm$   
 1444  $0.37$  °C EgC<sup>-1</sup>) (see section A6 in the Appendix).

1446 The TCRC may also be expressed in terms of a product of a thermal contribution from the  
 1447 dependence of surface warming on radiative forcing and a carbon contribution from the  
 1448 dependence of radiative forcing on cumulative carbon emissions (Williams et al., 2016; Katavouta  
 1449 et al., 2018), as

$$TCRC = \frac{\Delta T_{2 \times CO_2}}{\Delta R_{2 \times CO_2}} \frac{\Delta R_{2 \times CO_2}}{\tilde{E}_{2 \times CO_2}} \quad (22)$$

1451 where  $\Delta R_{2 \times CO_2}$  is the change in radiative forcing relative to the pre-industrial period. For a suite  
 1452 of ten CMIP5 models, (Williams et al., 2017) show that the inter-model spread in the TCRC  
 1453 calculated from the 1pctCO2 experiment, has a larger contribution from the inter-model  
 1454 differences in the thermal contribution,  $\frac{\Delta T_{2 \times CO_2}}{\Delta R_{2 \times CO_2}}$ , due to climate feedback and ocean heat uptake  
 1455 over the first few decades, but the inter-model differences in the carbon contribution,  $\frac{\Delta R_{2 \times CO_2}}{\tilde{E}_{2 \times CO_2}}$ ,  
 1456 due to land and ocean carbon uptake become of comparable importance after 80 years.

Deleted: models

Deleted: s

Deleted: A

Deleted: Inclusion of N cycle helps to reduce this uncertainty in that and the results presented here indicate that the spread across the land models (in terms of the strength of their feedback parameters and diagnosed cumulative emissions) is smaller for models with N cycle compared to those that do not include N cycle. representation of the nitrogen cycle is helpful in reducing this uncertainty, as indicated by the spread across land models

Deleted: .

Deleted: 9

Deleted: 44

Deleted: its

Deleted: much greater than

Deleted: 3

Deleted: so that

Deleted: uncertainty

Deleted: 8

Deleted: 41

Field Code Changed

Deleted: preindustrial

Field Code Changed

Deleted: is

Deleted: again dominated by

1481 Thus we conclude, as shown by Jones and Friedlingstein (2020), that the contributions to TCRE  
 1482 uncertainty have changed since CMIP5 from being of similar magnitudes due to carbon feedbacks  
 1483 and climate feedbacks, to now being dominated by climate feedbacks. The reduction in spread  
 1484 of land carbon model feedbacks which we are beginning to see in CMIP6 has led to a reduction  
 1485 in spread of TCRE implying that a large fraction of uncertainty in TCRE is now contributed by  
 1486 physical climate system processes that determine TCR. More CMIP6 models include a complete  
 1487 treatment of important processes – notably the terrestrial nitrogen cycle – that determine the  
 1488 airborne fraction and hence  $\tilde{E}_{2 \times CO_2}$ . Reducing the uncertainty in land and ocean carbon uptake  
 1489 across models remains a priority and will contribute to further reducing the uncertainty in the  
 1490 estimates of TCRE on centennial timescales.

**Formatted:** Font: (Default) Calibri, 12 pt

**Deleted:** Jones & Friedlingstein (2020 submitted),

**Formatted:** Font: (Default) Calibri, 12 pt

**Deleted:** s

**Deleted:** a

**Deleted:** meaning

**Deleted:** Although

**Deleted:** more

**Deleted:** e

**Deleted:** and not the biogeochemical processes that determine

**Deleted:** ,

**Deleted:** reducing

**Deleted:** still

1491

## 1492 5. Summary and conclusions

1493 Model intercomparison projects offer several benefits including calculation of model mean  
 1494 response, quantification of the uncertainty based on the spread across models, and how this  
 1495 uncertainty changes over time. The carbon feedback analysis presented here based on the C<sup>4</sup>MIP  
 1496 protocol of experiments (Jones et al., 2016) allows to investigate how feedback strengths have  
 1497 evolved since CMIP5 and also attempts to understand the reasons behind the spread in models.

**Deleted:** that allows modellers to evaluate how their model's response is different from others'

**Deleted:** s

1498

1499 The carbon uptake over land and ocean, in response to increasing atmospheric CO<sub>2</sub>  
 1500 concentration, is well known to be dominated by the positive contribution from the carbon-  
 1501 concentration feedback (Gregory et al., 2009; Arora et al., 2013). The strength of this feedback is

**Field Code Changed**

1516 of comparable magnitudes over land (mean  $\pm$  standard deviation =  $0.97 \pm 0.40$  PgC ppm<sup>-1</sup>) and  
 1517 ocean ( $0.79 \pm 0.07$  PgC ppm<sup>-1</sup>) although the feedback is much more uncertain over land as  
 1518 indicated by the standard deviation across the eleven models considered here. This dominant  
 1519 positive contribution from the carbon-concentration feedback is, however, opposed by the  
 1520 weaker negative carbon-climate feedback that is associated with the climate change that results  
 1521 due to increasing atmospheric CO<sub>2</sub>. The absolute magnitude of this weaker negative feedback is  
 1522 about three times larger, and an order of magnitude more uncertain, over land ( $-45.1 \pm 50.6$  PgC  
 1523 °C<sup>-1</sup>) than over ocean ( $-17.2 \pm 5.0$  PgC °C<sup>-1</sup>). Model estimates of the ocean carbon-concentration  
 1524 feedback are consistent with each other, reflecting the strong control of how carbonate  
 1525 chemistry alters with rising atmospheric CO<sub>2</sub>. There is a relatively wider range in the model  
 1526 estimates of the ocean carbon-climate feedback, particularly in terms of how changes in ocean  
 1527 circulation alter the disequilibrium and regeneration terms. Over land, however, since the  
 1528 carbon-concentration and carbon-climate feedbacks are determined entirely by biological  
 1529 process, which are much less understood, the resulting uncertainty is much higher across land  
 1530 models than across the ocean models. This uncertainty in the strength of carbon-concentration  
 1531 and carbon-climate feedbacks over land is well known (Friedlingstein et al., 2006; Arora et al.,  
 1532 2013). The inclusion of N cycle results in lower absolute strength of the feedback parameters  
 1533 over land. In addition, the land models that include a representation of the N cycle exhibit a  
 1534 reduced spread in their feedback parameters, despite the additional complexity, compared to  
 1535 when all models are considered. This suggests that if all models were to include N limitation of  
 1536 photosynthesis the spread across them will potentially reduce.

**Deleted:** , but

**Deleted:** very

**Field Code Changed**

**Deleted:** but also a reduced spread across

**Deleted:** .

**Moved down [2]:** While the uncertainty in TCRE is dominated by physical processes affecting the thermal response involving climate feedbacks and heat uptake on decadal timescales, a reduction in the uncertainty in land and ocean carbon uptake across models will reduce the uncertainty in the TCRE on centennial timescales.

1548 The additional analyses that we have performed provide insight into the reasons for the diverse  
1549 responses among models, especially for land models. Over land, the diverse response of models  
1550 is found to be primarily due to the wide range of the strength of the CO<sub>2</sub> fertilization effect, the  
1551 fraction of GPP that is converted to NPP, and the residence times of carbon in the live (vegetation)  
1552 and dead (litter plus soil) carbon pools across models. There is more consistency in the response  
1553 of the ocean models, although inter-model differences arise from differences in the ventilation  
1554 and residence time altering the ocean disequilibrium and regenerated carbon.

**Deleted:** The additional analyses that we have performed to gain further insight into the reasons for differences among models provide insight into their diverse response, especially for land models

1556 In regards to TCRE, while its uncertainty is dominated by physical processes affecting the thermal  
1557 response involving climate feedbacks and heat uptake on decadal timescales, a reduction in the  
1558 uncertainty in land and ocean carbon uptake across models will reduce the uncertainty in the  
1559 TCRE on centennial timescales.

**Moved (insertion) [2]**

**Deleted:** W

**Deleted:** the

**Deleted:** in TCRE

1560 Finally, the decision to use fully- and biogeochemically coupled configurations of the 1pctCO2  
1561 experiment as the standard simulations to diagnose carbon cycle and climate system feedbacks  
1562 from should provide consistency and continuity for future versions of Earth system models to be  
1563 compared against their predecessors.

**Deleted:** ¶



1574 **Table 1:** The values of the carbon-concentration ( $\beta$ ) and carbon-climate ( $\gamma$ ) feedback parameters  
1575 can be solved using results from any two combinations of the RAD, BGC and COU versions of an  
1576 experiment as shown in equation (1). In addition, when using results from the BGC and COU  
1577 simulations the effect of temperature change in the BGC simulation ( $T^*$ ) can be neglected, as was  
1578 done in the F06 study, yielding approximate values for  $\beta_X$  and  $\gamma_X$ .

Approach	$\gamma_X$	$\beta_X$
The RAD-BGC approach	$\gamma_X = \frac{\Delta C_X^+}{T^+}$	$\beta_X = \frac{\Delta C_X^*}{c'} - \frac{\gamma_X T^*}{c'}$
The RAD-COU approach	$\gamma_X = \frac{\Delta C_X^+}{T^+}$	$\beta_X = \frac{\Delta C_X'}{c'} - \frac{\gamma_X T'}{c'}$
The BGC-COU approach	$\gamma_X = \frac{\Delta C_X' - \Delta C_X^*}{T' - T^*}$	$\beta_X = \frac{1}{c'} \left( \frac{\Delta C_X^* T' - \Delta C_X' T^*}{T' - T^*} \right)$
The BGC-COU approach with $T^* = 0$	$\gamma_X = \frac{\Delta C_X' - \Delta C_X^*}{T'}$	$\beta_X = \frac{\Delta C_X^*}{c'}$

1582

1583

1584

1585

**Table 2: Primary features of the physical atmosphere and ocean components, and land and ocean carbon cycle components of the eleven participating models in this study.**

Modelling group	CSIRO	BCC	CCCma	CESM	CNRM	GFDL
ESM	ACCESS-ESM1.5	BCC-CSM2-MR	CanESM5	CESM2	CNRM-ESM2-1	GFDL-ESM4
Atmosphere resolution	1.875°x1.25°, L38	1.125°x1.125°, L46	2.81° x2.81°, L49	0.9°x1.25°	T127 (1.4°x1.4°) L91	Cube-sphere C96 (1-degree)
Ocean resolution	1° but finer between 10S-10N and in the Southern Ocean, L50	1° but becoming finer to 1/3° within 30°N - 30°S, L40	1° but becoming finer to 1/3° within 20°N - 20°S, L45.	gx1v7 displaced pole grid (384 x 320 lat x lon)	1°but becoming 0.3° in the Tropics, L75	0.5 degree tri-polar grid
<b>Land carbon/biogeochemistry component</b>						
Model name	CABLE2.4 with CASA-CNP	BCC-AVIM2	CLASS-CTEM	CLM5	ISBA-CTRIP	LM4p1
Number of live carbon pools	3	3	3	22	6	6
Number of dead carbon pools	6	8	2	7	7	4
Number of plant functional types (PFTs)	13	16	9	22	16	6
Fire	No	No	No	Yes	yes	Yes
Dynamic vegetation cover	No	No	No	No	no	Yes
Nitrogen cycle	Yes (and phosphorus)	No	No	Yes	No (implicit, derived from Yin 2002)	No
<b>Ocean carbon/biogeochemistry component</b>						
Model name	WOMBAT	MOM4_L40, Ocean carbon cycle follows OCMIP2	CMOC (biology), carbonate chemistry follows OMIP protocol.	MARBL	PISCESv2-gas	COBALTV2
Number of phytoplankton types	1	0	1	3	2	2
Number of zooplankton types	1	0	1	1	2	3
Explicit nutrients considered	Phosphorus, Iron	Phosphorus	Nitrogen	Nitrogen, Phosphorus, Silica, Iron	Nitrogen, Phosphorus, Silica, Iron	Nitrogen, Phosphorus, Silica, Iron

Formatted Table

Deleted: ¶  
¶  
¶

Modelling group	IPSL	JAMSETC (Team MIROC)	MPI	NCC	UK
ESM	IPSL-CM6A-LR	MIROC-ES2L	MPI-ESM1.2-LR	NorESM2-LM	UKESM1-0-LL
Atmosphere resolution	2.5°x.3°, L79	2.81x2.81, L40	T63, 1.8°x1.8°. L47	1.9°x2.5°, L32	1.875° x1.25°, L85
Ocean resolution	1°-0.3° in the Tropics L75	Almost 1° but becoming finer to North pole and equator (Tripolar system: 360x256), L62	GR1.5 (1.5°, finer close to Antarctica and Greenland), L40	1° with enhanced meridional resolution near the Equator, L53	1°
<b>Land carbon/biogeochemistry component</b>					
Model name	ORCHIDEE, branch 2.0	MATSIRO (physics) VISIT-e (BGC)	JSBACH3.2	CLM5	JULES-ES-1.0
Number of live carbon pools	8	3	3	22	3
Number of dead carbon pools	3	6	18	7	4
Number of plant functional types (PFTs)	15	13	13	22	13
Fire	No	No	Yes	Yes	No
Dynamic vegetation cover	No	No	Yes	No	Yes
Nitrogen cycle	No	Yes	Yes	Yes	Yes
<b>Ocean carbon/biogeochemistry component</b>					
Model name	PISCES-v2	OECO2	HAMOCC6	Modified HAMOCC5.1	MEDUSA-2.1
Number of phytoplankton types	2	2 (non-diazotroph and diazotroph)	2	1	2
Number of zooplankton types	2	1	1	1	2
Explicit nutrients considered	Nitrogen, Phosphorus, Silica, Iron	Nitrogen, Phosphorus, Iron	Nitrogen, Phosphorus, Silica, Iron	Nitrogen, Phosphorus, Silica, Iron	Nitrogen, Silica, Iron

1633

1634 **Table 3:** Correlation between carbon-concentration ( $\beta_x$ ) and carbon-climate ( $\gamma_x$ ) feedback  
1635 parameters over land and ocean across comprehensive ESMs from the CMIP5 intercomparison  
1636 in the A13 study and CMIP6 intercomparison in this study. For land correlation is also shown  
1637 when CanESM5 is excluded from CMIP6 models.

1638

Land	Ocean	
−0.69 −0.92 (excluding CanESM5)	−0.64	CMIP6 (11 models)
−0.82	−0.75	CMIP5 (8 models)

1639

1640

1641 **Table 4:** Transient Climate Response (TCR,  $\Delta T_{2\times CO_2}$ ), diagnosed cumulative emissions at  $2\times CO_2$   
1642 ( $\bar{E}_{2\times CO_2}$ ), and transient climate response to cumulative emissions (TCRE) for the eleven CMIP6  
1643 models considered in this study.

1644

CMIP6 model	TCR (°C)	Cumulative diagnosed emissions (PgC)	TCRE (°C EgC <sup>−1</sup> )
ACCESS-ESM1.5	2.15	1064	2.02
BCC-CSM2-MR	1.70	1291	1.32
CanESM5	2.54	1214	2.09
CESM2	2.29	1073	2.13
CNRM-ESM2-1	1.84	1124	1.63
IPSL-CM6A-LR	2.36	1107	2.13
MIROC-ES2L	1.58	1135	1.39
MPI-ESM1.2-LR	1.86	1127	1.65
NOAA-GFDL-ESM4	1.55	1066	1.45
NorESM2-LM	1.42	1075	1.32
UKESM1-0-LL	2.42	1054	2.30
Mean	1.97	1121	1.77
Sample standard deviation	0.39	72.9	0.37

1645

1646

1647

1648

Moved (insertion) [1]

Deleted: A

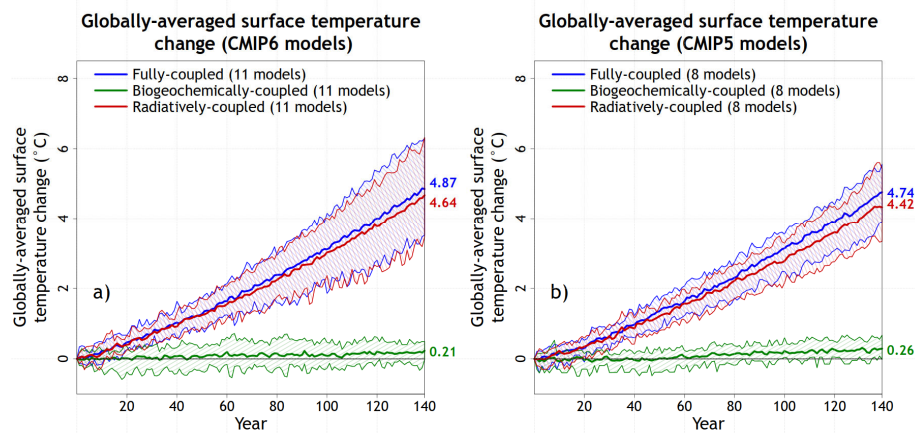
Deleted: S

Deleted: 8

Deleted: 69.5

Deleted: 6

1654  
1655  
1656



1657

1658 Figure 1: Temperature changes in the fully-, biogeochemically- and radiatively-coupled  
1659 configurations of the 1pctCO2 experiment across participating CMIP6 (panel a) and CMIP5 (panel  
1660 b) comprehensive ESMs that participated in this and the Arora et al. (2013) study, respectively.  
1661 Model mean is indicated by the solid lines and the range across the models is indicated by shading  
1662 around the solid lines. Individual CMIP6 model results are shown in Figure A1.

1663

1664

Deleted: ¶

Deleted: 4

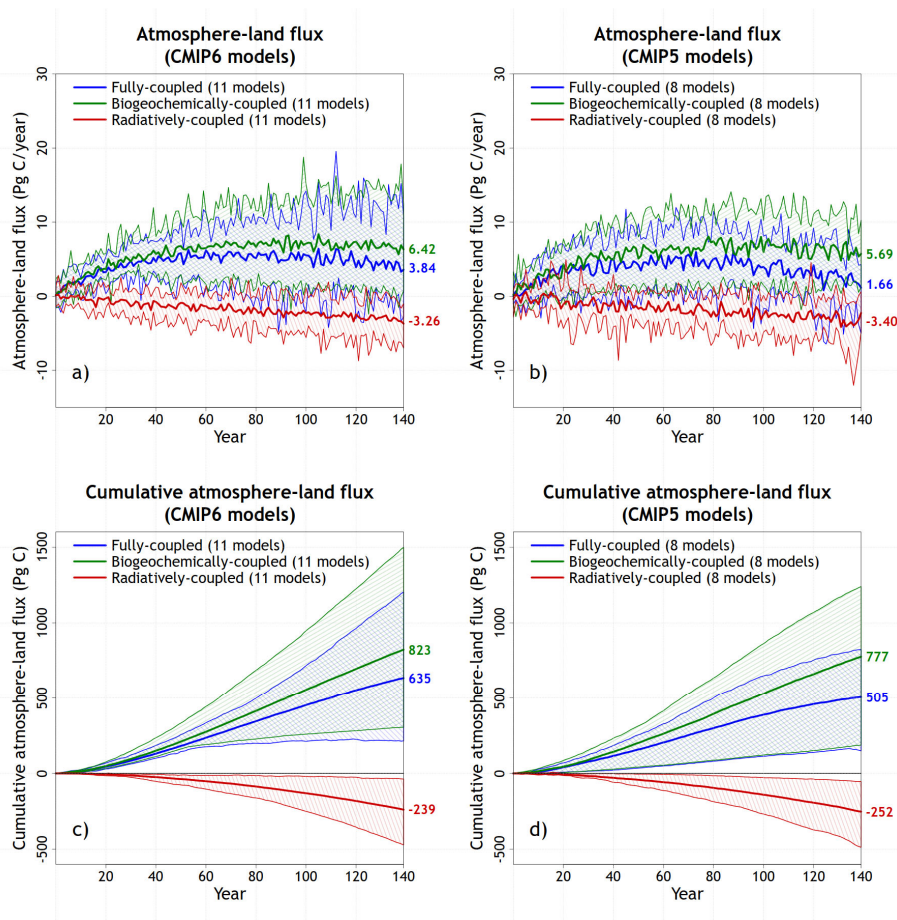
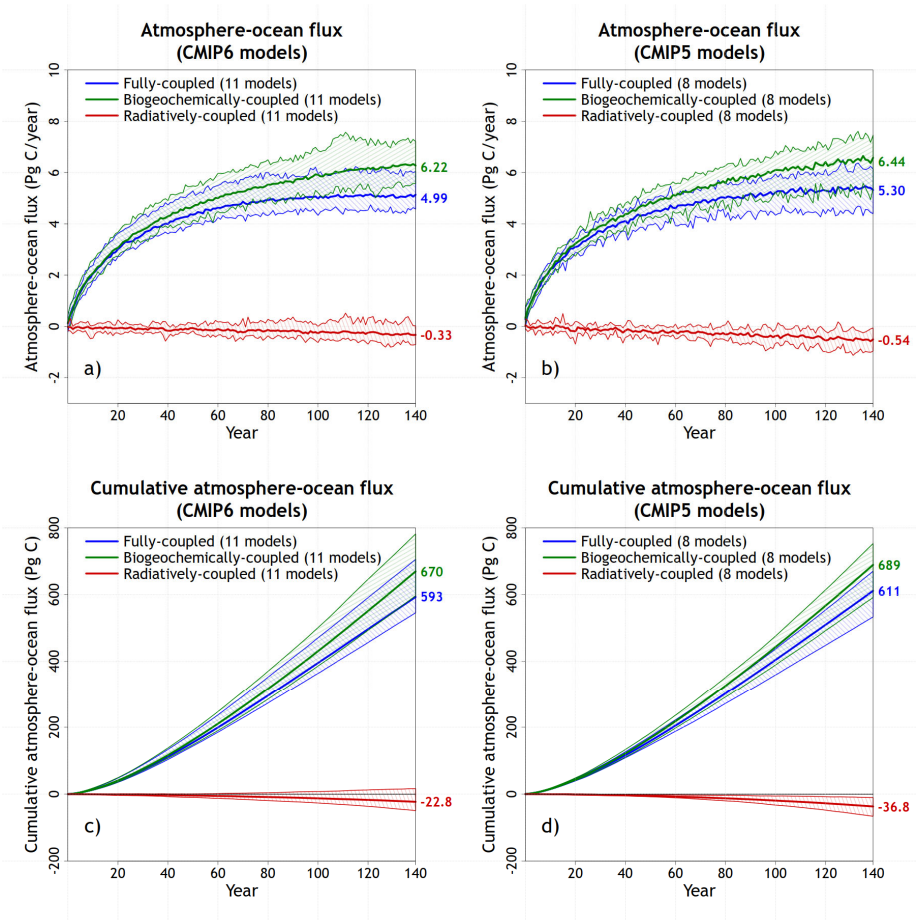


Figure 2: Model mean values and the range across models for annual simulated atmosphere-land CO<sub>2</sub> flux (top row) and their cumulative values (bottom row) for participating CMIP6 (left column) and CMIP5 (right column) models from the fully-, biogeochemically- and radiatively-coupled versions of the 1pctCO<sub>2</sub> experiment. Individual CMIP6 model results are shown in Figure A1.

Deleted: 4



1675

1676

1677

1678

1679

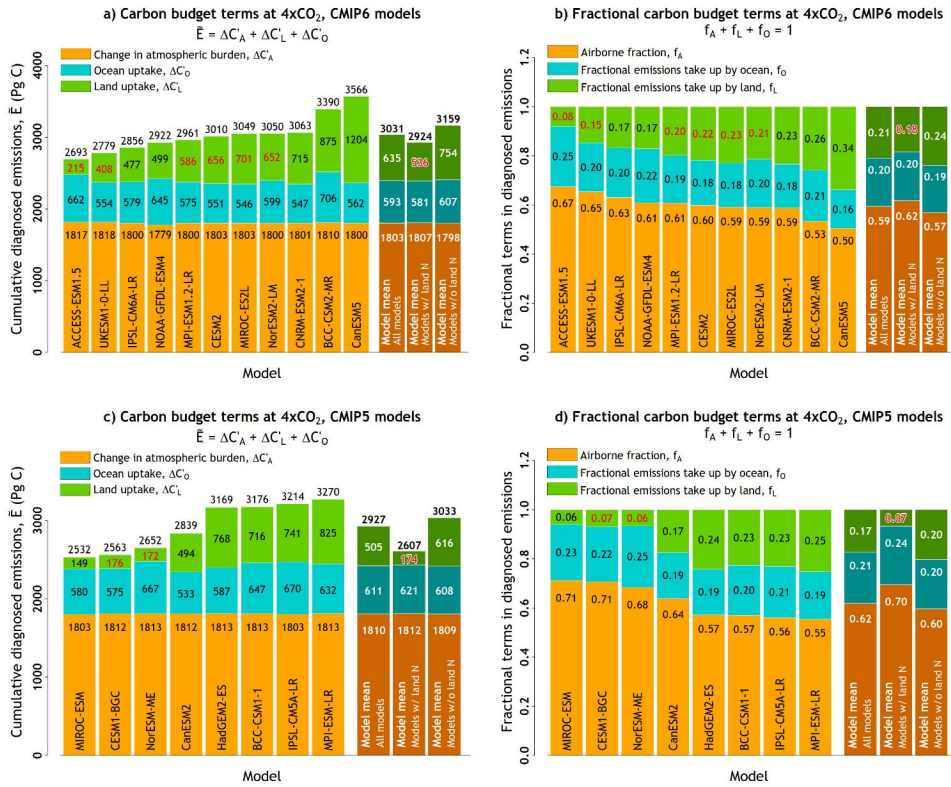
1680

1681

Figure 3: Model mean values and the range across models for annual simulated atmosphere-ocean CO<sub>2</sub> flux (top row) and their cumulative values (bottom row) for participating CMIP6 (left column) and CMIP5 (right column) models from the fully-, biogeochemically- and radiatively-coupled versions of the 1pctCO<sub>2</sub> experiment. Individual CMIP6 model results are shown in Figure A1.

Deleted: <object>  
Deleted: 4  
Deleted: -----Page Break-----  
¶  
<object>Figure 4: Individual model values from CMIP6 models for globally-averaged surface temperature change (top row), cumulative atmosphere-land CO<sub>2</sub> flux (middle row), and cumulative atmosphere-ocean CO<sub>2</sub> flux (bottom row) from the fully-, biogeochemically- and radiatively-coupled versions of the 1pctCO<sub>2</sub> experiment. Results from the radiatively-coupled configuration were not available from NorESM2-LM models at the time of writing.

Figure 4: Components of the carbon budget terms in cumulative emissions from the eleven participating CMIP6 models based on equation (A6) in panel (a) and equation (A7) in panel (b) using results from the fully-coupled 1pctCO2 simulation. The models are arranged in an ascending order based on their cumulative emissions values. Results from participating CMIP5 models in the A13 study are shown in panels c and d. In addition, ESMs whose land component includes a representation of N cycle are identified by red font colour for cumulative land carbon uptake (panels a and c) and fractional emissions taken up by land (panels b and d). Model mean is shown for all models but also separately for models whose land components include or do not include a representation of the N cycle.



Deleted: 5  
Deleted: 15  
Deleted: 16



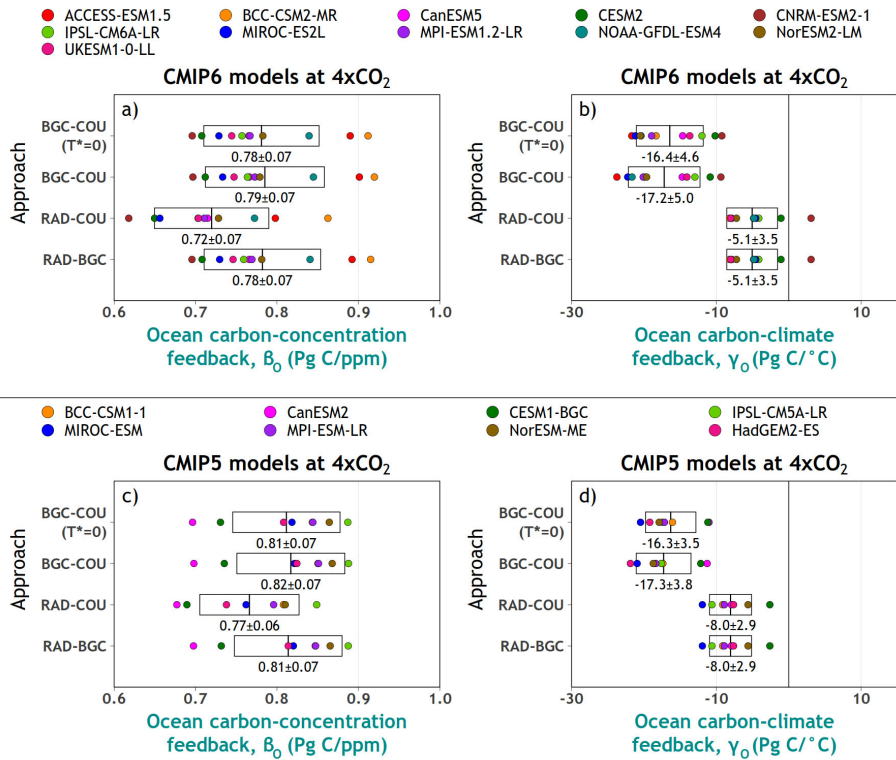


Deleted: ¶

**Deleted: 6**

**Deleted:** Note that among CMIP6 models results from NorESM2-LM were not available for the RAD simulation at the time of writing.

1724



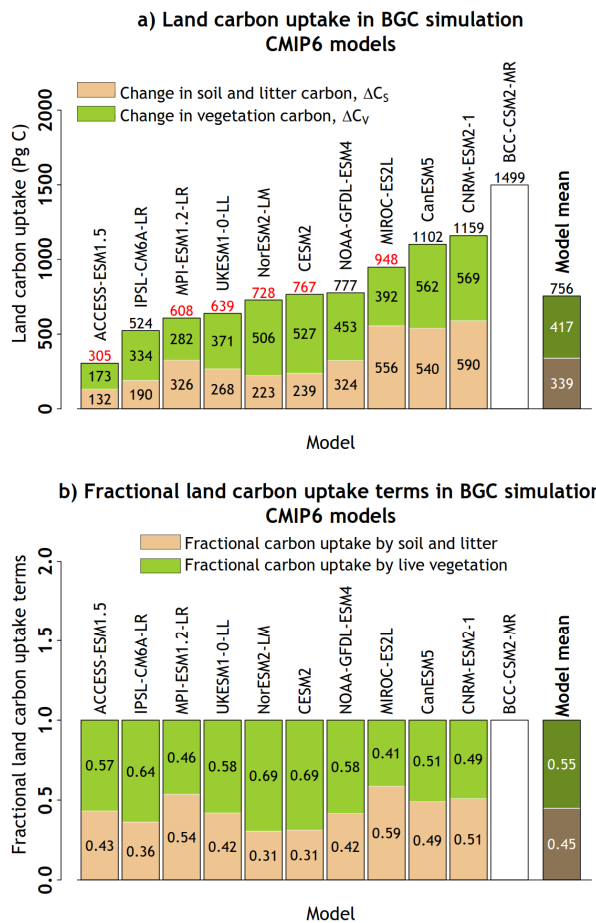
Formatted: Line spacing: Double

1725

1726 Figure 6: Carbon-concentration (panel a) and carbon-climate (panel b) feedback parameters  
1727 over ocean from participating CMIP6 models calculated using the approaches summarized in  
1728 Table 1. The boxes show the mean  $\pm 1$  standard deviation range. Results from participating  
1729 CMIP5 models in the A13 study are shown in panels c and d.

Deleted: 7

Deleted: Note that among CMIP6 models results from NorESM2-LM were not available for the RAD simulation at the time of writing.



1734

1735 Figure 7: Carbon uptake over land in the BGC simulation, used to calculate land carbon-  
 1736 concentration feedback ( $\beta_L$ ) and its partitioning into vegetation and soil+litter carbon pools  
 1737 across the participating CMIP6 models (panel a). Panel (b) shows the fractional land carbon  
 1738 uptake by vegetation and soil+litter carbon pools in the BGC simulation. No partitioning is  
 1739 shown for the BCC-CSM2-MR model because total land carbon uptake in this model exceeded  
 1740 the sum of changes in the vegetation and soil+litter carbon pools by more than 10%. Total land  
 1741 carbon uptake in models which include a representation of the N cycle is shown in red color.  
 1742 The results from the BCC-CSM2-MR model are not used in calculating the model-mean values.

Deleted: 8

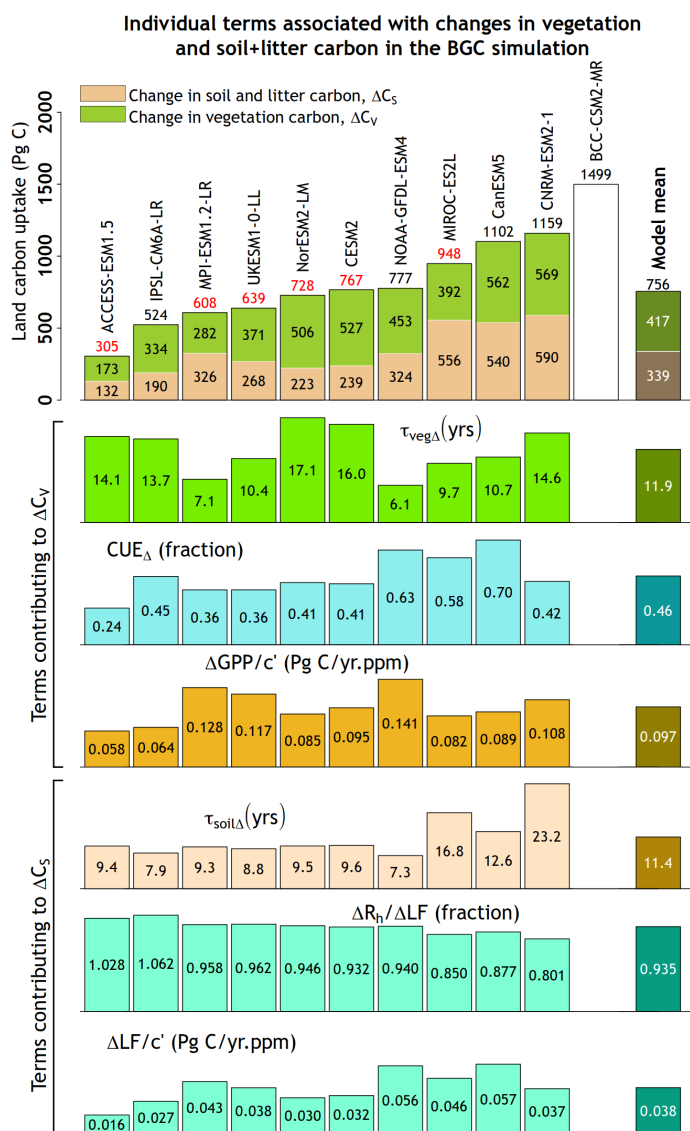
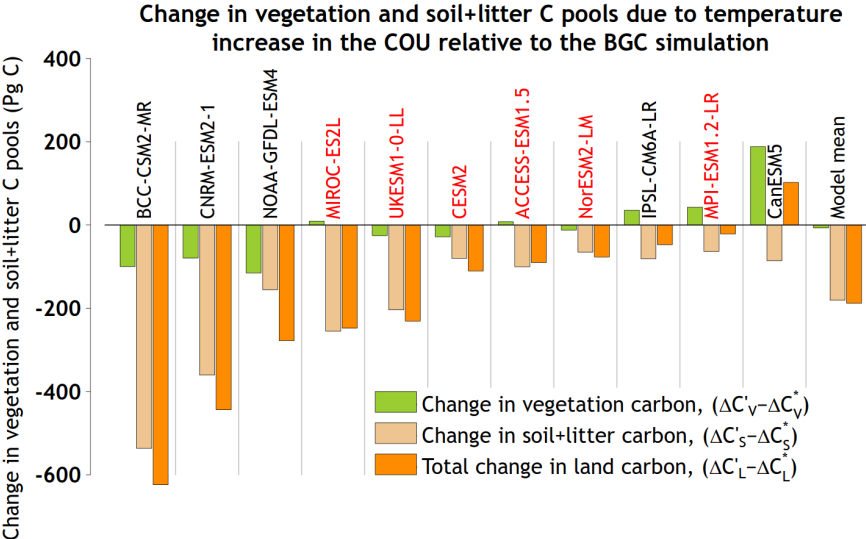


Figure 8: Individual terms of equation (8) which contribute to changes in vegetation ( $\Delta C_v$ ) and litter+soil ( $\Delta C_s$ ) carbon pools. Values from the BCC-CSM2-MR model are not used in calculating the model-mean.

Formatted: Line spacing: Multiple 1.08 li  
 Deleted: 9

1776  
1777  
1778  
1779

Deleted: 11  
Page Break



1780

1781 Figure 9: The changes in vegetation and soil+litter carbon pools in the COU relative to the BGC  
1782 simulation, as shown in equation (9), which contribute to the calculation of carbon-climate  
1783 feedback over land ( $\gamma_L$ ) in the BGC-COU approach. The names of models which include N cycle  
1784 are shown in red font colour.

Deleted: 10

1785

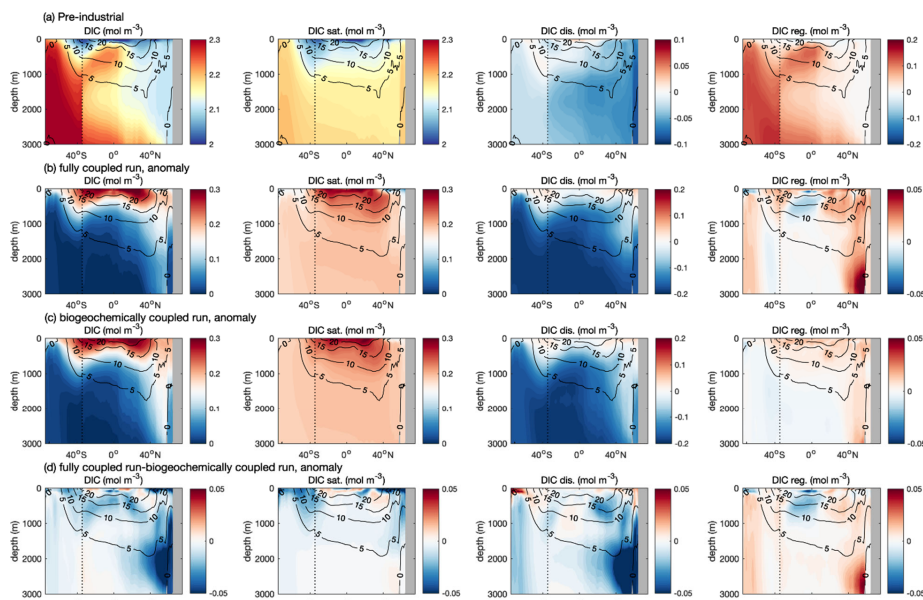


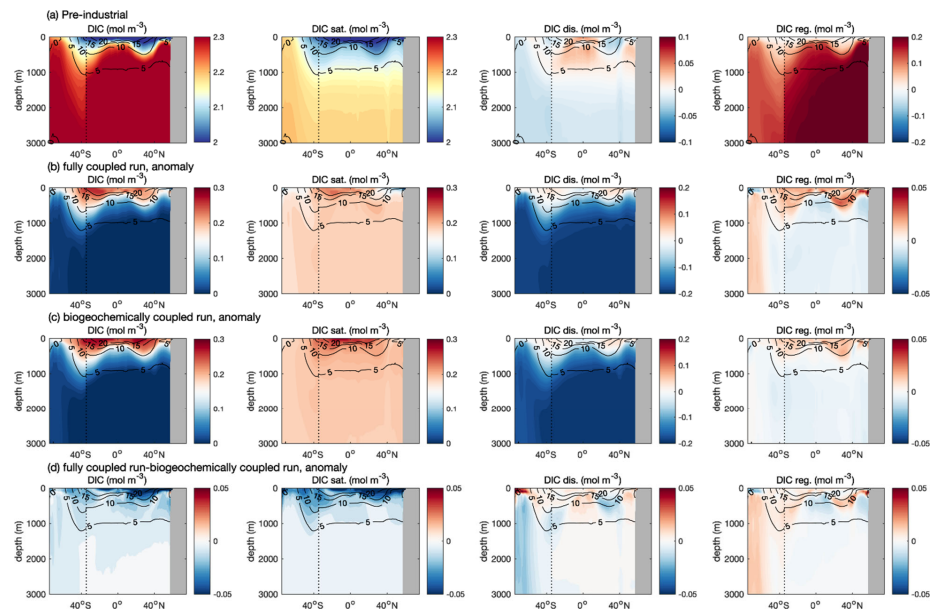
Figure 10. Meridional section of the dissolved inorganic carbon,  $DIC$  ( $\text{mol m}^{-3}$ ), and constituent carbon pools in UK-ESM1-0-LL for the zonally-averaged Atlantic and Southern Ocean: (a) the pre-industrial absolute concentrations, and the anomalies relative to the pre-industrial state at year 140 for (b) the COU configuration, (c) the BGC configuration and (d) the COU minus the BGC configuration. The  $DIC$  is separated into saturated carbon,  $DIC_{\text{sat}}$ , the disequilibrium carbon,  $DIC_{\text{disequib}}$ , and the regenerated carbon,  $DIC_{\text{regenerated}}$ . The Atlantic and Southern Ocean domains are separated by a black vertical line.

Deleted: 1

Deleted: preindustrial

Deleted: preindustrial

1802



1803

1804 Figure 11. Meridional section of the dissolved inorganic carbon,  $DIC$  ( $\text{mol m}^{-3}$ ), and constituent  
1805 carbon pools in UK-ESM1-0-LL for the zonally-averaged Pacific and Southern Ocean: (a) the pre-  
1806 industrial absolute concentrations, and the anomalies relative to the pre-industrial state at year  
1807 140 for (b) the COU configuration, (c) the BGC configuration and (d) the COU minus the BGC  
1808 configuration. The  $DIC$  is separated into saturated carbon,  $DIC_{sat}$ , the disequilibrium carbon,  
1809  $DIC_{disequib}$ , and the regenerated carbon,  $DIC_{regenerated}$ . The Pacific and Southern Ocean domains  
1810 are separated by a black vertical line.

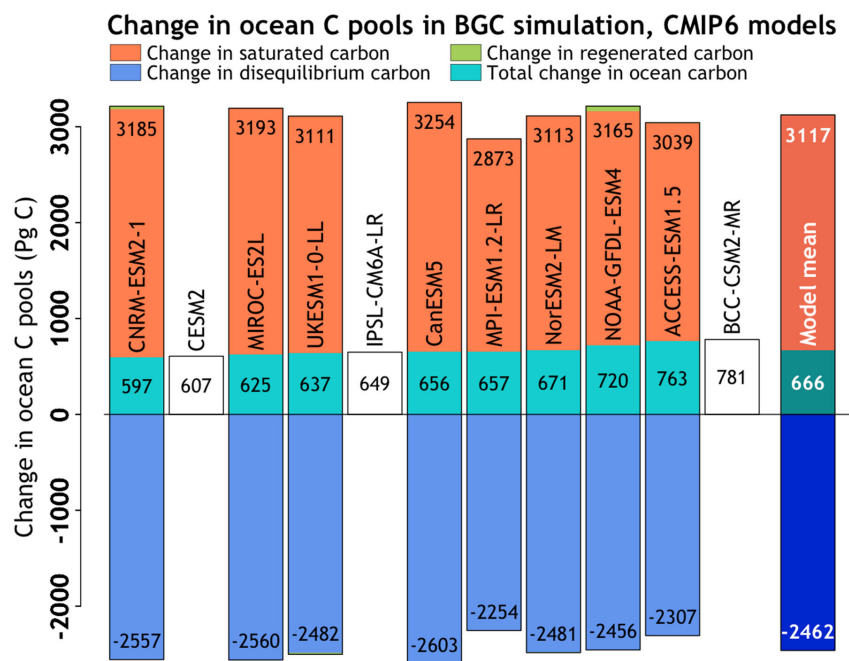
1811

Deleted: 2

Deleted: preindustrial

Deleted: preindustrial

1815



1816

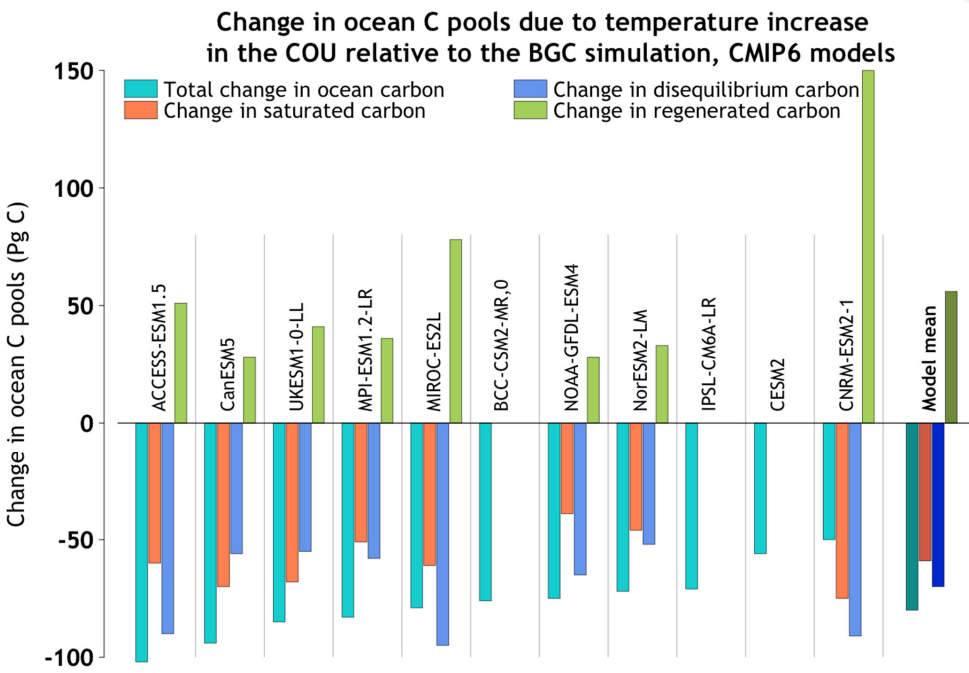
1817 Figure 12. Carbon uptake over the ocean in the biogeochemically-coupled simulation, used to  
1818 calculate ocean carbon-concentration feedback and its partitioning into saturated, disequilibrium  
1819 and regenerated carbon pools across the participating CMIP6 models (left panels) using equation  
1820 (12). No partitioning is shown for models for which 3D ocean fields were not available and the  
1821 results of these models are not used in calculating the model mean values (right panel). The sum  
1822 of the partitions does not exactly match the total ocean uptake diagnosed from the air-sea fluxes  
1823 due to land-ocean interactions involving storage in sediments and river inputs.

Deleted: 3

1824



1826



1827

1828 Figure 13. Change in saturated, disequilibrium and regenerated carbon pools in the fully coupled  
1829 minus the biogeochemical simulation using equation (14), which contribute to the calculation of  
1830 carbon-climate feedback over the ocean. The sum of the partitions does not exactly match the  
1831 total ocean uptake diagnosed from the air-sea fluxes due to land-ocean interactions involving  
1832 storage in sediments and river inputs.

Deleted: 4

Deleted: 2

Deleted: concentration

1833

1837

1838 **Appendix**

1839

1840 **A1. The climate carbon cycle feedbacks framework**

1841

1842 The rate of change of carbon in the combined atmosphere-land-ocean system is written as

1843

1844 
$$\frac{dC_G}{dt} = \frac{dC_A}{dt} + \frac{dC_L}{dt} + \frac{dC_O}{dt} = E \quad (A1)$$

1845

1846 where the Global carbon pool  $C_G = C_A + C_L + C_O$  is the sum of carbon in the Atmosphere, Land

1847 and Ocean components (PgC), and  $E$  is the rate of anthropogenic CO<sub>2</sub> emission (PgC/yr) into the

1848 atmosphere. The equations for the atmosphere, land and ocean are

1849 
$$\begin{aligned} \frac{dC_A}{dt} &= F_A(T, c) + E \\ \frac{dC_L}{dt} &= F_L(T, c) \\ \frac{dC_O}{dt} &= F_O(T, c) \end{aligned} \quad (A2)$$

1850 where  $(F_L + F_O) = -F_A$  are the fluxes between the atmosphere and the underlying land and

1851 ocean, taken to be positive into the components. The fluxes  $F$  are expressed as functions of

1852 surface temperature  $T$  and the surface atmospheric CO<sub>2</sub> concentration  $c$ . Here and subsequently,

1853 uppercase  $C$  denotes carbon pools and lowercase  $c$  denotes atmospheric CO<sub>2</sub> concentration.

1854 In the fully-, biogeochemically-, and radiatively-coupled versions of the 1pctCO<sub>2</sub> experiments  
 1855 analyzed here, the rate of change of atmospheric carbon  $dC_A/dt$  is specified in equations (A1)  
 1856 and (A2). The uptake or release of CO<sub>2</sub> by the underlying land and ocean yields an effective  
 1857 emission  $E$  which serves to maintain the budget.

1858

1859 The changes in atmosphere carbon budgets, from the pre-industrial control simulation, in the  
 1860 differently coupled simulations are represented as

1861

1862 Radiatively-coupled  $\frac{dC'_A}{dt} - E^+ = F_A^+ = -F_L^+ - F_O^+ = \Gamma_A T^+$  (A3a)

1863 Biogeochemically-coupled  $\frac{dC'_A}{dt} - E^* = F_A^* = -F_L^* - F_O^* = \Gamma_A T^* + B_A c'$  (A3b)

1864 Fully-coupled  $\frac{dC'_A}{dt} - E = F'_A = -F'_L - F'_O = \Gamma_A T' + B_A c'$  (A3c)

1865

1866

1867 which serve to define the instantaneous carbon-concentration ( $B_A$ ) and carbon-climate ( $\Gamma_A$ )  
 1868 feedback parameters and assume linearization of the globally integrated surface-atmosphere  
 1869 CO<sub>2</sub> flux in terms of global mean temperature and concentration change. In equation (A3),  $F^+$ ,  
 1870  $F^*$ , and  $F'$  are the flux changes and  $T^+$ ,  $T^*$ , and  $T'$  the temperature changes in the radiatively-,  
 1871 biogeochemically- and fully-coupled simulations, and  $E^+$ ,  $E^*$ , and  $E$  are the resulting implicit  
 1872 emissions.  $c'$  is the specified CO<sub>2</sub> concentration change above its pre-industrial level in the  
 1873 1pctCO<sub>2</sub> simulations. In the biogeochemically-coupled simulation there is no radiative forcing  
 1874 due to increasing CO<sub>2</sub> so  $T^*$  is small, although not zero and exhibits a distinct spatial pattern. The

1875 assumption made in equation (A3) is that the feedback parameters are the same in the three  
1876 cases.

1877

1878 Carbon budget changes for the land component parallel (A3) but without the emissions terms as

1879 Radiatively-coupled  $\frac{dC_L'}{dt} = F_L^+ = \Gamma_L T^+$  (A4a)

1880 Biogeochemically-coupled  $\frac{dC_L^*}{dt} = F_L^* = \Gamma_L T^* + B_L c'$  (A4b)

1881 Fully-coupled  $\frac{dC_L^*}{dt} = F_L' = \Gamma_L T' + B_L c'$  (A4c)

1882

1883 and similarly for the ocean component. Since  $F_A = -(F_L + F_O)$  it follows that  $\Gamma_A = -(\Gamma_L + \Gamma_O)$   
1884 and  $B_A = -(B_L + B_O)$ . There are no terms involving  $c'$  in the radiatively-coupled simulation  
1885 (equations A3a and A4a) since the pre-industrial value of atmospheric CO<sub>2</sub> concentration is  
1886 prescribed for the biogeochemistry components so  $c' = 0$  and does not affect the flux.

1887

1888 The instantaneous feedback parameters ( $B_L$  and  $\Gamma_L$ ) differ from that in the integrated flux  
1889 approach of Friedlingstein et al. (2006) who express time integrated flux changes (i.e. change in  
1890 pool or reservoir sizes) as functions of temperature and CO<sub>2</sub> concentration changes with

1891 Radiatively-coupled  $\int F_L^+ = \Delta C_L^+ = \gamma_L T^+$  (A5a)

1892 Biogeochemically-coupled  $\int F_L^* = \Delta C_L^* = \gamma_L T^* + \beta_L c'$  (A5b)

1893 Fully-coupled  $\int F_L' = \Delta C_L' = \gamma_L T' + \beta_L c'$  (A5c)

1894

1895 and similarly for the ocean component, with the assumption that the  $\Delta C'_O$  term includes changes  
 1896 in the carbon amount of ocean sediment as well.

1897

1898 The units of instantaneous and integrated flux based parameters are different ( $\Gamma$  - PgC yr<sup>-1</sup> °C<sup>-1</sup>,  
 1899  $B$  - PgC yr<sup>-1</sup> ppm<sup>-1</sup> and  $\gamma$  - PgC °C<sup>-1</sup>,  $\beta$  - PgC ppm<sup>-1</sup>). Arora et al. (2013) show how the  
 1900 instantaneous and integrated flux based feedback parameters are related to each other

1901

1902 Integrating equations (A1) and (A2) from initial time to  $t$  gives

1903 
$$\Delta C'_A + \Delta C'_L + \Delta C'_O = \int_0^t E dt = \tilde{E} . \quad (A6)$$

1904 Here  $\Delta C'_A = 2.12 (c(t) - c(0))$  is the change in atmospheric carbon burden (the factor 2.12  
 1905 converts atmospheric CO<sub>2</sub> concentration from ppm to atmospheric burden in PgC) and  $\Delta C'_X =$   
 1906  $\int_0^t F'_X dt$ ,  $X = L, O$  is the cumulative flux equal to the change in the land or ocean carbon pool  
 1907 for the fully-coupled simulation. The terms in equation (A6) indicate the contribution of changes  
 1908 in atmosphere, land and ocean carbon pools to cumulative emissions  $\tilde{E}$ . Finally, division by the  
 1909 cumulative emissions term in equations (A6) gives all the terms in a fractional form as

1910

1911 
$$f_A + f_L + f_O = 1 \quad (A7)$$

1912

Deleted: Wh

1914 where  $f_A$  is the airborne fraction of cumulative emissions and  $f_L$  and  $f_O$  are fractional emissions  
1915 taken up by the land and ocean. These components are evaluated at the time of CO<sub>2</sub> quadrupling.

1916

## 1917 A2. Reasons for non-linearity in the ocean C cycle response in the CNRM-ESM2-1 model

1918

1919 In Figure 6 value of  $\gamma_O$  changes sign for the CNRM-ESM2-1 model from positive when calculated  
1920 using the RAD-BGC or RAD-COU approaches to negative when calculated using the BGC-COU  
1921 approach. This non-linear behaviour for a previous version of the CNRM model has been  
1922 document in Schwinger et al. (2014) and caused by the large increase in regenerated DIC in the  
1923 RAD simulation, similar to the increase in the COU relative to the BGC simulation, as shown in  
1924 Figure 13 for the CNRM-ESM2-1 model. This non-linear behaviour is stronger in CNRM-ESM2-1,  
1925 compared to CNRM-ESM1, its previous version (Séférian et al., 2016), most likely due to a new  
1926 parameterization for N fixation which increases ocean NPP and a revised parameterization for  
1927 organic matter remineralization (in PISCESv2-gas). A contribution to a positive  $\gamma_O$  is also made by  
1928 declining sea ice in the RAD simulation which leads to changes in the sign of the air-sea carbon  
1929 exchange in the Southern Ocean. The vertical profile of dissolved inorganic carbon in the  
1930 Southern Ocean in BGC and COU simulations (with rising [CO<sub>2</sub>]) is different from that in the RAD  
1931 simulation (for the pre-industrial [CO<sub>2</sub>]) and this leads to additional non-linearities.

1932

1933

## 1934 A3. Additional figures and discussion

**Deleted:** Justification for using BGC and COU simulations for finding feedback parameters

**Formatted:** Font: Bold

**Deleted:** Figures 6 and 7 provide justification for using the BGC-COU approach, over the RAD-BGC and RAD-COU approaches, in calculating the feedback parameters as discussed below. In Figure 7, the absolute magnitude of  $\gamma_O$  when using the BGC-COU approach is about twice in CMIP5 models (and more than three times in CMIP6 models) compared to its model-mean value calculated using the RAD-BGC and RAD-COU approaches. The reason for this is that the RAD simulation misses the suppression (due to weakening of the ocean circulation) of carbon drawdown to the deep ocean. This is because there is no buildup of a strong carbon gradient from the atmosphere to the deep ocean in the RAD simulation. This process is important when climate change is forced by increasing atmospheric CO<sub>2</sub>, and therefore feedback parameters calculated using the BGC-COU approach are more likely to include all processes relevant to application for realistic scenarios. In Figure 6, although the carbon-climate feedback parameter over land ( $\gamma_L$ ) is larger in absolute amount, it is comparatively less sensitive to the approach used, than over ocean, because over land an increase in temperature not only increases the respiratory losses but also affects photosynthetic processes especially in conjunction with increasing CO<sub>2</sub>. Warmer temperatures increase photosynthesis over mid to high latitude regions where photosynthesis is currently limited by temperature and more so with increasing CO<sub>2</sub>, but decrease photosynthesis over tropical regions where the temperatures are already too warm for optimal photosynthesis. The net result of these compensating processes plays out very differently in different models and in the model-mean sense this results in less sensitivity of the calculated value of carbon climate feedback parameter over land ( $\gamma_L$ ) to the different approaches than over ocean. This is seen in both CMIP5 and CMIP6 models. When  $\gamma_L$  is calculated using the RAD-BGC and RAD-COU approaches, it is exclusively calculated using results from the RAD simulation. However, since over land photosynthesis is also affected by temperature in addition to respiration (with widely varying responses between models) the  $\gamma_L$  values vary widely between models between the RAD-BGC/RAD-COU approach and the BGC-COU approach. This is seen, for example, for ACCESS-ESM1. ... [3]

**Deleted:** 7

**Deleted:** and this further illustrates the sensitivity of feedback parameters to the approach used to calculate them

**Field Code Changed**

**Deleted:** (

**Deleted:** ,

**Deleted:** 4

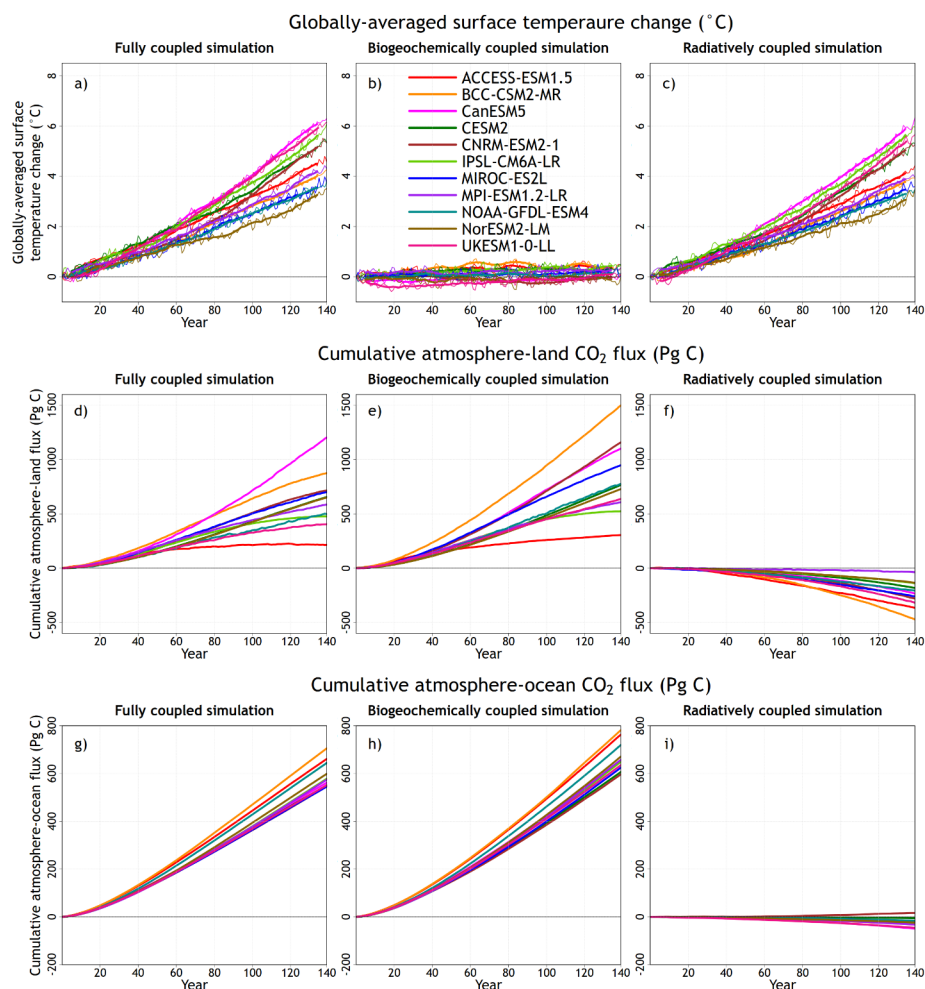
**Deleted:** in the model's ocean biogeochemistry component

**Deleted:** preindustrial

**Deleted:** \_\_\_\_\_ Page Break \_\_\_\_\_

**Deleted:** F

Figure A1 shows results from individual CMIP6 models for which model means and ranges were shown in Figures 1, 2, and 3 and allows identification of models which behave differently compared to the majority of models. In Figure A1, panels a and c, CanESM5 shows the largest temperature increase, and NorESM2-LM and MIROC-ES2L the smallest, in response to increase in [CO<sub>2</sub>] for the COU and RAD simulations, respectively. For cumulative atmosphere-land CO<sub>2</sub> flux in the COU simulation (panel d), CanESM5 simulates the largest land carbon uptake and ACCESS-ESM1.5 the smallest. This is not the case for the BGC simulation (panel e) where land carbon uptake from the BCC-CSM2-MR and CNRM-ESM2.1 are the largest among all models, while land carbon uptake from the ACCESS-ESM1.5 is the lowest. Finally, in the RAD simulation (panel f) the loss of carbon from land in response to increasing temperatures is lowest in the MPI-ESM1.2-LR and largest in the BCC-CSM2-MR. Over the ocean, while most models behave very similarly, the carbon uptake in the BCC-CSM2-MR, ACCESS-ESM1.5, and NOAA-GFDL-ESM4 are larger than most models in the COU and BGC simulations. In the RAD simulation, almost all models simulate a loss of carbon from the ocean, but the CNRM-ESM2.1 shows a small uptake.



2048 **Figure A1: Individual model values from CMIP6 models for globally-averaged surface**  
 2049 **temperature change (top row), cumulative atmosphere-land  $\text{CO}_2$  flux (middle row), and**  
 2050 **cumulative atmosphere-ocean  $\text{CO}_2$  flux (bottom row) from the fully-, biogeochemically- and**  
 2051 **radiatively-coupled versions of the 1pctCO2 experiment.**



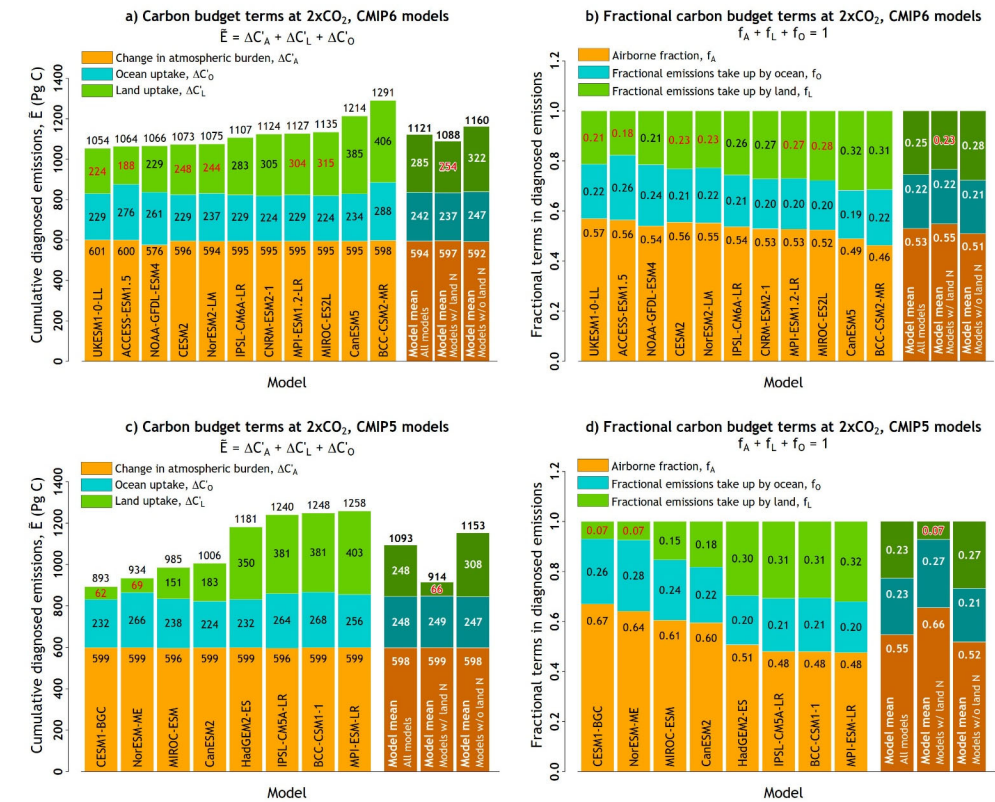


Figure A2: Components of the carbon budget terms in cumulative emissions from the eleven participating CMIP6 models based on equation (A6) in panel (a) and equation (A7) in panel (b) using results from the fully-coupled 1% per year increasing CO<sub>2</sub> simulation at 2xCO<sub>2</sub> (year 70) in contrast to Figure 4 which showed these results at 4xCO<sub>2</sub>. The models are arranged in an ascending order based on their cumulative emissions values. Results from participating CMIP5 models in the A13 study are shown in panels c and d. In addition, ESMs whose land component includes a representation of N cycle are identified by red font colour for cumulative land carbon uptake (panels a and c) and fractional emissions taken up by land (panels b and d). Model mean is shown for all models but also separately for models whose land components include or do not include a representation of the N cycle.

Deleted: 1

Deleted: 15

Deleted: 16

Deleted: but

Deleted: 5

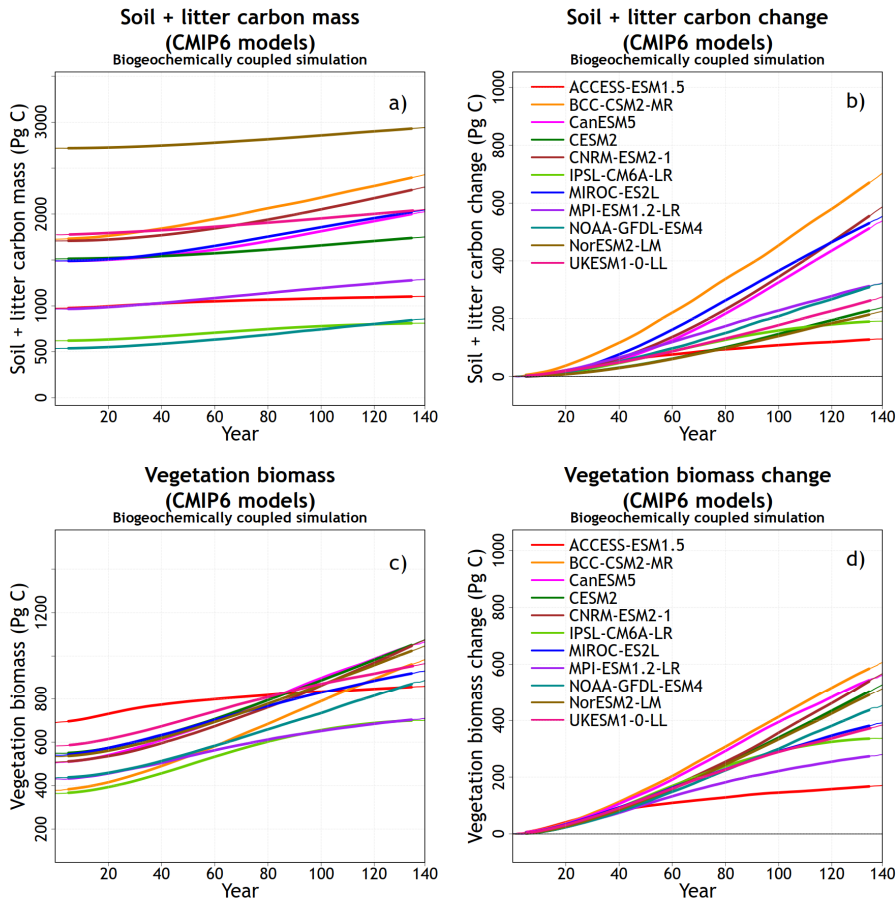


Figure A3: Absolute amounts and the change from the beginning of the BGC simulation for carbon in soil+litter (panels a and b) and vegetation (panels c and d) pools.

Deleted: 2

2076 **A4. Additional tables**

2077 **Table A1:** Values of carbon-concentration and carbon-climate feedback parameters for land and  
2078 ocean calculated using the **BGC-COU** approach (using results from the **BGC and COU** simulations),  
2079 and the linear transient climate sensitivity to CO<sub>2</sub>, from CMIP6 and CMIP5 models at 4×CO<sub>2</sub> (i.e.  
2080 at the end of the 1pctCO2 simulation) and 2×CO<sub>2</sub>.

CMIP6 models at 4×CO <sub>2</sub>					
	Land		Ocean		
	Carbon-climate feedback, $\gamma_L$	Carbon-concentration feedback, $\beta_L$	Carbon-climate feedback, $\gamma_O$	Carbon-concentration feedback, $\beta_O$	Climate sensitivity, $\alpha$
	PgC °C <sup>-1</sup>	PgC ppm <sup>-1</sup>	PgC °C <sup>-1</sup>	PgC ppm <sup>-1</sup>	°C ppm <sup>-1</sup>
ACCESS-ESM1.5	-21.1	0.37	-23.75	0.9	0.00546
BCC-CSM2-MR	-163.1	1.81	-19.94	0.92	0.00485
CanESM5	15.95	1.28	-14.72	0.77	0.00751
CESM2	-21.6	0.9	-10.85	0.71	0.00637
CNRM-ESM2-1	-83.11	1.36	-9.38	0.7	0.00632
IPSL-CM6A-LR	-8.67	0.62	-12.97	0.76	0.00687
MIROC-ES2L	-69.57	1.12	-22.25	0.73	0.00436
MPI-ESM1.2-LR	-5.17	0.71	-20.11	0.77	0.00512
NOAA-GFDL-ESM4	-80.06	0.93	-21.65	0.84	0.00430
NorESM2-LM	-20.95	0.85	-19.64	0.78	0.00410
UKESM1-0-LL	-38.4	0.75	-14.07	0.75	0.00721
Model mean	-45.07	0.97	-17.21	0.78	0.00568
Sample standard deviation	50.59	0.40	4.95	0.07	0.00123

CMIP6 models at 2×CO <sub>2</sub>					
	Land		Ocean		
	Carbon-climate feedback, $\gamma_L$	Carbon-concentration feedback, $\beta_L$	Carbon-climate feedback, $\gamma_O$	Carbon-concentration feedback, $\beta_O$	Climate sensitivity, $\alpha$
		PgC °C <sup>-1</sup>	PgC ppm <sup>-1</sup>	PgC °C <sup>-1</sup>	PgC ppm <sup>-1</sup>
ACCESS-ESM1.5	-12	0.75	-11.72	1.06	0.00750
BCC-CSM2-MR	-132.84	2.22	-12.38	1.09	0.00592
CanESM5	-6.22	1.42	-7.71	0.9	0.00950
CESM2	-12.76	0.98	-4.24	0.84	0.00789
CNRM-ESM2-1	-44.51	1.37	-3.58	0.81	0.00650
IPSL-CM6A-LR	-12.24	1.11	-7.37	0.87	0.00876
MIROC-ES2L	-63.36	1.45	-10.44	0.85	0.00530
MPI-ESM1.2-LR	-0.81	1.08	-11.4	0.88	0.00636
NOAA-GFDL-ESM4	-50.69	1.08	-8.97	0.97	0.00543
NorESM2-LM	-15.61	0.94	-9.34	0.88	0.00509
UKESM1-0-LL	-24.01	1	-7.35	0.88	0.00885
Model mean	-34.10	1.22	-8.59	0.91	0.00701
Sample standard deviation	38.39	0.40	2.80	0.09	0.00157

Deleted: COU and

Deleted: S

Deleted: 48.24

Deleted: 0.38

Deleted: 72

Deleted: 18

Deleted: S

Deleted: 36.61

Deleted: 38

Deleted: 76

Deleted: 0

2094

CMIP5 models at 4xCO <sub>2</sub>					
	Land		Ocean		
	Carbon-climate feedback, $\gamma_L$	Carbon-concentration feedback, $\beta_L$	Carbon-climate feedback, $\gamma_O$	Carbon-concentration feedback, $\beta_O$	Climate sensitivity, $\alpha$
		PgC °C <sup>-1</sup>	PgC ppm <sup>-1</sup>	PgC °C <sup>-1</sup>	PgC ppm <sup>-1</sup>
BCC-CSM1-1	-109.7	1.4	-17.4	0.85	0.00511
CanESM2	-64.9	0.99	-11.28	0.7	0.00623
CESM1-BGC	-6.39	0.24	-12.16	0.74	0.00481
IPSL-CM5A-LR	-46.65	1.13	-17.6	0.89	0.00559
MIROC-ESM	-86.82	0.75	-20.94	0.82	0.00660
MPI-ESM-LR	-89.64	1.49	-18.36	0.85	0.00582
NorESM-ME	-4.3	0.22	-18.72	0.87	0.00441
HadGEM2-ES	-54.94	1.24	-21.88	0.82	0.00607
Model mean	-57.92	0.93	-17.29	0.82	0.00558
Sample standard deviation	38.24	0.49	3.78	0.07	0.00075

- Deleted: S
- Deleted: 5.77
- Deleted: 46
- Deleted: 54
- Deleted: 6
- Deleted: 0

2095

CMIP5 models at 2xCO <sub>2</sub>					
	Land		Ocean		
	Carbon-climate feedback, $\gamma_L$	Carbon-concentration feedback, $\beta_L$	Carbon-climate feedback, $\gamma_O$	Carbon-concentration feedback, $\beta_O$	Climate sensitivity, $\alpha$
		PgC °C <sup>-1</sup>	PgC ppm <sup>-1</sup>	PgC °C <sup>-1</sup>	PgC ppm <sup>-1</sup>
BCC-CSM1-1	-57.61	1.75	-11.06	1.03	0.00676
CanESM2	-48.13	1.05	-6.64	0.85	0.00830
CESM1-BGC	-5.02	0.25	-4.41	0.86	0.00603
IPSL-CM5A-LR	-37.28	1.58	-8.88	0.99	0.00609
MIROC-ESM	-64.79	1.04	-12.36	0.94	0.00778
MPI-ESM-LR	-62.52	1.86	-11.24	0.99	0.00686
NorESM-ME	1.02	0.24	-9.53	1	0.00506
HadGEM2-ES	-21.78	1.43	-11.27	0.92	0.00836
Model mean	-37.01	1.15	-9.42	0.95	0.00690
Sample standard deviation	25.48	0.63	2.70	0.07	0.00118

- Deleted: S
- Deleted: 4.17
- Deleted: 59
- Deleted: 53
- Deleted: 6
- Deleted: 0

2096

2097

2110 **Table A2:** Estimate of the change in the ocean carbon inventory (PgC) expected from a time  
2111 integral of the global air-sea carbon flux into the ocean versus the volume integral of the change  
2112 in the dissolved inorganic carbon, together with the small residual. The time integral of the air-  
2113 sea carbon flux provides the dominant contribution to the change in the ocean carbon inventory,  
2114 although there is a small mismatch due to the land to ocean carbon flux from river runoff and the  
2115 ocean to land carbon flux from carbon burial in ocean sediments.

2116

Model	Time integral of the global air-sea carbon flux into the ocean (PgC)	Global ocean volume integral of $\Delta$ DIC (PgC)	Residual (PgC)
ACCESS-ESM1.5	763	736	27
CanESM5	656	651	5
CNRM-ESM2-1	597	658	-61
MIROC-ES2L	625	632	-7
MPI-ESM1.2-LR	657	621	36
NOAA-GFDL-ESM4	720	759	-39
NorESM2-LM	671	628	43
UKESM1-0-LL	637	609	28
Model mean ( $\bar{x}$ )	666	662	
Sample standard deviation ( $\sigma_x$ )	53	55	
Coefficient of variation ( $\sigma_x/ \bar{x} $ )	0.08	0.08	

2117

2118

2119

Deleted: s

2121

2122 **Table A3:** Carbon-cycle feedback parameters for the ocean,  $\beta_o$  and  $\gamma_o$ , diagnosed from the air-  
2123 sea carbon fluxes and separately diagnosed for the ocean carbon inventory and its separate  
2124 ocean saturated, disequilibrium and regenerated DIC pools for the subset of eight CMIP6 models  
2125 for which 3D ocean data were available; their sum does not exactly match the diagnostics from  
2126 the air-sea fluxes due to land-ocean interactions involving storage in sediments and river inputs.

2127

	Carbon-concentration feedback (PgC ppm <sup>-1</sup> )				Carbon-climate feedback (PgC °C <sup>-1</sup> )			
	$\beta_o$	$\beta_{sat}$	$\beta_{dis}$	$\beta_{reg}$	$\gamma_o$	$\gamma_{sat}$	$\gamma_{dis}$	$\gamma_{reg}$
ACCESS-ESM1.5	0.90	3.54	-2.69	0.005	-23.75	-13.60	-20.47	11.52
CanESM5	0.77	3.83	-3.06	-0.001	-14.72	-10.72	-8.62	4.29
CNRM-ESM2-1	0.70	3.75	-3.01	0.03	-9.38	-14.56	-17.66	29.27
MIROC-ES2L	0.73	3.76	-3.01	-0.001	-22.25	-16.48	-25.50	21.08
MPI-ESM1.2-LR	0.77	3.34	-2.62	0.002	-20.11	-14.37	-15.37	8.40
NorESM2-LM	0.78	3.67	-2.92	-0.004	-19.64	-12.91	-14.44	9.19
UKESM1-0-LL	0.75	3.62	-2.88	-0.02	-14.07	-8.87	-11.04	6.56
NOAA-GFDL-ESM4	0.84	3.77	-2.93	0.05	-21.65	-10.75	-17.77	7.7
Model mean ( $\bar{x}$ )	0.78	3.66	-2.89	-0.003	-18.20	-12.78	-16.36	12.25
Sample standard deviation ( $\sigma_x$ )	0.06	0.16	0.16	0.009	4.95	2.50	5.31	8.53
Coefficient of variation ( $\sigma_x/ \bar{x} $ )	0.08	0.05	0.06	3.00	0.27	0.20	0.33	0.70

Deleted: 16.95

Deleted: s

Deleted: 5.62

Deleted: 33

Moved up [1]: Table A4: Transient Climate Response (TCE,  $\Delta T_{2\times CO_2}$ ), diagnosed cumulative emissions at  $2\times CO_2$  ( $\bar{E}_{2\times CO_2}$ ), and transient climate response to cumulative emissions (TCRE) for the eleven CMIP6 models considered in this study.¶¶

2128

2129

2140 **A5. Model descriptions**

2141 **A5.1. Commonwealth Scientific and Industrial Research Organisation (CSIRO) ACCESS-ESM1.5**

2142 The Australian Community Climate and Earth System Simulator ACCESS-ESM1.5 (Ziehn et al.,  
2143 2020, The Australian Earth System Model: ACCESS-ESM1.5, submitted to Journal of Southern  
2144 Hemisphere Earth Systems Science) is comprised of a number of component models. The  
2145 atmospheric model is the UK Met Office Unified Model at version 7.3 (Martin et al., 2010, 2011)  
2146 with their land surface model replaced with the Community Atmosphere Biosphere Land  
2147 Exchange (CABLE) model (Kowalczyk et al., 2013). The ocean component is the NOAA/GFDL  
2148 Modular Ocean Model (MOM) at version 5 (Griffies, 2014) with the same configuration as the  
2149 ocean model component of ACCESS1.0 and ACCESS1.3 (Bi et al., 2013). Sea ice is simulated using  
2150 the LANL CICE4.1 model (Hunke and Lipscomb, 2010). Coupling of the ocean and sea-ice to the  
2151 atmosphere is through the OASIS-MCT coupler (Valcke, 2013). The physical climate model  
2152 configuration used here is very similar to the version (ACCESS1.3) that contributed to the Coupled  
2153 Model Intercomparison Project Phase 5 (CMIP5) (Bi et al., 2013). The carbon cycle is included in  
2154 ACCESS through the CABLE land surface model and its biogeochemistry module, CASA-CNP  
2155 (Wang et al., 2010), and through the World Ocean Model of Biogeochemistry and Trophic-  
2156 dynamics (WOMBAT) (Oke et al., 2013).

2157

2158 The WOMBAT model is based on a NPZD (nutrient-phosphate, phytoplankton, zooplankton and  
2159 detritus) model with the additions of bio-available iron limitation, dissolved inorganic carbon,  
2160 calcium carbonate, alkalinity and oxygen. Productivity drives uptake and formation of carbon

**Deleted:** (Ziehn et al., 2017)

**Formatted:** Font: (Default) +Body (Calibri), 11 pt, Check spelling and grammar

**Field Code Changed**

2162 and oxygen ~~that are~~ exchanged with the atmosphere. Sinking and remineralization of detritus  
2163 carries biogeochemical tracers to the deep ocean. Iron is supplied by dust deposition, continental  
2164 shelves and background ocean values.

Deleted: which

2165  
2166 The Australian community model CABLE simulates the fluxes of momentum, heat, water and  
2167 carbon at the surface. The biogeochemistry module CASA-CNP simulates the flow of carbon and  
2168 nutrients such as nitrogen and phosphorus between three plant biomass pools (leaf, wood, root),  
2169 three litter pools (metabolic, structural, coarse woody debris) and three organic soil pools  
2170 (microbial, slow, passive) plus one inorganic soil mineral nitrogen pool and three phosphorus soil  
2171 pools.

2172  
2173 In the CABLE configuration applied here ~~the land surface is represented by 10 vegetation~~ and 3  
2174 non-vegetation ~~land cover~~ types. CABLE calculates gross primary production (GPP) and leaf  
2175 respiration at every time step using a two-leaf canopy scheme (Wang and Leuning, 1998) as a  
2176 function of the leaf area index (LAI). This set-up uses a simulated (prognostic) LAI based on the  
2177 size of the leaf carbon pool and the specific leaf area. Daily mean GPP and leaf respiration values  
2178 are then passed onto CASA-CNP to calculate daily respiration fluxes and the flow of carbon and  
2179 nutrients between the pools. Similar to the previous version, ACCESS-ESM1 (Law et al., 2017;  
2180 Ziehn et al., 2017), the model is run with nitrogen and phosphorus limitation enabled.

Deleted: we use

Deleted: ed

Deleted: types

Deleted: ed



2187 **A5.2. Beijing Climate Center (BCC) Climate System Model version 2 with Medium Resolution**  
2188 **(BCC-CSM2-MR)**

2189 BCC-CSM2-MR (Wu et al., 2019) is the second generation of the BCC model with medium  
2190 resolution that was released to run CMIP6 simulations. It is a fully-coupled global climate model  
2191 and updated from its previous version of BCC-CSM1.1 used for CMIP5 (Wu et al., 2013). The  
2192 atmospheric component of BCC-CSM2-MR is the BCC Atmospheric General Circulation Model  
2193 version 3 (BCC-AGCM3-MR, (Wu et al., 2019)). The land component is the BCC Atmosphere and  
2194 Vegetation Interaction Model version 2.0 (BCC-AVIM2, Li et al., 2019) with terrestrial carbon  
2195 cycle. The oceanic component is the Modular Ocean Model version 4 with 40 levels (hereafter  
2196 MOM4-L40). The sea ice component is Sea Ice Simulator (SIS). These components are physically  
2197 coupled through fluxes of momentum, energy, water, and carbon at their interfaces. The  
2198 coupling was realized with the flux coupler version 5 developed by the National Center for  
2199 Atmosphere Research (NCAR).

2200  
  
2201 The atmospheric component of BCC-CSM2-MR has a horizontal resolution of T106 approximately  
2202 1.125° and 46 vertical levels in a hybrid sigma/pressure vertical coordinate system with the top  
2203 level at 1.459 hPa. The ocean component resolution of BCC-CSM2-MR is 1° longitude by 1/3°  
2204 latitude between 30°S and 30°N which increases to 1° latitude at 60°S and 60°N and nominally  
2205 1° polarward with tripolar coordinates, and there are 40 z-levels in the vertical.

2206

Formatted: Font: (Default) Calibri, 12 pt

Field Code Changed

Deleted: (Li et al., 2019)

Formatted: Font: (Default) +Body (Calibri), Check spelling and grammar

Deleted: ranged

2209 The atmospheric component model BCC-AGCM3-MR in BCC-CSM2-MR is developed from its  
2210 previous CMIP5 version (Wu et al., 2008). The main updates include a modification of deep  
2211 convection parameterization, a new scheme for cloud fraction, indirect effects of aerosols  
2212 through clouds and precipitation, and the gravity wave drag generated by deep convection (Wu  
2213 et al., 2019). Atmospheric CO<sub>2</sub> concentration in BCC-AGCM3-MR for this work is a prognostic  
2214 variable and calculated through a budget equation which considered advective transport in the  
2215 atmosphere, anthropogenic CO<sub>2</sub> emissions, and interactive CO<sub>2</sub> fluxes at the interfaces with land  
2216 and ocean. But chemical processes are not taken into account. The terrestrial carbon cycle in  
2217 BCC-AVIM2 (Li et al., 2019) operates through a series of biochemical and physiological processes  
2218 on photosynthesis and respiration of vegetation, and takes into account carbon loss due to  
2219 turnover and mortality of vegetation, and CO<sub>2</sub> release into atmosphere through soil respiration.  
2220 The vegetation litter on the ground surface and in the soil is divided into eight terrestrial carbon  
2221 pools (surface structural, surface metabolic, surface microbial, soil structural, soil metabolic, soil  
2222 microbial, slow, and passive carbon pools) according to the timescale of the decomposition of  
2223 carbon in each pool and the transfers between different pools. Allocation to and from the three  
2224 vegetation biomass pools (leaf, stem, root) leads to dynamic vegetation that in turn produces  
2225 litter fall and which ultimately transfers carbon to soil organic matter. The allocation of carbon  
2226 to the three vegetation biomass pools is dependent on light availability, water stress and  
2227 phenology stages of the canopy and follows the formulations of Arora and Boer (2005).  
2228

2229 The biogeochemistry module to simulate the ocean carbon cycle in MOM4\_L40 is based on the  
2230 protocols from the Ocean Carbon Cycle Model Intercomparison Project–Phase 2 (OCMIP2,

Deleted: (Li et al., 2019)

Field Code Changed

Formatted: Font: (Default) +Body (Calibri), Check spelling and grammar

Formatted: Font: (Default) Calibri, 12 pt

Deleted: to

Deleted: to

Deleted: carbon

Deleted: (

Deleted: ,

2237 <http://www.ipsl.jussieu.fr/OCMIP/phase2/>). The OCMIP biogeochemistry module parameterizes  
2238 the process of marine biology in terms of geochemical fluxes without explicit representation of  
2239 the marine ecosystem and food web processes, and includes five prognostic variables:  
2240 phosphate, dissolved organic phosphorus, dissolved oxygen, dissolved inorganic carbon, and  
2241 alkalinity. Ocean carbon cycle processes in BCC-CSM2-MR follow OCMIP, except for  
2242 parameterizing the export of organic matter from surface waters to deep oceans (Wu et al.,  
2243 2013).

2244

### 2245 **A5.3. Canadian Centre for Climate Modelling and Analysis (CCCma) fifth generation Earth** 2246 **System Model, CanESM5**

2247 CanESM5 has evolved from its predecessor CanESM2 (Arora et al., 2011) that was used in the  
2248 Coupled Model Intercomparison Project phase 5 (CMIP5). CanESM5 represents a major update  
2249 to CanESM2 and described in detail in [Swart et al. \(2019\)](#). The major changes relative to CanESM2  
2250 are the implementation of completely new models for the ocean, sea-ice, marine ecosystems,  
2251 and a new coupler. The resolution of CanESM5 (T63 or ~2.8° in the atmosphere and ~1° in the  
2252 ocean) remains similar to CanESM2, and is at the lower end of the spectrum of CMIP6 models.  
2253 The atmospheric component of CanESM5 is represented by version 5 of the Canadian  
2254 Atmospheric Model (CanAM5) has several improvements relative to its predecessor, CanAM4  
2255 (von Salzen et al., 2013), including changes to aerosol, clouds, radiation, land surface and lake  
2256 processes. CanAM5 uses a triangular spectral truncation in the model dynamical core, with an  
2257 approximate horizontal resolution of 2.8 degrees in latitude/longitude. It uses a hybrid vertical

**Formatted:** Font: (Default) Calibri, 12 pt, Do not check spelling or grammar

**Formatted:** Font: (Default) Calibri, 12 pt, Do not check spelling or grammar

2258 coordinate system with 49 levels between the surface and 1 hPa, with a vertical resolution of  
2259 about 100 m near the surface. Relative to the 35 levels used in CanESM2 most of the additional  
2260 14 levels were added in the upper troposphere and stratosphere.

2261

2262 The land surface in CanESM5 is modelled using the Canadian Land Surface Scheme (CLASS;  
2263 (Verseghy, 2000)) and the Canadian Terrestrial Ecosystem Model (CTEM; (Arora and Boer, 2005,  
2264 2010)) which together form the land component of CanESM5. CLASS-CTEM simulate the physical  
2265 and biogeochemical land surface processes, respectively, and together they calculate fluxes of  
2266 energy, water, CO<sub>2</sub> and wetland CH<sub>4</sub> emissions at the land-atmosphere boundary. Over land,  
2267 three permeable soil layers are used with default thicknesses of 0.1, 0.25, and 3.75 m for which  
2268 liquid and frozen soil moistures and temperature are prognostically calculated. The depth to  
2269 bedrock is specified on the basis of the global data set which reduces thicknesses of the  
2270 permeable soil layers where soil depth is less than 4.1 meters. Snow is represented using one  
2271 layer whose snow water equivalent and temperature are modelled prognostically. The  
2272 introduction of dynamic wetlands and their methane emissions is a new biogeochemical process  
2273 added since the CanESM2 (Arora et al., 2018). Nitrogen cycle over land is not represented but

2274 the a parameterization of photosynthesis down-regulation as CO<sub>2</sub> increases is included. The  
2275 magnitude of the parameter representing this down-regulation is increased in CanESM5,  
2276 compared to CanESM2, following (Arora and Scinocca, 2016) who found best value of this  
2277 parameter that reproduced various aspects of the historical carbon budget for CanESM4.2 (a  
2278 model version more similar to CanESM2 than CanESM5). Other than wetlands, and the changes

Field Code Changed

Deleted: effect of

Deleted: represented

2281 to the strength of the CO<sub>2</sub> fertilization effect, the remaining terrestrial ecosystem processes are  
2282 represented the same as in CanESM2.

2283

2284 The physical ocean component of CanESM5 is based on NEMO version 3.4.1. It is configured on  
2285 the tripolar ORCA1 C-grid with 45 z-coordinate vertical levels, varying in thickness from ~6 m near  
2286 the surface to ~250 m in the abyssal ocean. The horizontal resolution is based on a 1° Mercator  
2287 grid, varying with the cosine of latitude, with a refinement of the meridional grid spacing to 1/3°  
2288 near the equator. Two modifications have been introduced to the NEMO's mesoscale and small-  
2289 scale mixing physics in CanESM5 and these are detailed in Swart et al. (2019). Sea ice is  
2290 represented using the LIM2 sea ice model (Fichefet and Morales Maqueda, 1997; Bouillon et al.,  
2291 2009), which is run within the NEMO framework.

2292

2293 Ocean carbon cycle is represented using the Canadian Model of Ocean Carbon (CMOC) which  
2294 was developed for earlier versions of CanESM (Christian et al., 2010; Arora et al., 2011), and  
2295 includes carbon chemistry and biology. The biological component is a simple Nutrient-  
2296 Phytoplankton-Zooplankton-Detritus (NPZD) model, with fixed Redfield stoichiometry, and  
2297 simple parameterizations of iron limitation, nitrogen fixation, and export flux of calcium  
2298 carbonate.

2299

2300 **A5.4. Community Earth System Model, version 2 (CESM2)**

Deleted: (

Deleted: .,

2303 The CESM2 (Danabasoglu et al., 2019: The Community Earth System Model version 2 - CESM2,  
2304 in preparation) contains substantial improvements since CESM1. The resolution remains the  
2305 same as in CESM1 (0.9° latitude x 1.25° longitude for the atmosphere and land with 32 vertical  
2306 atmospheric levels and 25 ground levels and ~1° for the ocean). The Community Atmosphere  
2307 Model version 6 (Neale, R. B. et al., 2019: The NCAR Community Atmosphere Model version 6  
2308 (CAM6): Scientific configuration and simulation fidelity, in preparation) includes many changes  
2309 to the representation of physical processes with the primary change being the inclusion of the  
2310 Cloud Layers Unified By Binormals (CLUBB) unified turbulence scheme.

2311

2312 The CESM2 ocean component (POP2) is largely the same as that used in CESM1 except with a  
2313 new parameterization for mixing effects in estuaries along with several other numerical and  
2314 physics improvements. The sea ice model is CICE version 5.1.2 (CICE5) (Hunke et al., 2015).

Deleted: ;

2315 Ocean biogeochemistry is represented by the Marine Biogeochemistry Library (MARBL). MARBL  
2316 represents multiple nutrient co-limitation (N, P, Si, and Fe). It includes three explicit  
2317 phytoplankton functional groups (diatoms, diazotrophs, and pico/nano phytoplankton), one  
2318 implicit phytoplankton group (calcifiers) and one zooplankton group. MARBL includes prognostic  
2319 carbonate chemistry and simulates sinking particulate organic matter. Major updates relative to  
2320 CESM1 include a representation of subgrid-scale variations in light and variable C:P  
2321 stoichiometry. Atmospheric deposition of iron is computed prognostically in CESM2 as a function  
2322 of dust and black carbon deposition simulated by CAM6. Riverine nutrient, carbon, and alkalinity  
2323 fluxes are supplied to the ocean from a dataset.

2325

2326 The land component is the Community Land Model version 5 (CLM5, [Lawrence et al., 2019](#)) which  
2327 simulates land water, energy, momentum, carbon and nitrogen cycling. CLM5 includes an  
2328 extensive suite of new and updated processes and parameterizations that collectively improve  
2329 the model's hydrological, biogeochemical and ecological realism and enhance the representation  
2330 of anthropogenic land use activities on climate and the carbon cycle. The primary updates are as  
2331 follows with details, references, and additional updates described and listed in [Lawrence et al.](#)  
2332 [\(2019\)](#); (1) updated parameterizations and structure for hydrology and snow (spatially explicit  
2333 soil depth, dry surface layer, revised groundwater scheme, revised canopy interception and  
2334 canopy snow processes, updated fresh snow density, and inclusion of the Model for Scale  
2335 Adaptive River Transport); (2) a plant hydraulics scheme to more mechanistically represent plant  
2336 water use and limitation; (3) vertically-resolved soil biogeochemistry with base organic matter  
2337 decomposition rates varying with depth and modified by soil temperature, water, and oxygen  
2338 limitation and nitrification and denitrification updated as in Century model; (4) a methane  
2339 production, oxidation, and emissions model; (5) improved representation of plant N dynamics to  
2340 address deficiencies in CLM4 through introduction of flexible plant carbon : nitrogen (C:N)  
2341 stoichiometry which avoids the problematic CLM4 separation of potential and actual plant  
2342 productivity, explicitly simulating photosynthetic capacity response to environmental conditions  
2343 through the Leaf Utilization of Nitrogen for Assimilation (LUNA) module, and accounting for how  
2344 N availability affects plant productivity through the Fixation and Uptake of Nitrogen (FUN)  
2345 module which determines the C costs of N acquisition; methane emissions and oxidation from  
2346 natural land processes; (6) a global active crop model with six crop types and time-evolving

**Formatted:** Font: (Default) Calibri, 12 pt

**Deleted:** (Lawrence et al., 2018)

**Formatted:** Font: (Default) +Body (Calibri), 11 pt, Check spelling and grammar

**Field Code Changed**

**Field Code Changed**

**Formatted:** Font: (Default) Calibri, 12 pt

**Deleted:** (Lawrence et al., 2018)

**Formatted:** Font: (Default) Calibri, 12 pt

**Formatted:** Font: (Default) +Body (Calibri), 11 pt, Check spelling and grammar

2349 irrigated areas and industrial fertilization rates; (7) updated canopy processes including a revised  
2350 canopy radiation scheme and canopy scaling of leaf processes, co-limitations on photosynthesis  
2351 and updated stomatal conductance; (8) a new fire model that includes representation of natural  
2352 and anthropogenic ignition sources and suppression along with agricultural, deforestation, and  
2353 peat fires; and (9) inclusion of carbon isotopes.

2354

#### 2355 **A5.5. Centre National de Recherches Météorologiques (CNRM) CNRM-ESM2-1**

2356 CNRM-ESM2-1 is the second generation Earth System model developed by CNRM-CERFACS for  
2357 CMIP6 (Séférian et al., 2019).

2358

2359 The atmosphere component of CNRM-ESM2-1 is based on version 6.3 of the global spectral  
2360 model ARPEGE-Climat (ARPEGE-Climat\_v6.3). ARPEGE-Climat resolves atmospheric dynamics  
2361 and thermodynamics on a T127 triangular grid truncation that offers a spatial resolution of about  
2362 150 km in both longitude and latitude. CNRM-ESM2-1 employs a “high-top” configuration with  
2363 91 vertical levels that extend from the surface to 0.01 hPa in the mesosphere; 15 hybrid  $\sigma$ -  
2364 pressure levels are available below 1500 m.

2365

2366 The surface state variables and fluxes at the surface-atmosphere interface are simulated by the  
2367 SURFEX modeling platform version 8.0 over the same grid and with the same time-step as the  
2368 atmosphere model. SURFEX\_v8.0 encompasses several submodules for modeling the interactions

Formatted: Font: 12 pt



2369 between the atmosphere, the ocean, the lakes and the land surface. Over the land surface,  
2370 CNRM-ESM2-1 uses the ISBA-CTRIP land surface modeling system ([http://www.umr-](http://www.umr-cnrm.fr/spip.php?article1092&lang=en)  
2371 [cnrm.fr/spip.php?article1092&lang=en](http://www.umr-cnrm.fr/spip.php?article1092&lang=en)) to solve energy, carbon and water budgets at the land  
2372 surface (Decharme et al., 2019; Delire et al., 2019). Its physical core explicitly solves the one-  
2373 dimensional Fourier and Darcy laws throughout the soil, accounting for the hydraulic and thermal  
2374 properties of soil organic carbon. It uses a 12-layer snow model of intermediate complexity that  
2375 allows separate water and energy budgets for the soil and the snowpack. It accounts for a  
2376 dynamic river flooding scheme in which floodplains interact with the soil and the atmosphere  
2377 through free-water evaporation, infiltration and precipitation interception and a two-  
2378 dimensional diffusive groundwater scheme to represent unconfined aquifers and upward  
2379 capillarity fluxes into the superficial soil. More details on these physical aspects can be found in  
2380 (Decharme et al., 2019).

2381

2382 To simulate the land carbon cycle and vegetation-climate interactions, ISBA-CTRIP simulates  
2383 plant physiology, carbon allocation and turnover, and carbon cycling through vegetation, litter,  
2384 and soil. It includes a module for wild fires, land use and land cover changes, and carbon leaching  
2385 through the soil and transport of dissolved organic carbon to the ocean. Leaf photosynthesis is  
2386 represented by the semi-empirical model proposed by (Goudriaan et al., 1985). Canopy level  
2387 assimilation is calculated using a 10-layer radiative transfer scheme including direct and diffuse  
2388 radiation. Vegetation in ISBA is represented by 4 carbon pools for grasses and crops (leaves, stem,  
2389 roots and a non-structural carbohydrate storage pool) with 2 additional pools for trees  
2390 (aboveground wood and coarse roots). Leaf phenology results directly from the carbon balance

2391 of the leaves. The model distinguishes 16 vegetation types (10 tree and shrub types, 3 grass types  
2392 and 3 crop types) alongside desert, rocks and permanent snow. In the absence of nitrogen cycling  
2393 within the vegetation, an implicit nitrogen limitation scheme that reduces specific leaf area with  
2394 increasing CO<sub>2</sub> concentration was implemented in ISBA following the meta-analysis of Yin (2002).

Deleted: (

Deleted: ,

2395 Additionally, there is an ad-hoc representation of photosynthesis down-regulation. The litter and  
2396 soil organic matter module is based on the soil carbon part of the CENTURY model (Parton et al.,  
2397 1988). The 4 litter and 3 soil carbon pools are defined based on their location above- or below-  
2398 ground and potential decomposition rates. The litter pools are supplied by the flux of dead  
2399 biomass from each biomass reservoir (turnover). Decomposition of litter and soil carbon releases  
2400 CO<sub>2</sub> (heterotrophic respiration). During the decomposition process, some carbon is dissolved by  
2401 water slowly percolating through the soil column. This dissolved organic carbon is transported by  
2402 the rivers to the ocean. A detailed description of the terrestrial carbon cycle can be found in  
2403 Delire et al. (2019).

Deleted: (

Deleted: .,

2405 The ocean component of CNRM-ESM2-1 is the Nucleus for European Models of the Ocean  
2406 (NEMO) version 3.6 (Madec et al., 2017) which is coupled to both the Global Experimental Leads  
2407 and ice for ATmosphere and Ocean (GELATO) sea-ice model (Salas Mélia, 2002) version 6 and  
2408 also the marine biogeochemical model Pelagic Interaction Scheme for Carbon and Ecosystem  
2409 Studies version 2-gas (PISCESv2-gas). NEMOv3.6 operates on the ORCA1L75 grid (Mathiot et al.,  
2410 2017) which offers a nominal resolution of 1° to which a latitudinal grid refinement of 1/3° is  
2411 added in the tropics; this grid describes 75 ocean vertical layers using a vertical z\*-coordinate  
2412 with partial step bathymetry formulation (Bernard et al., 2006).

Deleted: e

2418

2419 The atmospheric chemistry scheme of CNRM-ESM2-1 is Reactive Processes Ruling the Ozone  
2420 Budget in the Stratosphere version 2 (REPROBUS-C\_v2). This scheme resolves the spatial  
2421 distribution of 63 chemistry species but does not represent the low troposphere ozone non-  
2422 methane hydrocarbon chemistry. CNRM-ESM2-1 also includes an interactive tropospheric  
2423 aerosol scheme included in the atmospheric component ARPEGE-Climat. This aerosol scheme,  
2424 named Tropospheric Aerosols for ClimaTe In CNRM (TACTIC\_v2), represents the main  
2425 anthropogenic and natural aerosol species of the troposphere.

2426

2427 The ocean biogeochemical component of CNRM-ESM2-1 uses the Pelagic Interaction Scheme for  
2428 Carbon and Ecosystem Studies model volume 2 version trace gases (PISCESv2-gas), which derives  
2429 from PISCESv2 as described in Aumont et al. (2015). PISCESv2-gas simulates the distribution of  
2430 five nutrients (from macronutrients: nitrate, ammonium, phosphate, and silicate to  
2431 micronutrient: iron) which regulate the growth of two explicit phytoplankton classes  
2432 (nanophytoplankton and diatoms). Dissolved inorganic carbon (DIC) and alkalinity (Alk) are  
2433 involved in the computation of the carbonate chemistry, which is resolved by “Model the Ocean  
2434 Carbonate SYstem” version 2 (MOCSY 2.0, Orr & Epitalon, 2015) in PISCESv2-gas. MOCSY 2.0  
2435 enables a better and faster resolution of the ocean carbonate chemistry at thermodynamic  
2436 equilibria. Oxygen is prognostically simulated using two different oxygen-to-carbon ratios, one  
2437 when ammonium is converted to or mineralized from organic matter, the other when oxygen is  
2438 consumed during nitrification. Their values have been set respectively to 131/122 and 32/122.

Deleted: (

Deleted: .,

2441

2442 At ocean surface, PISCESv2-gas exchanges carbon, oxygen, dimethylsulfide (DMS) and nitrous  
2443 oxide (N<sub>2</sub>O) tracers with the atmosphere using the revised air-sea exchange bulk as published by  
2444 (Wanninkhof, 2014). PISCESv2-gas uses several boundary conditions which represent the supply  
2445 of nutrients from five different sources: atmospheric deposition, rivers, sediment mobilization,  
2446 sea-ice and hydrothermal vents.

2447

#### 2448 **A5.6. Institut Pierre Simon Laplace (IPSL) IPSL-CM6A-LR**

2449 IPSL-CM6A-LR is the coupled climate model of the Institut Pierre Simon Laplace (Servonnat et al.,  
2450 2019, in preparation). It results from the integration of the following components: the LMDZ  
2451 atmospheric general circulation model (version 6A-LR, Hourdin et al., 2019), the NEMO oceanic  
2452 model (version 3.6, (Vancoppenolle et al., 2009; Aumont et al., 2015; Rousset et al., 2015; Madec  
2453 et al., 2017)) and the ORCHIDEE land surface model (version 2.0, Peylin et al., 2019, in  
2454 preparation).

2455

2456 The atmospheric general circulation model LMDZ6A-LR builds onto its previous version that has  
2457 notably incorporated advances in the parameterization of turbulence, convection, and clouds.  
2458 More specifically, LMDZ6A-LR includes a turbulent scheme based on the prognostic equation for  
2459 the turbulent kinetic energy that follows Yamada (1983), a mass flux representation of the  
2460 organized structures of the convective boundary layer called "Thermal Plume Model" (Hourdin

Deleted: (

Deleted: )

Deleted: (

Deleted: ,

et al., 2002; Rio and Hourdin, 2008; Rio et al., 2010), and a parameterization of the cold pools or wakes created below cumulonimbus by the evaporation of convective rainfall (Grandpeix and Lafore, 2010; Grandpeix et al., 2010). It is based on a regular horizontal grid with 144 grid points regularly spaced in longitude and 142 in latitude, corresponding to a resolution of  $2.5^{\circ} \times 1.3^{\circ}$ , and 79 vertical layers.

2470

IPSL-CM6A-LR further includes NEMO (Nucleus for European Models of the Ocean), which is itself composed of three major building blocks: the ocean physics NEMO-OPA (Madec et al., 2017), the sea-ice dynamics and thermodynamics NEMO-LIM3 (Vancoppenolle et al., 2009; Rousset et al., 2015), and the ocean biogeochemistry NEMO-PISCES (Aumont et al., 2015). The grid used has a nominal resolution of  $1^{\circ}$  in the zonal and meridional directions with a latitudinal grid refinement of  $1/3^{\circ}$  in the Tropics. Vertical discretization uses a partial step formulation (Bernard et al., 2006), which ensures a better representation of bottom bathymetry, with 75 levels. The initial layer thicknesses increase non-uniformly from 1 m at the surface to 10 m at 100 m depth, and reaches 200 m at the bottom, and are subsequently time-dependent. NEMO-PISCES (Aumont et al., 2015) models the lower trophic levels of marine ecosystem (phytoplankton, microzooplankton and mesozooplankton) and the biogeochemical cycles of carbon and of the main nutrients (P, N, Fe, and Si). This model also computes air-sea carbon fluxes.

2483

Finally, IPSL-CM6A-LR includes ORCHIDEE, a global process-based terrestrial biosphere model (Krinner et al., 2005; Peylin et al., 2019, in preparation) that calculates carbon, water and energy

Deleted: )

2487 fluxes between the land surface and the atmosphere. Photosynthesis and all components of the  
2488 surface energy and water budgets are calculated at a 15 minute resolution while the dynamics of  
2489 the carbon storage (including carbon allocation in plant reservoirs, soil carbon dynamics, and  
2490 litter decomposition) are resolved on a daily basis. Photosynthesis depends on light availability  
2491 and CO<sub>2</sub> concentration, soil moisture and temperature and is parameterized based on (Farquhar  
2492 et al., 1980) and (Collatz et al., 1992) for C<sub>3</sub> and C<sub>4</sub> plants, respectively. In the absence of an  
2493 explicit representation of the nitrogen cycle, this latest version of ORCHIDEE includes a  
2494 downregulation capability that models a reduction of the terrestrial photosynthesis rates as a  
2495 function of CO<sub>2</sub> concentration. While the N and C cycles interact in multiple ways, a key aspect of  
2496 these interactions is the limitation of carbon uptake by nitrogen availability, especially under  
2497 increasing atmospheric CO<sub>2</sub> concentrations. The downregulation parameterization models a  
2498 reduction of the maximum photosynthetic rate as the atmospheric CO<sub>2</sub> concentrations increases  
2499 using a logarithmic function of the CO<sub>2</sub> concentration relative to 380 ppm (Sellers et al., 1996).  
2500 The PFT-dependent parameters of this parameterization are chosen to broadly reproduce the  
2501 change in GPP observed at the free air enrichment experiment (FACE) sites (Norby and Zak, 2011).  
2502 In ORCHIDEE, the spatial distribution of vegetation is represented using 15 plant functional types  
2503 (PFTs) (Prentice et al., 1992; Cramer, 1997; Wullschleger et al., 2014). More precisely these PFTs  
2504 are decomposed into 3 groups according to their physiological behavior under similar climate  
2505 conditions: tall vegetation (forests) is represented by 8 PFTs, short vegetation (grasses and crops)  
2506 is represented by 6 PFTs, and bare soil. The fractional coverage of these PFTs vary geographically.  
2507 A soil type is associated with each one of these 3 PFT groups. This 3-group partitioning allows for  
2508 dividing each grid box into 3 tiles for which an independent hydrological budget is calculated,

2509 using the 11-layer physically based hydrology scheme. In ORCHIDEE the wood harvest product  
2510 from the LUHv2h database is used in addition to the annual land cover maps.

2511

2512 **A5.7. Team MIROC (Japan Agency for Marine-Earth Science and Technology / the University of**  
2513 **Tokyo / the National Institute for Environmental Studies) MIROC-ES2L**

2514

2515 MIROC-ES2L (Hajima et al., 2020) is based on the global climate model MIROC5.2 (Tatebe et al.,  
2516 2018), which is a minor updated version of MIROC5 used for CMIP5 (Watanabe et al., 2010). The  
2517 physical core shares almost same structure and characteristics with the latest model MIROC6  
2518 (Tatebe et al., 2019), except for the atmospheric spatial resolution and treatment of cumulus  
2519 clouds. This model interactively couples an atmospheric general circulation model (CCSR-NIES  
2520 AGCM, Tatebe et al., 2019) including an on-line aerosol component (SPRINTARS, (Takemura et  
2521 al., 2000)), an ocean GCM with sea-ice component (COCO, (Hasumi, 2015)), and a land physical  
2522 surface model (MATSIRO, (Takata et al., 2003)). The land and ocean biogeochemical components  
2523 are represented by VISIT (Ito and Inatomi, 2012) and OECO2 (Hajima et al., 2020), respectively,  
2524 which are interactively coupled to the atmospheric component. There exists another branched  
2525 version that has atmospheric chemistry component with finer atmospheric grid (MIROC-ES2H),  
2526 but not used in this study.

2527

**Formatted:** Font: (Default) Calibri, 12 pt

**Deleted:** (Hajima et al., 2019b)

**Formatted:** Font: (Default) +Body (Calibri), Check spelling and grammar

**Field Code Changed**

**Field Code Changed**

**Deleted:** (

**Deleted:** )

**Field Code Changed**

**Deleted:**

**Formatted:** Font: (Default) Calibri, 12 pt

**Deleted:** (Hajima et al., 2019b)(Hajima et al., 2019a)(Hajima et al., 2019a)(Hajima et al., 2019a)(T. Hajima, Abe, et al., 2019)(T. Hajima, Abe, et al., 2019)(T. Hajima, Abe, et al., 2019)(T. Hajima, Abe, et al., 2019)(T. Hajima, Abe, et al., 2019)

2536 The atmospheric grid resolution is approximately  $2.81^{\circ}$  with 40 vertical levels between the  
2537 surface and about 3 hPa. For the ocean, the model employs tripolar coordinate system with 62  
2538 vertical levels. To the south of  $63^{\circ}\text{N}$ , the ocean model has longitudinal grid spacing of about  $1^{\circ}$ ,  
2539 while the meridional grid spacing varies from about  $0.5^{\circ}$  near the equator to  $1^{\circ}$  in the mid-  
2540 latitudes. Over the Arctic ocean the grid resolution is even finer following the tripolar coordinate  
2541 system. The physical terrestrial component resolves vertical soil profile with 6 layers down to  
2542 14m depth, with two types of land-use tiles (agriculture and non-agriculture). Terrestrial  
2543 biogeochemical component considers two layered soil organic matter (the upper litter layer and  
2544 the lower humus layer), with 5 types of land-use tiles (primary vegetation, secondary vegetation,  
2545 urban, crop, and pasture).

2546

2547 The terrestrial biogeochemical component covers major processes relevant to global carbon  
2548 cycle, with vegetation (leaf, stem, and root), litter (leaf, stem, and root), and humus (active,  
2549 intermediate, and passive) pools and with a static biome distribution. Details on carbon cycle  
2550 processes in the model can be found in (Ito and Oikawa, 2002). N cycle is simulated with N  
2551 pools of vegetation (canopy and structural), organic soil (litter, humus, and microbe), and  
2552 inorganic nitrogen (ammonium and nitrate). The model considers two major nitrogen influxes  
2553 into ecosystem (biological nitrogen fixation and external nitrogen inputs). Fluxes out of land  
2554 ecosystem in the model are  $\text{N}_2/\text{N}_2\text{O}$  emissions, leaching,  $\text{NH}_3$  emission, and other emission like  
2555 volatilization from land-use product pools. For installing into MIROC-ES2L, the terrestrial  
2556 ecosystem processes were modified such that photosynthetic capacity is controlled by leaf N



2557 concentration. Processes associated with land-use change are also modified to take full  
2558 advantage of CMIP6 LUC forcing dataset. Further details can be found in [\(Hajima et al., 2020\)](#).

**Formatted:** Font: (Default) Calibri, 12 pt

**Field Code Changed**

**Deleted:** (Hajima et al., 2019b)

**Formatted:** Font: (Default) +Body (Calibri), 11 pt, Check spelling and grammar

2560 The new ocean biogeochemical component model, OECO2, is a NPZD-type model and modified  
2561 from the previous model [\(Watanabe et al., 2011\)](#). The biogeochemical compartments of OECO2  
2562 are nitrate, phosphate, dissolved iron, dissolved oxygen, two types of phytoplankton (non-  
2563 diazotroph and diazotroph), zooplankton, and particulate detritus. There exist other  
2564 compartments of dissolved inorganic carbon (DIC), total alkalinity, calcium, calcium carbonate,  
2565 and N<sub>2</sub>O. All organic materials have identical elemental stoichiometric ratio. The model considers  
2566 external nutrient inputs (atmospheric N/Fe deposition, inorganic N/P from rivers, biological N  
2567 fixation, Fe input from ocean bottom/shelf) and nutrient loss (denitrification for N and loss into  
2568 sediment for N, P, and Fe). The emission, transportation and deposition processes of iron are  
2569 explicitly simulated by the atmospheric aerosol component.

**Field Code Changed**

2570

#### 2571 **A5.8. Max Planck Institute for Meteorology (MPI) MPI-ESM1.2-LR**

2572 The MPI-ESM1.2-LR model (Mauritsen et al., 2019) consists of ocean, atmosphere, land and sea-  
2573 ice components which are connected via a coupler analogous to the predecessor MPI-ESM  
2574 versions (Giorgetta et al., 2013). The atmosphere model, ECHAM6.3, at the LR resolution has a  
2575 spectral truncation at T63 or approximately 200-km grid spacing with 47 vertical levels. It is  
2576 directly coupled to the land model, JSBACH3.2, through surface exchange of mass, momentum,  
2577 and heat. The ocean general circulation model, MPIOM1.6 in MPI-ESM1.2-LR runs on a bi-polar

**Deleted:**

2580 grid GR1.5 and has 40 unevenly placed levels. It computes transport of tracers of the ocean  
2581 biogeochemistry model HAMOCC6 (Ilyina et al., 2013; Paulsen et al., 2017). The MPI-ESM-LR  
2582 configuration computes 45–85 model years per physical day enabling new simulations which  
2583 were not feasible previously, such as for instance, large ensemble simulations (Maher et al.,  
2584 2019) or millennial-scale simulations with interactive carbon cycle (Brovkin et al., 2019).

2585

2586 Terrestrial vegetation in JSBACH includes vegetation dynamics which interacts with land use  
2587 changes (Reick et al., 2013), accounting for the latest changes in the land use harmonization  
2588 dataset by (Hurtt et al., 2006). The new SPITFIRE model simulates burned area and carbon  
2589 emissions to atmosphere due to wildfires and anthropogenic fires (Lasslop et al., 2014), replacing  
2590 old global fire parameterization used in the CMIP5 model. Soil carbon model YASSO simulates  
2591 dynamics of 4 fast soil carbon pools which are different for leaf and woody litter types, plus a  
2592 slow humus pool (Goll et al., 2015). Nitrogen and carbon pools are coupled based on CO<sub>2</sub>-induced  
2593 nitrogen limitation (Goll et al., 2017).

2594

2595 The ocean biogeochemistry model HAMOCC6 has been extended as compared to the previous  
2596 version described in Ilyina et al. (2013) to explicitly resolve nitrogen-fixing cyanobacteria as an  
2597 additional prognostic phytoplankton class (Paulsen et al., 2017). This allows to capture the  
2598 response of N<sub>2</sub> fixation and ocean biogeochemistry to changing climate conditions. Additionally,  
2599 updates of existing processes have been performed. This includes for instance the addition of a  
2600 vertically varying settling rate for detritus following the formulation by Martin et al. (1987).

Deleted: (

Deleted: .,

Deleted: (

Deleted: .,

2605 Finally some empirical relationships in the parameterized processes have been updated to follow  
2606 recommendations of the C4MIP and OMIP protocols (Jones et al., 2016; Orr et al., 2017). The full  
2607 overview of changes in HAMOCC is given in (Mauritsen et al., 2019).

Field Code Changed

2609 **A5.9. Geophysical Fluid Dynamics Laboratory (GFDL) NOAA-GFDL-ESM4**

2610  
2611 GFDL-ESM4.1 is a comprehensive, fully-coupled Earth System Model developed by NOAA's  
2612 Geophysical Dynamics Laboratory with a fully-interactive carbon cycle and interactive  
2613 atmospheric chemistry (Dunne et al., ~~2020; The GFDL Earth System Model version 4.1 (GFDL-~~  
2614 ~~ESM4.1): Model description and simulation characteristics, in review, J. Adv. Mod. Earth Sys.)~~  
2615 that builds on previous generation modeling efforts of the carbon cycle (ESM2-series) (Dunne et  
2616 al., 2012, 2013) and atmospheric chemistry (CM3) (Donner et al., 2011) along with increased  
2617 resolution and improved numerics and physics akin to GFDL's 4th generation coupled climate  
2618 model (CM4.0; ~~Held et al., 2019~~), and representation of additional Earth system processes.

Deleted: 2019

Deleted: ,

Deleted: in prep.,

Deleted: The GFDL Earth System Model version 4.1 (GFDL-ESM4.1): Model description and simulation characteristics

Field Code Changed

Deleted: Held et al., 2019, in preparation

Formatted: Font: (Default) Calibri, 12 pt

Deleted: S

Deleted: P

2620 The atmospheric component, GFDL AM4.1, is based on the third generation finite volume cube-  
2621 sphere dynamical core (FV3) (Lin, 2004) with a 1° horizontal resolution and 49 vertical levels. The  
2622 model top is located at ~0.1 hPa to resolve the stratosphere. AM4.1 shares the critical  
2623 developments in model physics with the AM4.0 model (Zhao et al., 2018) including radiation,  
2624 convection, and clouds. AM4.1 differs from the AM4.0 model in its enhanced vertical resolution

2633 and its more explicit representation of atmospheric chemistry that motivated a separate  
2634 radiative and gravity wave tuning.

2635

2636 AM4.1 includes interactive tropospheric and stratospheric gas-phase and aerosol chemistry  
2637 represented through 56 prognostic (transported) tracers and 36 diagnostic (non-transported)  
2638 chemical tracers. The tropospheric chemistry includes reactions for the oxidation of methane  
2639 among other volatile organic compounds. The stratospheric chemistry accounts for the major  
2640 ozone loss cycles and heterogeneous reactions on liquid and solid stratospheric aerosols. Details  
2641 on the base chemical mechanism including improvements relative to the previous generation  
2642 model (AM3) are included in Horowitz et al. (2019, The GFDL Global Atmospheric Chemistry-  
2643 Climate Model AM4.1: Model Description and Simulation Characteristics, [in review, J. Adv. Mod.](#)  
2644 [Earth Sys.](#)).

Deleted: in prep.

2645

2646 Land hydrology and ecosystem dynamics are represented by the GFDL Land Model version 4.1  
2647 (LM4p1; Shevliakova et al., 2019, The land component LM4.1 of the GFDL Earth system model  
2648 ESM4.1: biophysical and biogeochemical processes and interactions with climate, [in review, J.](#)  
2649 [Adv. Mod. Earth Sys.](#)) and builds on the previous generation LM3.1 model (Milly et al., 2014). Soil  
2650 carbon dynamics and biogeochemistry represented through the CORPSE model (Sulman et al.,  
2651 2019) with an explicit treatment of soil microbes. LM4.1 also includes a new fire model FINAL  
2652 (Rabin et al., 2018). Vegetation dynamics [is](#) represented by the second generation age-height  
2653 structured approach, the Perfect Plasticity Approximation (PPA) (Weng et al., 2015; [Martinez](#)

Deleted: in prep.

Deleted: )

2657 Cano et al., 2019, [Allometric constraints and competition enable the simulation of size structure](#)  
2658 [and carbon fluxes in a dynamic vegetation model of tropical forests \(LM3PPA-TV\), in review](#).

2659 There are 6 carbon pools in LM4.1 representing leaves, fine roots, heartwood, sapwood, seeds,  
2660 and non-structural carbon (i.e. sugars). Litter is broken into leaf and coarse wood categories as  
2661 well into fast and slow timescale partitions. Soil has 20 vertical levels each with its own  
2662 prognostic state for energy, water and soil carbon variables. There are 5 types of vegetation  
2663 forms in LM4.1 representing C<sub>3</sub> grass, C<sub>4</sub> grass, tropical trees, temperate deciduous trees, cold  
2664 evergreen trees. A combination of these vegetation types could coexist in some location. The  
2665 model also includes a new treatment of stomatal conductance and plant hydraulics. The  
2666 vegetation state is used to drive a dust emission model that is coupled with the atmosphere for  
2667 transport (Ginoux et al., 2019, in prep.). ESM4 implementation of LM4.1 does not include an  
2668 interactive nitrogen cycle.

2669

2670 The ocean biogeochemical component of ESM4 is version 2 of the Carbon, Ocean  
2671 Biogeochemistry and Lower Trophics (COBALTV2) model (Stock et al., 2014b). COBALTV2 uses 33  
2672 tracers to represent carbon, alkalinity, oxygen, nitrogen, phosphorus, iron, silica, calcite and  
2673 lithogenic mineral cycling within the ocean. Relative to previous generation ocean  
2674 biogeochemistry models developed at GFDL, COBALTV2 includes an enhanced representation of  
2675 plankton food web dynamics to resolve the flow of energy from phytoplankton to fish (Stock et  
2676 al., 2014a) and enhance the model's capacity to resolve linkages between food webs and  
2677 biogeochemical cycles. COBALTV2 explicitly includes small, large (split into diatoms and non-  
2678 diatoms), and diazotrophic phytoplankton groups, three zooplankton groups, bacteria and three

**Deleted:** Tree allometry, height structured competition for light and the emergence of forest structure in a dynamic vegetation model of tropical forests LM3-PPA-TV, in prep.

2682 labilities of dissolved organic matter. Other updates include a temperature-dependence ~~for~~  
2683 sinking organic matter remineralization (Laufkötter et al., 2017), the addition of semi-labile  
2684 dissolved organic material, carbonate chemistry calculations based on the open source Model of  
2685 the Ocean Carbonate SYstem version 2.0 (Orr and Epitalon, 2015). [An evaluation of the ocean](#)  
2686 [biogeochemical simulation in ESM4.1 is presented in Stock et al. \(2019, Ocean Biogeochemistry](#)  
2687 [in GFDL's Earth System Model 4.1 and its Response to Increasing Atmospheric CO2, in review, J.](#)  
2688 [Adv. Mod. Earth Sys.\).](#)

Deleted: to

2690 Data from the NOAA-GFDL-ESM4 model used in the analysis presented in this paper are  
2691 accessible via the Earth System Grid Federation (ESGF) for 1pctCO2 (Krasting et al., 2019b)  
2692 simulation and for its radiatively- and biogeochemically-coupled configurations (Krasting et al.,  
2693 2019a).

#### 2694 A5.10. Norwegian Climate Centre (NCC) NorESM2-LM

2695 The NorESM2-LM ([Seland et al. 2020, The Norwegian Earth System Model, NorESM2 – Evaluation](#)  
2696 [of the CMIP6 DECK and historical simulations, Geosci. Model Dev. Discuss.,](#)  
2697 <https://doi.org/10.5194/gmd-2019-378>, in review) is based on the latest release of the  
2698 Community Earth System Model (CESM2.1), whose development is supported by the National  
2699 Center for Atmospheric Research at the United States. NorESM2 keeps the original land and sea-  
2700 ice components of CESM2.1 (i.e., CLM5, and CICE5, respectively). The atmospheric component is  
2701 CAM6 (as in CESM), but with modifications regarding the energy and angular momentum  
2702 conservation. Further, the atmospheric ~~aerosol~~ module of CAM6 has been replaced by the

Formatted: Font: 12 pt

Formatted: Font: 12 pt

Deleted: chemistry

2705 scheme developed by the Norwegian Meteorological Institute. The ocean physical and  
2706 biogeochemical components of NorESM2 are the isopycnal ocean circulation and carbon cycle  
2707 components updated from NorESM1 version (Tjiputra et al., 2013; Schwinger et al., 2016)

2708

2709 The CLM5 (Community Land Model version 5) prognostically simulates the carbon and nitrogen  
2710 cycles, which include natural vegetation, crops, and soil biogeochemistry. The carbon and  
2711 nitrogen budgets comprise leaf, live stem, dead stem, live coarse root, dead coarse root, fine-  
2712 root, and grain pools. Each of these pools has short-term and long-term storage of non-structural  
2713 carbohydrates and labile nitrogen. In addition to the vegetation pools, CLM includes a series of  
2714 decomposing carbon and nitrogen pools as vegetation successively breaks down to coarse woody  
2715 debris, and/or litter, and subsequently to soil organic matter. Details on the CLM5 models are  
2716 available in [Lawrence et al. \(2019\)](#).

2717

2718 Similar to the earlier version, the ocean carbon cycle component in NorESM2 is based on the  
2719 Hamburg Oceanic Carbon Cycle (HAMOCC; (Maier-Reimer et al., 2005)) model, which has been  
2720 adopted to the isopycnal ocean general circulation model. The current version includes new  
2721 processes, refined parameterizations, as well as new diagnostic tracers. The ecosystem model is  
2722 based on an NPZD-type model with multi nutrient limitation in its phytoplankton growth  
2723 formulation. Riverine fluxes of inorganic and organic carbon as well as nutrients are now  
2724 implemented. Unlike the earlier version, the sea-to-air dimethyl sulfate (DMS) fluxes alter the

Deleted: (Lawrence et al., 2018)

Formatted: Font: (Default) Calibri, 12 pt

Field Code Changed

Formatted: Font: (Default) Calibri, 12 pt

Formatted: Font: (Default) +Body (Calibri), 11 pt, Check spelling and grammar

2726 atmospheric radiative forcing and hence the climate carbon cycle feedback. More details on the  
2727 ocean carbon cycle of NorESM2 are available in [Tijputra et al. \(2020, accepted\)](#).  
2728

**Formatted:** Font: (Default) Calibri, 12 pt

**Deleted:** Tijputra et al. (2019, in preparation)

**Formatted:** Font: (Default) Calibri, 12 pt

**Formatted:** Font: (Default) Calibri, 12 pt

#### 2729 **A5.11. The United Kingdom Community Earth System Model, UKESM1-0-LL**

2730 UKESM1-0-LL (Sellar et al., 2019) is based upon the HadGEM3-GC3.1 (Williams et al., 2018) global  
2731 climate model which includes coupled ocean, atmosphere, land and sea-ice components. The  
2732 atmosphere component is the Unified Model with a resolution of 1.875° by 1.25° with 85 vertical  
2733 levels up to a model top of 90 km (Walters et al., 2019) and includes a modal aerosol scheme  
2734 (Mann et al., 2010). The ocean component uses the NEMO dynamical ocean at 1° resolution with  
2735 75 vertical levels (Storkey et al., 2018). The sea-ice component uses CICE on the same grid as the  
2736 ocean with 5-ice thickness categories (Ridley et al., 2018). The land component uses the JULES  
2737 land surface model (Wiltshire et al., in preparation), however, the land surface configuration is  
2738 substantially updated for UKESM. The primary differences between the physical and earth system  
2739 models is the inclusion of a terrestrial carbon and nitrogen cycle (Wiltshire et al., in preparation),  
2740 ocean biogeochemistry (Yool et al., 2013) and tropospheric-stratospheric chemistry model.  
2741 Atmospheric chemistry in UKESM1 is simulated by the UKCA chemistry and aerosol model with  
2742 the specific configuration a combination of tropospheric (O'Connor et al., 2014) and stratospheric  
2743 chemistry (Morgenstern et al., 2009, 2017).

**Field Code Changed**

**Deleted:** s

2744

2745 Terrestrial biogeochemistry is represented by the JULES-ES model cycle (Wiltshire et al., in  
2746 preparation). The land surface is represented by 13 plant functional types (PFTs) including 4



2749 managed crop and pasture land types. The height, leaf area index and spatial distribution of the  
 2750 PFTs are dynamic simulated by TRIFFID dynamic global vegetation model (Cox, 2001). Soil carbon  
 2751 is represented by the 4 pool Roth-C scheme (Coleman and Jenkinson, 1999). Terrestrial carbon  
 2752 uptake may be limited by the availability of nitrogen. Nitrogen does not directly affect  
 2753 photosynthetic capacity through leaf N concentrations but acts indirectly by controlling the  
 2754 biomass and leaf area index within the TRIFFID DGVM. A second mechanism acts through soil  
 2755 carbon by limiting the decomposition of litter into soil carbon in the RothC model. The vegetation  
 2756 model includes retranslocation of ~~n~~itrogen during senescence of leaves and roots into a labile  
 2757 pool to supply nutrients for the following seasonal leaf out. The soil model simulates  
 2758 mineralization and immobilization with mineralized nitrogen becoming available for plant uptake  
 2759 and ecosystem loss. Inorganic ~~n~~itrogen is represented by a single gridbox pool from which all  
 2760 PFTs have equal access. Nitrogen deposition is prescribed from ancillary data.

Deleted: N

Deleted: s

Deleted: s

Deleted: s

Deleted: N

2761  
 2762 Land-use change is represented by the application of time-varying fields of crop and pasture to  
 2763 the DGVM, which allocates space dynamically to C<sub>3</sub> and C<sub>4</sub>, crop and pasture types. Pasture is  
 2764 represented as natural grass whereas crops include a harvest parameterization and are fertilized.

2765 Biogenic ~~v~~olatile ~~o~~rganic ~~c~~ompound (BVOC) emissions from vegetation are simulated and affect  
 2766 the formation of secondary organic aerosols. Mineral dust is emitted from bare soil and acts as  
 2767 both an aerosol and a fertilizer to the ocean.

Deleted: V

Deleted: O

Deleted: C

Deleted: s

2778 Ocean biogeochemistry is represented by MEDUSA-2 (Yool et al., 2013) which resolves a dual  
 2779 size-structured ecosystem of small (nanophytoplankton and microzooplankton) and large  
 2780 (microphytoplankton and mesozooplankton) components. This explicitly includes the  
 2781 biogeochemical cycles of nitrogen, silicon and iron nutrients as well as the cycles of carbon,  
 2782 alkalinity and dissolved oxygen. Large phytoplankton are treated as diatoms and utilize silicic acid  
 2783 in addition to nitrogen, iron and carbon. Like the living components, the detrital components are  
 2784 split into two size classes. At the seafloor, MEDUSA-2 resolves 5 reservoirs to temporarily store  
 2785 sinking organic material reaching the sediment. The model's nitrogen, silicon and alkalinity cycles  
 2786 are closed and conservative (e.g. no riverine inputs), while the other three cycles (carbon, iron,  
 2787 oxygen) are open. The ocean's iron cycle includes aeolian (land derived dust) and benthic sources,  
 2788 and is depleted by scavenging. The ocean's carbon cycle exchanges CO<sub>2</sub> with the atmosphere.  
 2789 The ocean's oxygen cycle exchanges with the atmosphere, and dissolved oxygen is additionally  
 2790 created by primary production and depleted by remineralisation. Ocean biogeochemistry also  
 2791 feeds back on the atmosphere through the production of marine DMS and marine organic  
 2792 aerosols.

Deleted: s

#### 2794 **A6. Contribution of uncertainties in $\Delta T_{2\times CO_2}$ and $\tilde{E}_{2\times CO_2}$ to TCRE.**

2796 The uncertainty in TCRE, as indicated by its standard deviation ( $\sigma_{TCRE}$ ), can be represented in  
 2797 terms of the standard deviation of  $\Delta T_{2\times CO_2}$  ( $\sigma_{\Delta T}$ ), standard deviation of  $\tilde{E}_{2\times CO_2}$  ( $\sigma_{\tilde{E}}$ ), and their  
 2798 means  $\overline{\Delta T}$  and  $\overline{E}$  across the eleven CMIP6 models. Since  $\Delta T_{2\times CO_2}$  and  $\tilde{E}_{2\times CO_2}$  are nearly

2800 independent (correlation between these two quantities is only 0.02 across the eleven CMIP6  
2801 models considered here), we can write

$$2802 \quad \sigma_{TCRE} = \overline{TCRE} \cdot \sqrt{\left(\frac{\sigma_{\Delta T}}{\Delta T}\right)^2 + \left(\frac{\sigma_E}{E}\right)^2} \quad (A8)$$

2803 which allows to calculate to contributions of  $\left(\frac{\sigma_{\Delta T}}{\Delta T}\right)^2$  and  $\left(\frac{\sigma_E}{E}\right)^2$  to  $\sigma_{TCRE}$ .

2804

2805

2806

2807

2808

2809

2810

2811

2812

2813

2814

## References

- Ainsworth, E. A. and Long, S. P.: What have we learned from 15 years of free-air CO<sub>2</sub> enrichment (FACE)? A meta-analytic review of the responses of photosynthesis, canopy properties and plant production to rising CO<sub>2</sub>, *New Phytol.*, 165(2), 351–372, doi:10.1111/j.1469-8137.2004.01224.x, 2005.
- Arora, V. K. and Boer, G. J.: A parameterization of leaf phenology for the terrestrial ecosystem component of climate models, *Glob. Change Biol.*, 11(1), 39–59, doi:10.1111/j.1365-2486.2004.00890.x, 2005.
- Arora, V. K. and Boer, G. J.: Uncertainties in the 20th century carbon budget associated with land use change, *Glob. Change Biol.*, 16(12), 3327–3348, 2010.
- Arora, V. K. and Scinocca, J. F.: Constraining the strength of the terrestrial CO<sub>2</sub> fertilization effect in the Canadian Earth system model version 4.2 (CanESM4.2), *Geosci. Model Dev.*, 9(7), 2357–2376, doi:10.5194/gmd-9-2357-2016, 2016.
- Arora, V. K., Scinocca, J. F., Boer, G. J., Christian, J. R., Denman, K. L., Flato, G. M., Kharin, V. V., Lee, W. G. and Merryfield, W. J.: Carbon emission limits required to satisfy future representative concentration pathways of greenhouse gases, *Geophys. Res. Lett.*, 38(5), doi:10.1029/2010GL046270, 2011.
- Arora, V. K., Boer, G. J., Friedlingstein, P., Eby, M., Jones, C. D., Christian, J. R., Bonan, G., Bopp, L., Brovkin, V., Cadule, P., Hajima, T., Ilyina, T., Lindsay, K., Tjiputra, J. F. and Wu, T.: Carbon–Concentration and Carbon–Climate Feedbacks in CMIP5 Earth System Models, *J. Clim.*, 26(15), 5289–5314, doi:10.1175/JCLI-D-12-00494.1, 2013.
- Arora, V. K., Melton, J. R. and Plummer, D.: An assessment of natural methane fluxes simulated by the CLASS-CTEM model, *Biogeosciences*, 15(15), 4683–4709, doi:10.5194/bg-15-4683-2018, 2018.
- Aumont, O., Ethé, C., Tagliabue, A., Bopp, L. and Gehlen, M.: PISCES-v2: an ocean biogeochemical model for carbon and ecosystem studies, *Geosci. Model Dev.*, 8(8), 2465–2513, doi:10.5194/gmd-8-2465-2015, 2015.
- Bernard, B., Madec, G., Penduff, T., Molines, J.-M., Treguier, A.-M., Le Sommer, J., Beckmann, A., Biastoch, A., Böning, C., Dengg, J., Derval, C., Durand, E., Gulev, S., Remy, E., Talandier, C., Theetten, S., Maltrud, M., McClean, J. and De Cuevas, B.: Impact of partial steps and momentum advection schemes in a global ocean circulation model at eddy-permitting resolution, *Ocean Dyn.*, 56(5), 543–567, doi:10.1007/s10236-006-0082-1, 2006.
- Bernardello, R., Marinov, I., Palter, J. B., Sarmiento, J. L., Galbraith, E. D. and Slater, R. D.: Response of the Ocean Natural Carbon Storage to Projected Twenty-First-Century Climate Change, *J. Clim.*, 27(5), 2033–2053, doi:10.1175/JCLI-D-13-00343.1, 2014.
- Bi, D., Dix, M., Marsland, S., O’Farrell, S., Rashid, H., Uotila, P., Hirst, A., Kowalczyk, E., Golebiewski, M., Sullivan, A., Yan, H., Hannah, N., Franklin, C., Sun, Z., Vohralik, P., Watterson, I., Zhou, X., Fiedler, R., Collier, M., Ma, Y., Noonan, J., Stevens, L., Uhe, P., Zhu, H., Griffies, S., Hill, R., Harris, C. and Puri, K.: The ACCESS coupled model: description, control climate and evaluation, *Aust Meteor Oceanogr J*, 63(1), 41–64, doi:https://doi.org/10.22499/2.6301.004, 2013.

Formatted: Bibliography, Widow/Orphan control, Adjust space between Latin and Asian text, Adjust space between Asian text and numbers

2853 [Boer, G. J. and Arora, V.: Geographic Aspects of Temperature and Concentration Feedbacks in the](#)  
2854 [Carbon Budget, J. Clim., 23\(3\), 775–784, doi:10.1175/2009JCLI3161.1, 2010.](#)

2855 [Bouillon, S., Maqueda, M. Á. M., Legat, V. and Fichefet, T.: An elastic–viscous–plastic sea ice model](#)  
2856 [formulated on Arakawa B and C grids, Ocean Model., 27\(3\), 174–184,](#)  
2857 [doi:https://doi.org/10.1016/j.ocemod.2009.01.004, 2009.](#)

2858 [Bounoua, L., Collatz, G. J., Sellers, P. J., Randall, D. A., Dazlich, D. A., Los, S. O., Berry, J. A., Fung, I.,](#)  
2859 [Tucker, C. J., Field, C. B. and Jensen, T. G.: Interactions between Vegetation and Climate: Radiative and](#)  
2860 [Physiological Effects of Doubled Atmospheric CO<sub>2</sub>, J. Clim., 12\(2\), 309–324, doi:10.1175/1520-](#)  
2861 [0442\(1999\)012<0309:IBVACR>2.0.CO;2, 1999.](#)

2862 [Brovkin, V., Lorenz, S., Raddatz, T., Ilyina, T., Stemmler, I., Toohey, M. and Claussen, M.: What was the](#)  
2863 [source of the atmospheric CO<sub>2</sub> increase during the Holocene?, Biogeosciences, 16\(13\), 2543–2555,](#)  
2864 [doi:10.5194/bg-16-2543-2019, 2019.](#)

2865 [Cao, L., Bala, G., Caldeira, K., Nemani, R. and Ban-Weiss, G.: Importance of carbon dioxide physiological](#)  
2866 [forcing to future climate change, Proc. Natl. Acad. Sci., 107\(21\), 9513, doi:10.1073/pnas.0913000107,](#)  
2867 [2010.](#)

2868 [Ceppi, P. and Gregory, J. M.: Relationship of tropospheric stability to climate sensitivity and Earth’s](#)  
2869 [observed radiation budget, Proc. Natl. Acad. Sci., 114\(50\), 13126–13131, doi:10.1073/pnas.1714308114,](#)  
2870 [2017.](#)

2871 [Chadwick, R., Douville, H. and Skinner, C. B.: Timeslice experiments for understanding regional climate](#)  
2872 [projections: applications to the tropical hydrological cycle and European winter circulation, Clim. Dyn.,](#)  
2873 [doi:10.1007/s00382-016-3488-6, 2017.](#)

2874 [Choudhury, B. J.: Carbon use efficiency, and net primary productivity of terrestrial vegetation, Adv.](#)  
2875 [Space Res., 26\(7\), 1105–1108, doi:https://doi.org/10.1016/S0273-1177\(99\)01126-6, 2000.](#)

2876 [Christian, J. R., Arora, V. K., Boer, G. J., Curry, C. L., Zahariev, K., Denman, K. L., Flato, G. M., Lee, W. G.,](#)  
2877 [Merryfield, W. J., Roulet, N. T. and Scinocca, J. F.: The global carbon cycle in the Canadian Earth system](#)  
2878 [model \(CanESM1\): Preindustrial control simulation, J. Geophys. Res. Biogeosciences, 115\(G3\),](#)  
2879 [doi:10.1029/2008JG000920, 2010.](#)

2880 [Coleman, K. and Jenkinson, D. S.: RothC-26.3 - A model for the turnover of carbon in soil: Model](#)  
2881 [description and users guide, Rothamsted Research, Harpenden, U.K. \[online\] Available from:](#)  
2882 [https://www.rothamsted.ac.uk/sites/default/files/RothC\\_guide\\_WIN.pdf, 1999.](#)

2883 [Collatz, G., Ribas-Carbo, M. and Berry, J.: Coupled Photosynthesis-Stomatal Conductance Model for](#)  
2884 [Leaves of C4 Plants, Funct. Plant Biol., 19\(5\), 519–538, 1992.](#)

2885 [Cox, P.: Description of the TRIFFID Dynamic Global Vegetation Model, Hadley Centre Technical Note #](#)  
2886 [24, UK Met Office. \[online\] Available from: https://digital.nmla.metoffice.gov.uk/IO\\_cc8f146a-d524-](#)  
2887 [4243-88fc-e3a3bcd782e7/, 2001.](#)

2888 [Cramer, W.: Using plant functional types in a global vegetation model, in Smith, T.M., Shugart, H.H. &](#)  
2889 [Woodward, F.I. \(eds.\) Plant functional types: their relevance to ecosystem properties and global change,](#)  
2890 [pp. 271–288, Cambridge University Press, Cambridge., 1997.](#)

2891 [Decharme, B., Delire, C., Minvielle, M., Colin, J., Vergnes, J.-P., Alias, A., Saint-Martin, D., Séférian, R.,](#)  
2892 [Sénési, S. and Voldoire, A.: Recent Changes in the ISBA-CTRIP Land Surface System for Use in the CNRM-](#)  
2893 [CM6 Climate Model and in Global Off-Line Hydrological Applications, J. Adv. Model. Earth Syst., 11\(5\),](#)  
2894 [1207–1252, doi:10.1029/2018MS001545, 2019.](#)

2895 [Delire, C., Séférian, R., Decharme, B., Alkama, R., Carrer, D., Joetzjer, E., Morel, X. and Rocher, M.: The](#)  
2896 [global land carbon cycle simulated with ISBA, Journal of Advances in Modeling Earth Systems, JAMES,](#)  
2897 [submitted, 2019.](#)

2898 [Donner, L. J., Wyman, B. L., Hemler, R. S., Horowitz, L. W., Ming, Y., Zhao, M., Golaz, J.-C., Ginoux, P., Lin,](#)  
2899 [S.-J., Schwarzkopf, M. D., Austin, J., Alaka, G., Cooke, W. F., Delworth, T. L., Freidenreich, S. M., Gordon,](#)  
2900 [C. T., Griffies, S. M., Held, I. M., Hurlin, W. J., Klein, S. A., Knutson, T. R., Langenhorst, A. R., Lee, H.-C.,](#)  
2901 [Lin, Y., Magi, B. I., Malyshev, S. L., Milly, P. C. D., Naik, V., Nath, M. J., Pincus, R., Ploshay, J. J.,](#)  
2902 [Ramaswamy, V., Seman, C. J., Shevliakova, E., Sirutis, J. J., Stern, W. F., Stouffer, R. J., Wilson, R. J.,](#)  
2903 [Winton, M., Wittenberg, A. T. and Zeng, F.: The Dynamical Core, Physical Parameterizations, and Basic](#)  
2904 [Simulation Characteristics of the Atmospheric Component AM3 of the GFDL Global Coupled Model CM3,](#)  
2905 [J. Clim., 24\(13\), 3484–3519, doi:10.1175/2011JCLI3955.1, 2011.](#)

2906 [Dunne, J. P., John, J. G., Adcroft, A. J., Griffies, S. M., Hallberg, R. W., Shevliakova, E., Stouffer, R. J.,](#)  
2907 [Cooke, W., Dunne, K. A., Harrison, M. J., Krasting, J. P., Malyshev, S. L., Milly, P. C. D., Philipps, P. J.,](#)  
2908 [Sentman, L. T., Samuels, B. L., Spelman, M. J., Winton, M., Wittenberg, A. T. and Zadeh, N.: GFDL's ESM2](#)  
2909 [Global Coupled Climate–Carbon Earth System Models. Part I: Physical Formulation and Baseline](#)  
2910 [Simulation Characteristics, J. Clim., 25\(19\), 6646–6665, doi:10.1175/JCLI-D-11-00560.1, 2012.](#)

2911 [Dunne, J. P., John, J. G., Shevliakova, E., Stouffer, R. J., Krasting, J. P., Malyshev, S. L., Milly, P. C. D.,](#)  
2912 [Sentman, L. T., Adcroft, A. J., Cooke, W., Dunne, K. A., Griffies, S. M., Hallberg, R. W., Harrison, M. J.,](#)  
2913 [Levy, H., Wittenberg, A. T., Phillips, P. J. and Zadeh, N.: GFDL's ESM2 Global Coupled Climate–Carbon](#)  
2914 [Earth System Models. Part II: Carbon System Formulation and Baseline Simulation Characteristics, J.](#)  
2915 [Clim., 26\(7\), 2247–2267, doi:10.1175/JCLI-D-12-00150.1, 2013.](#)

2916 [Eyring, V., Bony, S., Meehl, G. A., Senior, C. A., Stevens, B., Stouffer, R. J. and Taylor, K. E.: Overview of](#)  
2917 [the Coupled Model Intercomparison Project Phase 6 \(CMIP6\) experimental design and organization,](#)  
2918 [Geosci. Model Dev., 9\(5\), 1937–1958, doi:10.5194/gmd-9-1937-2016, 2016.](#)

2919 [Farquhar, G. D., von Caemmerer, S. and Berry, J. A.: A biochemical model of photosynthetic CO<sub>2</sub>](#)  
2920 [assimilation in leaves of C<sub>3</sub> species, Planta, 149\(1\), 78–90, doi:10.1007/BF00386231, 1980.](#)

2921 [Fichefet, T. and Morales Maqueda, M. A.: Sensitivity of a global sea ice model to the treatment of ice](#)  
2922 [thermodynamics and dynamics, J. Geophys. Res. Oceans, 102\(C6\), 12609–12646,](#)  
2923 [doi:10.1029/97JC00480, 1997.](#)

2924 [Fisher, R. A., Wieder, W. R., Sanderson, B. M., Koven, C. D., Oleson, K. W., Xu, C., Fisher, J. B., Shi, M.,](#)  
2925 [Walker, A. P. and Lawrence, D. M.: Parametric Controls on Vegetation Responses to Biogeochemical](#)  
2926 [Forcing in the CLM5, J. Adv. Model. Earth Syst., 11, doi:10.1029/2019MS001609, 2019.](#)

2927 [Follows, M. J., Ito, T. and Dutkiewicz, S.: On the solution of the carbonate chemistry system in ocean](#)  
 2928 [biogeochemistry models, Ocean Model., 12\(3\), 290–301,](#)  
 2929 [doi:https://doi.org/10.1016/j.ocemod.2005.05.004, 2006.](#)

2930 [Frame, D. J., Macey, A. H. and Allen, M. R.: Cumulative emissions and climate policy, Nat. Geosci., 7, 692,](#)  
 2931 [2014.](#)

2932 [Friedlingstein, P., Cox, P., Betts, R., Bopp, L., Von Bloh, W., Brovkin, V., Cadule, P., Doney, S., Eby, M.,](#)  
 2933 [Fung, I., Bala, G., John, J., Jones, C., Joos, F., Kato, T., Kawamiya, M., Knorr, W., Lindsay, K., Matthews, H.](#)  
 2934 [D., Raddatz, T., Rayner, P., Reick, C., Roeckner, E., Schnitzler, K.-G., Schnur, R., Strassmann, K., Weaver,](#)  
 2935 [A. J., Yoshikawa, C., Zeng, A. N. and Friedlingstein, P.: Climate–Carbon Cycle Feedback Analysis: Results](#)  
 2936 [from the C 4 MIP Model Intercomparison, 2006.](#)

2937 [Gillett, N. P., Arora, V. K., Matthews, D. and Allen, M. R.: Constraining the Ratio of Global Warming to](#)  
 2938 [Cumulative CO2 Emissions Using CMIP5 Simulations, J. Clim., 26\(18\), 6844–6858, doi:10.1175/JCLI-D-12-](#)  
 2939 [00476.1, 2013.](#)

2940 [Giorgetta, M. A., Jungclaus, J., Reick, C. H., Legutke, S., Bader, J., Böttinger, M., Brovkin, V., Crueger, T.,](#)  
 2941 [Esch, M., Fieg, K., Glushak, K., Gayler, V., Haak, H., Hollweg, H.-D., Ilyina, T., Kinne, S., Kornblueh, L.,](#)  
 2942 [Matei, D., Mauritsen, T., Mikolajewicz, U., Mueller, W., Notz, D., Pithan, F., Raddatz, T., Rast, S., Redler,](#)  
 2943 [R., Roeckner, E., Schmidt, H., Schnur, R., Segschneider, J., Six, K. D., Stockhause, M., Timmreck, C.,](#)  
 2944 [Wegner, J., Widmann, H., Wieners, K.-H., Claussen, M., Marotzke, J. and Stevens, B.: Climate and carbon](#)  
 2945 [cycle changes from 1850 to 2100 in MPI-ESM simulations for the Coupled Model Intercomparison](#)  
 2946 [Project phase 5, J. Adv. Model. Earth Syst., 5\(3\), 572–597, doi:10.1002/jame.20038, 2013.](#)

2947 [Goll, D. S., Brovkin, V., Liski, J., Raddatz, T., Thum, T. and Todd-Brown, K. E. O.: Strong dependence of](#)  
 2948 [CO2 emissions from anthropogenic land cover change on initial land cover and soil carbon](#)  
 2949 [parametrization, Glob. Biogeochem. Cycles, 29\(9\), 1511–1523, doi:10.1002/2014GB004988, 2015.](#)

2950 [Goll, D. S., Winkler, A. J., Raddatz, T., Dong, N., Prentice, I. C., Ciais, P. and Brovkin, V.: Carbon–nitrogen](#)  
 2951 [interactions in idealized simulations with JSBACH \(version 3.10\), Geosci. Model Dev., 10\(5\), 2009–2030,](#)  
 2952 [doi:10.5194/gmd-10-2009-2017, 2017.](#)

2953 [Goodwin, P. and Lenton, T. M.: Quantifying the feedback between ocean heating and CO2 solubility as](#)  
 2954 [an equivalent carbon emission, Geophys. Res. Lett., 36\(15\), doi:10.1029/2009GL039247, 2009.](#)

2955 [Goudriaan, J., van Laar, H. H., van Keulen, H. and Louwerse, W.: Photosynthesis, CO2 and Plant](#)  
 2956 [Production, in Wheat Growth and Modelling, edited by W. Day and R. K. Atkin, pp. 107–122, Springer](#)  
 2957 [US, Boston, MA., 1985.](#)

2958 [Grandpeix, J.-Y. and Lafore, J.-P.: A Density Current Parameterization Coupled with Emanuel’s](#)  
 2959 [Convection Scheme. Part I: The Models, J. Atmospheric Sci., 67\(4\), 881–897,](#)  
 2960 [doi:10.1175/2009JAS3044.1, 2010.](#)

2961 [Grandpeix, J.-Y., Lafore, J.-P. and Cheruy, F.: A Density Current Parameterization Coupled with Emanuel’s](#)  
 2962 [Convection Scheme. Part II: 1D Simulations, J. Atmospheric Sci., 67\(4\), 898–922,](#)  
 2963 [doi:10.1175/2009JAS3045.1, 2010.](#)

2964 [Gregory, J. M., Jones, C. D., Cadule, P. and Friedlingstein, P.: Quantifying Carbon Cycle Feedbacks, J. Clim., 22\(19\), 5232–5250, doi:10.1175/2009JCLI2949.1, 2009a.](#)  
 2965  
 2966 [Gregory, J. M., Jones, C. D., Cadule, P. and Friedlingstein, P.: Quantifying Carbon Cycle Feedbacks, J. Clim., 22\(19\), 5232–5250, doi:10.1175/2009JCLI2949.1, 2009b.](#)  
 2967  
 2968 [Griffies, S. M.: Elements of the Modular Ocean Model \(MOM\) \(2012 release with update\), GFDL Ocean Group Technical report No. 7, NOAA/GFDL., 2014.](#)  
 2969  
 2970 [Gruber, N., Sarmiento, J. L. and Stocker, T. F.: An improved method for detecting anthropogenic CO<sub>2</sub> in the oceans, Glob. Biogeochem. Cycles, 10\(4\), 809–837, doi:10.1029/96GB01608, 1996.](#)  
 2971  
 2972 [Hajima, T., Tachiiri, K., Ito, A. and Kawamiya, M.: Uncertainty of Concentration–Terrestrial Carbon Feedback in Earth System Models, J. Clim., 27\(9\), 3425–3445, doi:10.1175/JCLI-D-13-00177.1, 2014.](#)  
 2973  
 2974 [Hajima, T., Watanabe, M., Yamamoto, A., Tatebe, H., Noguchi, M. A., Abe, M., Ohgaito, R., Ito, A., Yamazaki, D., Okajima, H., Ito, A., Takata, K., Ogochi, K., Watanabe, S. and Kawamiya, M.: Description of the MIROC-ES2L Earth system model and evaluation of its climate–biogeochemical processes and feedbacks, Geosci. Model Dev., accepted, doi:10.5194/gmd-2019-275, 2020.](#)  
 2975  
 2976  
 2977  
 2978 [Hansen, J., Lacis, A., Rind, D., Russell, G., Stone, P., Fung, I., Ruedy, R. and Lerner, J.: Climate Sensitivity: Analysis of Feedback Mechanisms, in Climate Processes and Climate Sensitivity, pp. 130–163, American Geophysical Union \(AGU\)., 1984.](#)  
 2979  
 2980  
 2981 [Hasumi, H.: CCSR Ocean Component Model \(COCO\) version 4.0, University of Tokyo. \[online\] Available from: <https://ccsr.aori.u-tokyo.ac.jp/~hasumi/COCO/coco4.pdf>, 2015.](#)  
 2982  
 2983 [Hawkins, E. and Sutton, R.: The potential to narrow uncertainty in regional climate predictions, Bull. Am. Meteorol. Soc., doi:10.1175/2009BAMS2607.1, 2009.](#)  
 2984  
 2985 [Held, I. M., Guo, H., Adcroft, A., Dunne, J. P., Horowitz, L. W., Krasting, J., Shevliakova, E., Winton, M., Zhao, M., Bushuk, M., Wittenberg, A. T., Wyman, B., Xiang, B., Zhang, R., Anderson, W., Balaji, V., Donner, L., Dunne, K., Durachta, J., Gauthier, P. P. G., Ginoux, P., Golaz, J.-C., Griffies, S. M., Hallberg, R., Harris, L., Harrison, M., Hurlin, W., John, J., Lin, P., Lin, S.-J., Malyshev, S., Menzel, R., Milly, P. C. D., Ming, Y., Naik, V., Paynter, D., Paulot, F., Rammaswamy, V., Reichl, B., Robinson, T., Rosati, A., Seman, C., Silvers, L. G., Underwood, S. and Zadeh, N.: Structure and Performance of GFDL’s CM4.0 Climate Model, J. Adv. Model. Earth Syst., 11\(11\), 3691–3727, doi:10.1029/2019MS001829, 2019.](#)  
 2986  
 2987  
 2988  
 2989  
 2990  
 2991  
 2992 [Hourdin, F., Couvreux, F. and Menut, L.: Parameterization of the Dry Convective Boundary Layer Based on a Mass Flux Representation of Thermals, J. Atmospheric Sci., 59\(6\), 1105–1123, doi:10.1175/1520-0469\(2002\)059<1105:POTDCB>2.0.CO;2, 2002.](#)  
 2993  
 2994  
 2995 [Hourdin, F., Rio, C., Grandpeix, J.-Y., Madeleine, J.-B., Cheruy, F., Rochetin, N., Musat, I., Idelkadi, A., Fairhead, L., Foujols, M.-A., Ghattas, J., Mellul, L., Traore, A.-K., Gastineau, G., Dufresne, J.-L., Lefebvre, M.-P., Millour, E., Vignon, E., Jouaud, J., Bonazzola, M. and Lott, F.: LMDZ6: the improved atmospheric component of the IPSL coupled model, submitted, 2019.](#)  
 2996  
 2997  
 2998  
 2999 [Hunke, E. C. and Lipscomb, W. H.: The Los Alamos sea ice model documentation and software user’s manual, Version 4.1. LA-CC-06-012, Los Alamos National Laboratory., 2010.](#)  
 3000



3001 [Hunke, E. C., Lipscomb, W. H., Turner, A. K., Jeffery, N. and Elliott, S.: CICE: The Los Alamos Sea Ice](#)  
 3002 [Model. Documentation and Software User's Manual. Version 5.1, T-3 Fluid Dynamics Group, Los Alamos](#)  
 3003 [National Laboratory., 2015.](#)

3004 [Hurttt, G. C., Frolking, S., Fearon, M. G., Moore, B., Shevliakova, E., Malyshev, S., Pacala, S. W. and](#)  
 3005 [Houghton, R. A.: The underpinnings of land-use history: three centuries of global gridded land-use](#)  
 3006 [transitions, wood-harvest activity, and resulting secondary lands, Glob. Change Biol., 12\(7\), 1208–1229,](#)  
 3007 [doi:10.1111/j.1365-2486.2006.01150.x, 2006.](#)

3008 [Ilyina, T., Six, K. D., Segschneider, J., Maier-Reimer, E., Li, H. and Núñez-Riboni, I.: Global ocean](#)  
 3009 [biogeochemistry model HAMOCC: Model architecture and performance as component of the MPI-Earth](#)  
 3010 [system model in different CMIP5 experimental realizations, J. Adv. Model. Earth Syst., 5\(2\), 287–315,](#)  
 3011 [doi:10.1029/2012MS000178, 2013.](#)

3012 [IPCC: Climate Change 2014: Synthesis Report. Contribution of Working Groups I, II and III to the Fifth](#)  
 3013 [Assessment Report of the Intergovernmental Panel on Climate Change \[Core Writing Team, R.K.](#)  
 3014 [Pachauri and L.A. Meyer \(eds.\), Intergovernmental Panel on Climate Change, Geneva, Switzerland, 151](#)  
 3015 [pp. \[online\] Available from: https://www.ipcc.ch/report/ar5/syr/, 2014.](#)

3016 [Ito, A. and Inatomi, M.: Water-Use Efficiency of the Terrestrial Biosphere: A Model Analysis Focusing on](#)  
 3017 [Interactions between the Global Carbon and Water Cycles, J. Hydrometeorol., 13\(2\), 681–694,](#)  
 3018 [doi:10.1175/JHM-D-10-05034.1, 2012.](#)

3019 [Ito, A. and Oikawa, T.: A simulation model of the carbon cycle in land ecosystems \(Sim-CYCLE\): a](#)  
 3020 [description based on dry-matter production theory and plot-scale validation, Ecol. Model., 151\(2\), 143–](#)  
 3021 [176, doi:https://doi.org/10.1016/S0304-3800\(01\)00473-2, 2002.](#)

3022 [Ito, T. and Follows, M. J.: Preformed phosphate, soft tissue pump and atmospheric CO<sub>2</sub>, J. Mar. Res.,](#)  
 3023 [63\(4\), 813–839, doi:doi:10.1357/0022240054663231, 2005.](#)

3024 [Jones, C. D. and Friedlingstein, P.: Quantifying process-level uncertainty contributions to TCRE and](#)  
 3025 [Carbon Budgets for meeting Paris Agreement climate targets, Environ. Res. Lett. \[online\] Available from:](#)  
 3026 [http://iopscience.iop.org/10.1088/1748-9326/ab858a, 2020.](#)

3027 [Jones, C. D., Arora, V., Friedlingstein, P., Bopp, L., Brovkin, V., Dunne, J., Graven, H., Hoffman, F., Ilyina,](#)  
 3028 [T., John, J. G., Jung, M., Kawamiya, M., Koven, C., Pongratz, J., Raddatz, T., Randerson, J. T. and Zaehle,](#)  
 3029 [S.: C4MIP – The Coupled Climate–Carbon Cycle Model Intercomparison Project: experimental protocol](#)  
 3030 [for CMIP6, Geosci. Model Dev., 9\(8\), 2853–2880, doi:10.5194/gmd-9-2853-2016, 2016.](#)

3031 [Katavouta, A., Williams, R. G., Goodwin, P. and Roussenov, V.: Reconciling Atmospheric and Oceanic](#)  
 3032 [Views of the Transient Climate Response to Emissions, Geophys. Res. Lett., 45\(12\), 6205–6214,](#)  
 3033 [doi:10.1029/2018GL077849, 2018.](#)

3034 [Koven, C. D., Chambers, J. Q., Georgiou, K., Knox, R., Negron-Juarez, R., Riley, W. J., Arora, V. K., Brovkin,](#)  
 3035 [V., Friedlingstein, P. and Jones, C. D.: Controls on terrestrial carbon feedbacks by productivity versus](#)  
 3036 [turnover in the CMIP5 Earth System Models, Biogeosciences, doi:10.5194/bg-12-5211-2015, 2015.](#)

3037 [Kowalczyk, E. A., Stevens, L., Law, R. M., Dix, M., Wang, Y. P., Harman, I. N., Haynes, K., Srbinovsky, J.,](#)  
3038 [Pak, B. and Ziehn, T.: The land surface model component of ACCESS: description and impact on the](#)  
3039 [simulated surface climatology, Aust Meteor Oceanogr J, 63, 65–82, 2013.](#)

3040 [Krasting, J. P., Blanton, C., McHugh, C., Radhakrishnan, A., John, J. G., Rand, K., Nikonov, S., Vahlenkamp,](#)  
3041 [H., Zadeh, N. T., Dunne, J. P., Shevliakova, E., Horowitz, L. W., Stock, C., Malyshev, S., Ploshay, J.,](#)  
3042 [Gauthier, P. P., Naik, V. and Winton, M.: NOAA-GFDL GFDL-ESM4 model output prepared for CMIP6](#)  
3043 [C4MIP, Earth Syst. Grid Fed., DOI:10.22033/ESGF/CMIP6.1405 \[online\] Available from: \[http://esgf-\]\(http://esgf-node.llnl.gov/search/cmip6/?mip\_era=CMIP6&activity\_id=C4MIP&institution\_id=NOAA-GFDL&source\_id=GFDL-ESM4doi.org/10.22033/ESGF/CMIP6.1405\)](#)  
3044 [node.llnl.gov/search/cmip6/?mip\\_era=CMIP6&activity\\_id=C4MIP&institution\\_id=NOAA-](#)  
3045 [GFDL&source\\_id=GFDL-ESM4doi.org/10.22033/ESGF/CMIP6.1405](#), 2019a.

3046 [Krasting, J. P., John, J. G., Blanton, C., McHugh, C., Nikonov, S., Radhakrishnan, A., Rand, K., Zadeh, N. T.,](#)  
3047 [Balaji, V., Durachta, J., Dupuis, C., Menzel, R., Robinson, T., Underwood, S., Vahlenkamp, H., Dunne, K.](#)  
3048 [A., Gauthier, P. P., Ginoux, P., Griffies, S. M., Hallberg, R., Harrison, M., Hurlin, W., Malyshev, S., Naik, V.,](#)  
3049 [Paulot, F., Paynter, D. J., Ploshay, J., Schwarzkopf, D. M., Seman, C. J., Silvers, L., Wyman, B., Zeng, Y.,](#)  
3050 [Adcroft, A., Dunne, J. P., Guo, H., Held, I. M., Horowitz, L. W., Milly, P. C. D., Shevliakova, E., Stock, C.,](#)  
3051 [Winton, M. and Zhao, M.: NOAA-GFDL GFDL-ESM4 model output prepared for CMIP6 CMIP, Earth Syst.](#)  
3052 [Grid Fed., DOI:10.22033/ESGF/CMIP6.1407 \[online\] Available from: \[http://esgf-\]\(http://esgf-node.llnl.gov/search/cmip6/?mip\_era=CMIP6&activity\_id=CMIP&institution\_id=NOAA-GFDL&source\_id=GFDL-ESM4doi.org/10.22033/ESGF/CMIP6.1407\)](#)  
3053 [node.llnl.gov/search/cmip6/?mip\\_era=CMIP6&activity\\_id=CMIP&institution\\_id=NOAA-](#)  
3054 [GFDL&source\\_id=GFDL-ESM4doi.org/10.22033/ESGF/CMIP6.1407](#), 2019b.

3055 [Krinner, G., Viovy, N., de Noblet-Ducoudré, N., Ogée, J., Polcher, J., Friedlingstein, P., Ciais, P., Sitch, S.](#)  
3056 [and Prentice, I. C.: A dynamic global vegetation model for studies of the coupled atmosphere-biosphere](#)  
3057 [system: DVGM FOR COUPLED CLIMATE STUDIES, Glob. Biogeochem. Cycles, 19\(1\),](#)  
3058 [doi:10.1029/2003GB002199](#), 2005.

3059 [Lasslop, G., Thonicke, K. and Kloster, S.: SPITFIRE within the MPI Earth system model: Model](#)  
3060 [development and evaluation, J. Adv. Model. Earth Syst., 6\(3\), 740–755, doi:10.1002/2013MS000284,](#)  
3061 [2014.](#)

3062 [Lauderdale, J. M., Garabato, A. C. N., Oliver, K. I. C., Follows, M. J. and Williams, R. G.: Wind-driven](#)  
3063 [changes in Southern Ocean residual circulation, ocean carbon reservoirs and atmospheric CO<sub>2</sub>, Clim.](#)  
3064 [Dyn., 41\(7\), 2145–2164, doi:10.1007/s00382-012-1650-3](#), 2013.

3065 [Laufkötter, C., John, J. G., Stock, C. A. and Dunne, J. P.: Temperature and oxygen dependence of the](#)  
3066 [rem mineralization of organic matter, Glob. Biogeochem. Cycles, 31\(7\), 1038–1050,](#)  
3067 [doi:10.1002/2017GB005643](#), 2017.

3068 [Law, R. M., Ziehn, T., Matear, R. J., Lenton, A., Chamberlain, M. A., Stevens, L. E., Wang, Y.-P.,](#)  
3069 [Srbinovsky, J., Bi, D., Yan, H. and Vohralik, P. F.: The carbon cycle in the Australian Community Climate](#)  
3070 [and Earth System Simulator \(ACCESS-ESM1\) – Part 1: Model description and pre-industrial simulation,](#)  
3071 [Geosci. Model Dev., 10\(7\), 2567–2590, doi:10.5194/gmd-10-2567-2017](#), 2017.

3072 [Lawrence, D. M., Fisher, R. A., Koven, C. D., Oleson, K. W., Swenson, S. C., Bonan, G., Collier, N., Ghimire,](#)  
3073 [B., van Kampenhout, L., Kennedy, D., Kluzek, E., Lawrence, P. J., Li, F., Li, H., Lombardozzi, D., Riley, W. J.,](#)  
3074 [Sacks, W. J., Shi, M., Vertenstein, M., Wieder, W. R., Xu, C., Ali, A. A., Badger, A. M., Bisht, G., van den](#)  
3075 [Broeke, M., Brunke, M. A., Burns, S. P., Buzan, J., Clark, M., Craig, A., Dahlin, K., Drewniak, B., Fisher, J.](#)  
3076 [B., Flanner, M., Fox, A. M., Gentine, P., Hoffman, F., Keppel-Aleks, G., Knox, R., Kumar, S., Lenaerts, J.,](#)  
3077 [Leung, L. R., Lipscomb, W. H., Lu, Y., Pandey, A., Pelletier, J. D., Perket, J., Randerson, J. T., Ricciuto, D.](#)

3078 [M., Sanderson, B. M., Slater, A., Subin, Z. M., Tang, J., Thomas, R. Q., Val Martin, M. and Zeng, X.: The](#)  
 3079 [Community Land Model Version 5: Description of New Features, Benchmarking, and Impact of Forcing](#)  
 3080 [Uncertainty, J. Adv. Model. Earth Syst., 11\(12\), 4245–4287, doi:10.1029/2018MS001583, 2019.](#)

3081 [Li, W., Zhang, Y., Shi, X., Zhou, W., Huang, A., Mu, M., Qiu, B. and Ji, J.: Development of Land Surface](#)  
 3082 [Model BCC AVIM2.0 and Its Preliminary Performance in LS3MIP/CMIP6, J. Meteorol. Res., 33\(5\), 851–](#)  
 3083 [869, doi:10.1007/s13351-019-9016-y, 2019.](#)

3084 [Lin, S.-J.: A “Vertically Lagrangian” Finite-Volume Dynamical Core for Global Models, Mon. Weather Rev.,](#)  
 3085 [132\(10\), 2293–2307, doi:10.1175/1520-0493\(2004\)132<2293:AVLFDC>2.0.CO;2, 2004.](#)

3086 [MacDougall, A. H.: The Transient Response to Cumulative CO2 Emissions: a Review, Curr. Clim. Change](#)  
 3087 [Rep., 2\(1\), 39–47, doi:10.1007/s40641-015-0030-6, 2016.](#)

3088 [Madec, G., Romain, B.-B., Pierre-Antoine, B., Clément, B., Diego, B., Daley, C., Jérôme, C., Emanuela, C.,](#)  
 3089 [Andrew, C., Damiano, D., Christian, E., Simona, F., Tim, G., James, H., Doroteaciro, I., Dan, L., Claire, L.,](#)  
 3090 [Tomas, L., Nicolas, M., Sébastien, M., Silvia, M., Julien, P., Clément, R., Dave, S., Andrea, S. and Martin,](#)  
 3091 [V.: NEMO ocean engine., 2017.](#)

3092 [Maher, N., Milinski, S., Suarez-Gutierrez, L., Botzet, M., Dobrynin, M., Kornblueh, L., Kröger, J., Takano,](#)  
 3093 [Y., Ghosh, R., Hedemann, C., Li, C., Li, H., Manzini, E., Notz, D., Putrasahan, D., Boysen, L., Claussen, M.,](#)  
 3094 [Ilyina, T., Olonscheck, D., Raddatz, T., Stevens, B. and Marotzke, J.: The Max Planck Institute Grand](#)  
 3095 [Ensemble: Enabling the Exploration of Climate System Variability, J. Adv. Model. Earth Syst., 11\(7\),](#)  
 3096 [2050–2069, doi:10.1029/2019MS001639, 2019.](#)

3097 [Maier-Reimer, E., Kriest, I., Segsneider, J. and Wetzol, P.: The HAMBURG Ocean Carbon Cycle Model](#)  
 3098 [HAMOCC5.1 - Technical De- scription Release 1.1, Max Planck Institute for Meteorology, Hamburg,](#)  
 3099 [Germany, 50 pp., 2005.](#)

3100 [Mann, G. W., Carslaw, K. S., Spracklen, D. V., Ridley, D. A., Manktelow, P. T., Chipperfield, M. P.,](#)  
 3101 [Pickering, S. J. and Johnson, C. E.: Description and evaluation of GLOMAP-mode: a modal global aerosol](#)  
 3102 [microphysics model for the UKCA composition-climate model, Geosci. Model Dev., 3\(2\), 519–551,](#)  
 3103 [doi:10.5194/gmd-3-519-2010, 2010.](#)

3104 [Martin, G. M., Milton, S. F., Senior, C. A., Brooks, M. E., Ineson, S., Reichler, T. and Kim, J.: Analysis and](#)  
 3105 [Reduction of Systematic Errors through a Seamless Approach to Modeling Weather and Climate, J. Clim.,](#)  
 3106 [23\(22\), 5933–5957, doi:10.1175/2010JCLI3541.1, 2010.](#)

3107 [Martin, G. M., Bellouin, N., Collins, W. J., Culverwell, I. D., Halloran, P. R., Hardiman, S. C., Hinton, T. J.,](#)  
 3108 [Jones, C. D., McDonald, R. E., McLaren, A. J., O’Connor, F. M., Roberts, M. J., Rodriguez, J. M.,](#)  
 3109 [Woodward, S., Best, M. J., Brooks, M. E., Brown, A. R., Butchart, N., Dearden, C., Derbyshire, S. H.,](#)  
 3110 [Dharssi, I., Doutriaux-Boucher, M., Edwards, J. M., Falloon, P. D., Gedney, N., Gray, L. J., Hewitt, H. T.,](#)  
 3111 [Hobson, M., Huddleston, M. R., Hughes, J., Ineson, S., Ingram, W. J., James, P. M., Johns, T. C., Johnson,](#)  
 3112 [C. E., Jones, A., Jones, C. P., Joshi, M. M., Keen, A. B., Liddicoat, S., Lock, A. P., Maidens, A. V., Manners, J.](#)  
 3113 [C., Milton, S. F., Rae, J. G. L., Ridley, J. K., Sellar, A., Senior, C. A., Totterdell, I. J., Verhoef, A., Vidale, P. L.](#)  
 3114 [and Wiltshire, A.: The HadGEM2 family of Met Office Unified Model climate configurations, Geosci.](#)  
 3115 [Model Dev., doi:10.5194/gmd-4-723-2011, 2011.](#)

3116 [Martin, J. H., Knauer, G. A., Karl, D. M. and Broenkow, W. W.: VERTEX: carbon cycling in the northeast](#)  
 3117 [Pacific, Deep Sea Res. Part Oceanogr. Res. Pap., 34\(2\), 267–285, doi:https://doi.org/10.1016/0198-](#)  
 3118 [0149\(87\)90086-0, 1987.](#)

3119 [Mathiot, P., Jenkins, A., Harris, C. and Madec, G.: Explicit representation and parametrised impacts of](#)  
 3120 [under ice shelf seas in the  \$\Sigma^{\text{ast}}\$  coordinate ocean model NEMO 3.6, Geosci. Model Dev., 10\(7\),](#)  
 3121 [2849–2874, doi:10.5194/gmd-10-2849-2017, 2017.](#)

3122 [Matthews, H. D., Gillett, N. P., Stott, P. A. and Zickfeld, K.: The proportionality of global warming to](#)  
 3123 [cumulative carbon emissions, Nature, 459\(7248\), 829–832, doi:10.1038/nature08047, 2009.](#)

3124 [Mauritsen, T., Bader, J., Becker, T., Behrens, J., Bittner, M., Brokopf, R., Brovkin, V., Claussen, M.,](#)  
 3125 [Crueger, T., Esch, M., Fast, I., Fiedler, S., Fläschner, D., Gayler, V., Giorgetta, M., Goll, D. S., Haak, H.,](#)  
 3126 [Hagemann, S., Hedemann, C., Hohenegger, C., Ilyina, T., Jahns, T., Jimenéz-de-la-Cuesta, D., Jungclaus, J.,](#)  
 3127 [Kleinen, T., Kloster, S., Kracher, D., Kinne, S., Kleberg, D., Lasslop, G., Kornblueh, L., Marotzke, J., Matei,](#)  
 3128 [D., Meraner, K., Mikolajewicz, U., Modali, K., Möbis, B., Müller, W. A., Nabel, J. E. M. S., Nam, C. C. W.,](#)  
 3129 [Notz, D., Nyawira, S.-S., Paulsen, H., Peters, K., Pincus, R., Pohlmann, H., Pongratz, J., Popp, M., Raddatz,](#)  
 3130 [T. J., Rast, S., Redler, R., Reick, C. H., Rohrschneider, T., Schemann, V., Schmidt, H., Schnur, R.,](#)  
 3131 [Schulzweida, U., Six, K. D., Stein, L., Stemmler, I., Stevens, B., von Storch, J.-S., Tian, F., Voigt, A., Vrese,](#)  
 3132 [P., Wieners, K.-H., Wilkenskield, S., Winkler, A. and Roeckner, E.: Developments in the MPI-M Earth](#)  
 3133 [System Model version 1.2 \(MPI-ESM1.2\) and Its Response to Increasing CO<sub>2</sub>, J. Adv. Model. Earth Syst.,](#)  
 3134 [11\(4\), 998–1038, doi:10.1029/2018MS001400, 2019.](#)

3135 [Millar, R., Allen, M., Rogelj, J. and Friedlingstein, P.: The cumulative carbon budget and its implications,](#)  
 3136 [Oxf. Rev. Econ. Policy, 32\(2\), 323–342, doi:10.1093/oxrep/grw009, 2016.](#)

3137 [Millar, R. J., Fuglestedt, J. S., Friedlingstein, P., Rogelj, J., Grubb, M. J., Matthews, H. D., Skeie, R. B.,](#)  
 3138 [Forster, P. M., Frame, D. J. and Allen, M. R.: Emission budgets and pathways consistent with limiting](#)  
 3139 [warming to 1.5 °C, Nat. Geosci., 10, 741, 2017.](#)

3140 [Milly, P. C. D., Malyshev, S. L., Shevliakova, E., Dunne, K. A., Findell, K. L., Gleeson, T., Liang, Z., Philipps,](#)  
 3141 [P., Stouffer, R. J. and Swenson, S.: An Enhanced Model of Land Water and Energy for Global Hydrologic](#)  
 3142 [and Earth-System Studies, J. Hydrometeorol., 15\(5\), 1739–1761, doi:10.1175/JHM-D-13-0162.1, 2014.](#)

3143 [Morgenstern, O., Braesicke, P., O'Connor, F. M., Bushell, A. C., Johnson, C. E., Osprey, S. M. and Pyle, J.](#)  
 3144 [A.: Evaluation of the new UKCA climate-composition model – Part 1: The stratosphere, Geosci. Model](#)  
 3145 [Dev., 2\(1\), 43–57, doi:10.5194/gmd-2-43-2009, 2009.](#)

3146 [Morgenstern, O., Hegglin, M. I., Rozanov, E., O'Connor, F. M., Abraham, N. L., Akiyoshi, H., Archibald, A.](#)  
 3147 [T., Bekki, S., Butchart, N., Chipperfield, M. P., Deushi, M., Dhomse, S. S., Garcia, R. R., Hardiman, S. C.,](#)  
 3148 [Horowitz, L. W., Jöckel, P., Josse, B., Kinnison, D., Lin, M., Mancini, E., Manyin, M. E., Marchand, M.,](#)  
 3149 [Marécal, V., Michou, M., Oman, L. D., Pitari, G., Plummer, D. A., Revell, L. E., Saint-Martin, D., Schofield,](#)  
 3150 [R., Stenke, A., Stone, K., Sudo, K., Tanaka, T. Y., Tilmes, S., Yamashita, Y., Yoshida, K. and Zeng, G.:](#)  
 3151 [Review of the global models used within phase 1 of the Chemistry–Climate Model Initiative \(CCMI\),](#)  
 3152 [Geosci. Model Dev., 10\(2\), 639–671, doi:10.5194/gmd-10-639-2017, 2017.](#)

3153 [Norby, R. J. and Zak, D. R.: Ecological Lessons from Free-Air CO<sub>2</sub> Enrichment \(FACE\) Experiments, Annu.](#)  
 3154 [Rev. Ecol. Evol. Syst., 42\(1\), 181–203, doi:10.1146/annurev-ecolsys-102209-144647, 2011.](#)

3155 [O'Connor, F. M., Johnson, C. E., Morgenstern, O., Abraham, N. L., Braesicke, P., Dalvi, M., Folberth, G. A.,](#)  
 3156 [Sanderson, M. G., Telford, P. J., Voulgarakis, A., Young, P. J., Zeng, G., Collins, W. J. and Pyle, J. A.:](#)  
 3157 [Evaluation of the new UKCA climate-composition model – Part 2: The Troposphere, Geosci. Model Dev.,](#)  
 3158 [7\(1\), 41–91, doi:10.5194/gmd-7-41-2014, 2014.](#)

3159 [Oke, P. R., Griffin, D. A., Schiller, A., Matear, R. J., Fiedler, R., Mansbridge, J., Lenton, A., Cahill, M.,](#)  
 3160 [Chamberlain, M. A. and Ridgway, K.: Evaluation of a near-global eddy-resolving ocean model, Geosci.](#)  
 3161 [Model Dev., 6\(3\), 591–615, doi:10.5194/gmd-6-591-2013, 2013.](#)

3162 [Orr, J. C. and Epitalon, J.-M.: Improved routines to model the ocean carbonate system: mocsy 2.0,](#)  
 3163 [Geosci. Model Dev., 8\(3\), 485–499, doi:10.5194/gmd-8-485-2015, 2015.](#)

3164 [Orr, J. C., Najjar, R. G., Aumont, O., Bopp, L., Bullister, J. L., Danabasoglu, G., Doney, S. C., Dunne, J. P.,](#)  
 3165 [Dutay, J.-C., Graven, H., Griffies, S. M., John, J. G., Joos, F., Levin, I., Lindsay, K., Matear, R. J., McKinley,](#)  
 3166 [G. A., Mouchet, A., Oschlies, A., Romanou, A., Schlitzer, R., Tagliabue, A., Tanhua, T. and Yool, A.:](#)  
 3167 [Biogeochemical protocols and diagnostics for the CMIP6 Ocean Model Intercomparison Project \(OMIP\),](#)  
 3168 [Geosci. Model Dev., 10\(6\), 2169–2199, doi:10.5194/gmd-10-2169-2017, 2017.](#)

3169 [Parton, W. J., Stewart, J. W. B. and Cole, C. V.: Dynamics of C, N, P and S in grassland soils: a model,](#)  
 3170 [Biogeochemistry, 5\(1\), 109–131, doi:10.1007/BF02180320, 1988.](#)

3171 [Paulsen, H., Ilyina, T., Six, K. D. and Stemmler, I.: Incorporating a prognostic representation of marine](#)  
 3172 [nitrogen fixers into the global ocean biogeochemical model HAMOCC, J. Adv. Model. Earth Syst., 9\(1\),](#)  
 3173 [438–464, doi:10.1002/2016MS000737, 2017.](#)

3174 [Plattner, G.-K., Knutti, R., Joos, F., Stocker, T. F., von Bloh, W., Brovkin, V., Cameron, D., Driesschaert, E.,](#)  
 3175 [Dutkiewicz, S., Eby, M., Edwards, N. R., Fichefet, T., Hargreaves, J. C., Jones, C. D., Loutre, M. F.,](#)  
 3176 [Matthews, H. D., Mouchet, A., Müller, S. A., Nawrath, S., Price, A., Sokolov, A., Strassmann, K. M. and](#)  
 3177 [Weaver, A. J.: Long-Term Climate Commitments Projected with Climate–Carbon Cycle Models, J. Clim.,](#)  
 3178 [21\(12\), 2721–2751, doi:10.1175/2007JCLI1905.1, 2008.](#)

3179 [Prentice, I. C., Cramer, W., Harrison, S. P., Leemans, R., Monserud, R. A. and Solomon, A. M.: A Global](#)  
 3180 [Biome Model Based on Plant Physiology and Dominance, Soil Properties and Climate, J. Biogeogr., 19\(2\),](#)  
 3181 [117–134, 1992.](#)

3182 [Qian, H., Joseph, R. and Zeng, N.: Enhanced terrestrial carbon uptake in the Northern High Latitudes in](#)  
 3183 [the 21st century from the Coupled Carbon Cycle Climate Model Intercomparison Project model](#)  
 3184 [projections, Glob. Change Biol., 16\(2\), 641–656, doi:10.1111/j.1365-2486.2009.01989.x, 2010.](#)

3185 [Rabin, S. S., Ward, D. S., Malyshev, S. L., Magi, B. I., Shevliakova, E. and Pacala, S. W.: A fire model with](#)  
 3186 [distinct crop, pasture, and non-agricultural burning: use of new data and a model-fitting algorithm for](#)  
 3187 [FINAL1, Geosci. Model Dev., 11\(2\), 815–842, doi:10.5194/gmd-11-815-2018, 2018.](#)

3188 [Reick, C. H., Raddatz, T., Brovkin, V. and Gayler, V.: Representation of natural and anthropogenic land](#)  
 3189 [cover change in MPI-ESM, J. Adv. Model. Earth Syst., 5\(3\), 459–482, doi:10.1002/jame.20022, 2013.](#)

3190 [Ridley, J. K., Blockley, E. W., Keen, A. B., Rae, J. G. L., West, A. E. and Schroeder, D.: The sea ice model](#)  
 3191 [component of HadGEM3-GC3.1, Geosci. Model Dev., 11\(2\), 713–723, doi:10.5194/gmd-11-713-2018,](#)  
 3192 [2018.](#)

3193 [Rio, C. and Hourdin, F.: A Thermal Plume Model for the Convective Boundary Layer: Representation of](#)  
 3194 [Cumulus Clouds, \*J. Atmospheric Sci.\*, 65\(2\), 407–425, doi:10.1175/2007JAS2256.1, 2008.](#)

3195 [Rio, C., Hourdin, F., Couvreur, F. and Jam, A.: Resolved Versus Parametrized Boundary-Layer Plumes.](#)  
 3196 [Part II: Continuous Formulations of Mixing Rates for Mass-Flux Schemes, \*Bound.-Layer Meteorol.\*,](#)  
 3197 [135\(3\), 469–483, doi:10.1007/s10546-010-9478-z, 2010.](#)

3198 [Rogelj, J., Shindell, D., Jiang, K., Fifita, S., Forster, P., Ginzburg, V., Handa, C., Kheshgi, H., Kobayashi, S.,](#)  
 3199 [Kriegler, E., Mundaca, L., Seferian, R. and Vilarino, M. V.: Mitigation Pathways Compatible With 1.5°C in](#)  
 3200 [the Context of Sustainable Development., 2018.](#)

3201 [Rogelj, J., Forster, P. M., Kriegler, E., Smith, C. J. and Séférian, R.: Estimating and tracking the remaining](#)  
 3202 [carbon budget for stringent climate targets, \*Nature\*, 571\(7765\), 335–342, doi:10.1038/s41586-019-](#)  
 3203 [1368-z, 2019.](#)

3204 [Rousset, C., Vancoppenolle, M., Madec, G., Fichet, T., Flavoni, S., Barthélemy, A., Benshila, R., Chanut,](#)  
 3205 [J., Levy, C., Masson, S. and Vivier, F.: The Louvain-La-Neuve sea ice model LIM3.6: global and regional](#)  
 3206 [capabilities, \*Geosci. Model Dev.\*, 8\(10\), 2991–3005, doi:10.5194/gmd-8-2991-2015, 2015.](#)

3207 [Roy, T., Bopp, L., Gehlen, M., Schneider, B., Cadule, P., Frölicher, T. L., Segschneider, J., Tjiputra, J.,](#)  
 3208 [Heinze, C. and Joos, F.: Regional Impacts of Climate Change and Atmospheric CO<sub>2</sub> on Future Ocean](#)  
 3209 [Carbon Uptake: A Multimodel Linear Feedback Analysis, \*J. Clim.\*, 24\(9\), 2300–2318,](#)  
 3210 [doi:10.1175/2010JCLI3787.1, 2011.](#)

3211 [Salas Mélia, D.: A global coupled sea ice–ocean model, \*Ocean Model.\*, 4\(2\), 137–172,](#)  
 3212 [doi:https://doi.org/10.1016/S1463-5003\(01\)00015-4, 2002.](#)

3213 [von Salzen, K., Scinocca, J. F., McFarlane, N. A., Li, J., Cole, J. N. S., Plummer, D., Versegny, D., Reader, M.](#)  
 3214 [C., Ma, X., Lazare, M. and Solheim, L.: The Canadian Fourth Generation Atmospheric Global Climate](#)  
 3215 [Model \(CanAM4\). Part I: Representation of Physical Processes, \*Atmosphere-Ocean\*, 51\(1\), 104–125,](#)  
 3216 [doi:10.1080/07055900.2012.755610, 2013.](#)

3217 [Schwinger, J. and Tjiputra, J.: Ocean Carbon Cycle Feedbacks Under Negative Emissions, \*Geophys. Res.\*](#)  
 3218 [Lett., 45\(10\), 5062–5070, doi:10.1029/2018GL077790, 2018.](#)

3219 [Schwinger, J., Tjiputra, J. F., Heinze, C., Bopp, L., Christian, J. R., Gehlen, M., Ilyina, T., Jones, C. D., Salas-](#)  
 3220 [Mélia, D., Segschneider, J., Séférian, R. and Totterdell, I.: Nonlinearity of ocean carbon cycle](#)  
 3221 [feedbacks in CMIP5 earth system models, \*J. Clim.\*, doi:10.1175/JCLI-D-13-00452.1, 2014.](#)

3222 [Schwinger, J., Goris, N., Tjiputra, J. F., Kriest, I., Bentsen, M., Bethke, I., Ilıcak, M., Assmann, K. M. and](#)  
 3223 [Heinze, C.: Evaluation of NorESM-OC \(versions 1 and 1.2\), the ocean carbon-cycle stand-alone](#)  
 3224 [configuration of the Norwegian Earth System Model \(NorESM1\), \*Geosci. Model Dev.\*, 9\(8\), 2589–2622,](#)  
 3225 [doi:10.5194/gmd-9-2589-2016, 2016.](#)

3226 [Séférian, R., Delire, C., Decharme, B., Voldoire, A., Salas y Melia, D., Chevallier, M., Saint-Martin, D.,](#)  
 3227 [Aumont, O., Calvet, J.-C., Carrer, D., Douville, H., Franchistéguy, L., Joetzier, E. and Sénési, S.:](#)  
 3228 [Development and evaluation of CNRM Earth system model – CNRM-ESM1, \*Geosci. Model Dev.\*, 9\(4\),](#)  
 3229 [1423–1453, doi:10.5194/gmd-9-1423-2016, 2016.](#)

3230 [Séférián, R., Nabat, P., Michou, M., Saint-Martin, D., Voldoire, A., Colin, J., Decharme, B., Delire, C.,](#)  
 3231 [Berthet, S., Chevallier, M., Sénési, S., Franchisteguy, L., Vial, J., Mallet, M., Joetzjer, E., Geoffroy, O.,](#)  
 3232 [Guérémy, J.-F., Moine, M.-P., Msadek, R., Ribes, A., Rocher, M., Roehrig, R., Salas-y-Méla, D., Sanchez,](#)  
 3233 [E., Terray, L., Valcke, S., Waldman, R., Aumont, O., Bopp, L., Deshayes, J., Éthé, C. and Madec, G.:](#)  
 3234 [Evaluation of CNRM Earth-System model, CNRM-ESM2-1 : role of Earth system processes in present-day](#)  
 3235 [and future climate, J. Adv. Model. Earth Syst., submitted, 2019.](#)

3236 [Sellar, A. A., Jones, C. G., Mulcahy, J., Tang, Y., Yool, A., Wiltshire, A., O'Connor, F. M., Stringer, M., Hill,](#)  
 3237 [R., Palmieri, J., Woodward, S., de Mora, L., Kuhlbrodt, T., Rumbold, S., Kelley, D. I., Ellis, R., Johnson, C.](#)  
 3238 [E., Walton, J., Abraham, N. L., Andrews, M. B., Andrews, T., Archibald, A. T., Berthou, S., Burke, E.,](#)  
 3239 [Blockley, E., Carslaw, K., Dalvi, M., Edwards, J., Folberth, G. A., Gedney, N., Griffiths, P. T., Harper, A. B.,](#)  
 3240 [Hendry, M. A., Hewitt, A. J., Johnson, B., Jones, A., Jones, C. D., Keeble, J., Liddicoat, S., Morgenstern, O.,](#)  
 3241 [Parker, R. J., Predoi, V., Robertson, E., Siahann, A., Smith, R. S., Swaminathan, R., Woodhouse, M. T.,](#)  
 3242 [Zeng, G. and Zerroukat, M.: UKESM1: Description and evaluation of the UK Earth System Model, J. Adv.](#)  
 3243 [Model. Earth Syst., n/a\(n/a\), doi:10.1029/2019MS001739, 2019.](#)

3244 [Sellers, P. J., Bounoua, L., Collatz, G. J., Randall, D. A., Dazlich, D. A., Los, S. O., Berry, J. A., Fung, I.,](#)  
 3245 [Tucker, C. J., Field, C. B. and Jensen, T. G.: Comparison of Radiative and Physiological Effects of Doubled](#)  
 3246 [Atmospheric CO<sub>2</sub> on Climate, Science, 271\(5254\), 1402–1406, doi:10.1126/science.271.5254.1402,](#)  
 3247 [1996.](#)

3248 [Skinner, C. B., Poulsen, C. J., Chadwick, R., Diffenbaugh, N. S. and Fiorella, R. P.: The Role of Plant CO<sub>2</sub>](#)  
 3249 [Physiological Forcing in Shaping Future Daily-Scale Precipitation, J. Clim., 30\(7\), 2319–2340,](#)  
 3250 [doi:10.1175/JCLI-D-16-0603.1, 2017.](#)

3251 [Stock, C. A., Dunne, J. P. and John, J. G.: Drivers of trophic amplification of ocean productivity trends in a](#)  
 3252 [changing climate, Biogeosciences, 11\(24\), 7125–7135, doi:10.5194/bg-11-7125-2014, 2014a.](#)

3253 [Stock, C. A., Dunne, J. P. and John, J. G.: Global-scale carbon and energy flows through the marine](#)  
 3254 [planktonic food web: An analysis with a coupled physical–biological model, Prog. Oceanogr., 120, 1–28,](#)  
 3255 [doi:10.1016/j.pocean.2013.07.001, 2014b.](#)

3256 [Storkey, D., Blaker, A. T., Mathiot, P., Megann, A., Aksenov, Y., Blockley, E. W., Calvert, D., Graham, T.,](#)  
 3257 [Hewitt, H. T., Hyder, P., Kuhlbrodt, T., Rae, J. G. L. and Sinha, B.: UK Global Ocean GO6 and GO7: a](#)  
 3258 [traceable hierarchy of model resolutions, Geosci. Model Dev., 11\(8\), 3187–3213, doi:10.5194/gmd-11-](#)  
 3259 [3187-2018, 2018.](#)

3260 [Sulman, B. N., Shevliakova, E., Brzostek, E. R., Kivlin, S. N., Malyshev, S., Menge, D. N. L. and Zhang, X.:](#)  
 3261 [Diverse Mycorrhizal Associations Enhance Terrestrial C Storage in a Global Model, Glob. Biogeochem.](#)  
 3262 [Cycles, 33\(4\), 501–523, doi:10.1029/2018GB005973, 2019.](#)

3263 [Swart, N. C., Cole, J. N. S., Kharin, V. V., Lazare, M., Scinocca, J. F., Gillett, N. P., Anstey, J., Arora, V.,](#)  
 3264 [Christian, J. R., Hanna, S., Jiao, Y., Lee, W. G., Majaess, F., Saenko, O. A., Seiler, C., Seinen, C., Shao, A.,](#)  
 3265 [Sigmond, M., Solheim, L., von Salzen, K., Yang, D. and Winter, B.: The Canadian Earth System Model](#)  
 3266 [version 5 \(CanESM5.0.3\), Geosci. Model Dev., 12\(11\), 4823–4873, doi:10.5194/gmd-12-4823-2019,](#)  
 3267 [2019.](#)

3268 [Takata, K., Emori, S. and Watanabe, T.: Development of the minimal advanced treatments of surface](#)  
3269 [interaction and runoff, \*Glob. Planet. Change\*, 38\(1\), 209–222, doi:\[https://doi.org/10.1016/S0921-\]\(https://doi.org/10.1016/S0921-8181\(03\)00030-4\)](#)  
3270 [8181\(03\)00030-4, 2003.](#)

3271 [Takemura, T., Okamoto, H., Maruyama, Y., Numaguti, A., Higurashi, A. and Nakajima, T.: Global three-](#)  
3272 [dimensional simulation of aerosol optical thickness distribution of various origins, \*J. Geophys. Res.\*](#)  
3273 [Atmospheres, 105\(D14\), 17853–17873, doi:10.1029/2000JD900265, 2000.](#)

3274 [Tatebe, H., Tanaka, Y., Komuro, Y. and Hasumi, H.: Impact of deep ocean mixing on the climatic mean](#)  
3275 [state in the Southern Ocean, \*Sci. Rep.\*, 8\(1\), 14479, doi:10.1038/s41598-018-32768-6, 2018.](#)

3276 [Tatebe, H., Ogura, T., Nitta, T., Komuro, Y., Ogochi, K., Takemura, T., Sudo, K., Sekiguchi, M., Abe, M.,](#)  
3277 [Saito, F., Chikira, M., Watanabe, S., Mori, M., Hirota, N., Kawatani, Y., Mochizuki, T., Yoshimura, K.,](#)  
3278 [Takata, K., O'ishi, R., Yamazaki, D., Suzuki, T., Kurogi, M., Kataoka, T., Watanabe, M. and Kimoto, M.:](#)  
3279 [Description and basic evaluation of simulated mean state, internal variability, and climate sensitivity in](#)  
3280 [MIROC6, \*Geosci. Model Dev.\*, 12\(7\), 2727–2765, doi:10.5194/gmd-12-2727-2019, 2019.](#)

3281 [Taylor, K. E., Stouffer, R. J. and Meehl, G. A.: An Overview of CMIP5 and the Experiment Design, \*Bull. Am.\*](#)  
3282 [Meteorol. Soc.](#), 93(4), 485–498, doi:10.1175/BAMS-D-11-00094.1, 2012.

3283 [Thornton, P. E., Doney, S. C., Lindsay, K., Moore, J. K., Mahowald, N., Randerson, J. T., Fung, I.,](#)  
3284 [Lamarque, J.-F., Feddes, J. J. and Lee, Y.-H.: Carbon-nitrogen interactions regulate climate-carbon cycle](#)  
3285 [feedbacks: results from an atmosphere-ocean general circulation model, \*Biogeosciences\*, 6\(10\), 2099–](#)  
3286 [2120, doi:10.5194/bg-6-2099-2009, 2009.](#)

3287 [Tijpstra, J. F., Assmann, K., Bentsen, M., Bethke, I., Otter\aa, O. H., Sturm, C. and Heinze, C.: Bergen](#)  
3288 [Earth system model \(BCM-C\): model description and regional climate-carbon cycle feedbacks](#)  
3289 [assessment, \*Geosci. Model Dev.\*, 3\(1\), 123–141, doi:10.5194/gmd-3-123-2010, 2010.](#)

3290 [Tijpstra, J. F., Roelandt, C., Bentsen, M., Lawrence, D. M., Lorentzen, T., Schwinger, J., Seland, Ø. and](#)  
3291 [Heinze, C.: Evaluation of the carbon cycle components in the Norwegian Earth System Model \(NorESM\),](#)  
3292 [Geosci. Model Dev.](#), 6(2), 301–325, doi:10.5194/gmd-6-301-2013, 2013.

3293 [Tijpstra, J. F., Schwinger, J., Bentsen, M., Morée, A. L., Gao, S., Bethke, I., Heinze, C., Goris, N., Gupta, A.,](#)  
3294 [He, Y., Olivie, D., Seland, Ø. and Schulz, M.: Ocean biogeochemistry in the Norwegian Earth System](#)  
3295 [Model version 2 \(NorESM2\), \*Geosci. Model Dev. Discuss.\*, 1–64, doi:10.5194/gmd-2019-347, 2020.](#)

3296 [Valcke, S.: The OASIS3 coupler: a European climate modelling community software, \*Geosci. Model Dev.\*,](#)  
3297 [6\(2\), 373–388, doi:10.5194/gmd-6-373-2013, 2013.](#)

3298 [Vancoppenolle, M., Fichefet, T. and Goosse, H.: Simulating the mass balance and salinity of Arctic and](#)  
3299 [Antarctic sea ice. 2. Importance of sea ice salinity variations, \*Ocean Model.\*, 27\(1\), 54–69,](#)  
3300 [doi:<https://doi.org/10.1016/j.ocemod.2008.11.003>, 2009.](#)

3301 [Versegny, D. L.: The Canadian land surface scheme \(CLASS\): Its history and future, \*Atmosphere-Ocean\*,](#)  
3302 [38\(1\), 1–13, doi:10.1080/07055900.2000.9649637, 2000.](#)

3303 [Walters, D., Baran, A. J., Boutle, I., Brooks, M., Earnshaw, P., Edwards, J., Furtado, K., Hill, P., Lock, A.,](#)  
3304 [Manners, J., Morcrette, C., Mulcahy, J., Sanchez, C., Smith, C., Stratton, R., Tennant, W., Tomassini, L.,](#)



3305 [Van Weverberg, K., Vosper, S., Willett, M., Browse, J., Bushell, A., Carslaw, K., Dalvi, M., Essery, R.,](#)  
 3306 [Gedney, N., Hardiman, S., Johnson, B., Johnson, C., Jones, A., Jones, C., Mann, G., Milton, S., Rumbold,](#)  
 3307 [H., Sellar, A., Ujiie, M., Whittall, M., Williams, K. and Zerroukat, M.: The Met Office Unified Model Global](#)  
 3308 [Atmosphere 7.0/7.1 and JULES Global Land 7.0 configurations, \*Geosci. Model Dev.\*, \*\*12\*\*\(5\), 1909–1963,](#)  
 3309 [doi:10.5194/gmd-12-1909-2019, 2019.](#)

3310 [Wang, Y. P., Law, R. M. and Pak, B.: A global model of carbon, nitrogen and phosphorus cycles for the](#)  
 3311 [terrestrial biosphere, \*Biogeosciences\*, \*\*7\*\*\(7\), 2261–2282, doi:10.5194/bg-7-2261-2010, 2010.](#)

3312 [Wang, Y.-P. and Leuning, R.: A two-leaf model for canopy conductance, photosynthesis and partitioning](#)  
 3313 [of available energy I: Model description and comparison with a multi-layered model, \*Agric. For.\*](#)  
 3314 [Meteorol., \*\*91\*\*\(1\), 89–111, doi:https://doi.org/10.1016/S0168-1923\(98\)00061-6, 1998.](#)

3315 [Wanninkhof, R.: Relationship between wind speed and gas exchange over the ocean revisited, \*Limnol.\*](#)  
 3316 [Oceanogr. Methods, \*\*12\*\*\(6\), 351–362, doi:10.4319/lom.2014.12.351, 2014.](#)

3317 [Watanabe, M., Suzuki, T., O’ishi, R., Komuro, Y., Watanabe, S., Emori, S., Takemura, T., Chikira, M.,](#)  
 3318 [Ogura, T., Sekiguchi, M., Takata, K., Yamazaki, D., Yokohata, T., Nozawa, T., Hasumi, H., Tatebe, H. and](#)  
 3319 [Kimoto, M.: Improved Climate Simulation by MIROC5: Mean States, Variability, and Climate Sensitivity, \*J.\*](#)  
 3320 [Clim., \*\*23\*\*\(23\), 6312–6335, doi:10.1175/2010JCLI3679.1, 2010.](#)

3321 [Watanabe, S., Hajima, T., Sudo, K., Nagashima, T., Takemura, T., Okajima, H., Nozawa, T., Kawase, H.,](#)  
 3322 [Abe, M., Yokohata, T., Ise, T., Sato, H., Kato, E., Takata, K., Emori, S. and Kawamiya, M.: MIROC-ESM](#)  
 3323 [2010: model description and basic results of CMIP5-20c3m experiments, \*Geosci. Model Dev.\*, \*\*4\*\*, 845–](#)  
 3324 [872, 2011.](#)

3325 [Weng, E. S., Malyshev, S., Lichstein, J. W., Farrior, C. E., Dybzinski, R., Zhang, T., Shevliakova, E. and](#)  
 3326 [Pacala, S. W.: Scaling from individual trees to forests in an Earth system modeling framework using a](#)  
 3327 [mathematically tractable model of height-structured competition, \*Biogeosciences\*, \*\*12\*\*\(9\), 2655–2694,](#)  
 3328 [doi:10.5194/bg-12-2655-2015, 2015.](#)

3329 [Wenzel, S., Cox, P. M., Eyring, V. and Friedlingstein, P.: Emergent constraints on climate-carbon cycle](#)  
 3330 [feedbacks in the CMIP5 Earth system models, \*J. Geophys. Res. Biogeosciences\*, \*\*119\*\*\(5\), 794–807,](#)  
 3331 [doi:10.1002/2013JG002591, 2014.](#)

3332 [Wieder, W. R., Lawrence, D. M., Fisher, R. A., Bonan, G. B., Cheng, S. J., Goodale, C. L., Grandy, A. S.,](#)  
 3333 [Koven, C. D., Lombardozzi, D. L., Oleson, K. W. and Thomas, R. Q.: Beyond Static Benchmarking: Using](#)  
 3334 [Experimental Manipulations to Evaluate Land Model Assumptions, \*Glob. Biogeochem. Cycles\*, \*\*33\*\*\(10\),](#)  
 3335 [1289–1309, doi:10.1029/2018GB006141, 2019.](#)

3336 [Williams, K. D., Copsey, D., Blockley, E. W., Bodas-Salcedo, A., Calvert, D., Comer, R., Davis, P., Graham,](#)  
 3337 [T., Hewitt, H. T., Hill, R., Hyder, P., Ineson, S., Johns, T. C., Keen, A. B., Lee, R. W., Megann, A., Milton, S.](#)  
 3338 [F., Rae, J. G. L., Roberts, M. J., Scaife, A. A., Schiemann, R., Storkey, D., Thorpe, L., Watterson, I. G.,](#)  
 3339 [Walters, D. N., West, A., Wood, R. A., Woollings, T. and Xavier, P. K.: The Met Office Global Coupled](#)  
 3340 [Model 3.0 and 3.1 \(GC3.0 and GC3.1\) Configurations, \*J. Adv. Model. Earth Syst.\*, \*\*10\*\*\(2\), 357–380,](#)  
 3341 [doi:10.1002/2017MS001115, 2018.](#)

3342 [Williams, R. G. and Follows, M. J.: \*Ocean Dynamics and the Carbon Cycle: Principles and Mechanisms,\*](#)  
 3343 [Cambridge University Press., 2011.](#)

Williams, R. G., Goodwin, P., Roussenov, V. M. and Bopp, L.: A framework to understand the transient climate response to emissions, *Environ. Res. Lett.*, 11(1), 015003, doi:10.1088/1748-9326/11/1/015003, 2016.

Williams, R. G., Roussenov, V., Goodwin, P., Resplandy, L. and Bopp, L.: Sensitivity of Global Warming to Carbon Emissions: Effects of Heat and Carbon Uptake in a Suite of Earth System Models, *J. Clim.*, 30(23), 9343–9363, doi:10.1175/JCLI-D-16-0468.1, 2017.

Williams, R. G., Katavouta, A. and Goodwin, P.: Carbon-cycle feedbacks operating in the climate system, *Curr. Clim. Change Rep.*, 5(4), 282–295, doi:10.1007/s40641-019-00144-9, 2019.

Wu, T., Yu, R., Zhang, F., Wang, Z., Dong, M., Wang, L., Jin, X., Chen, D. and Li, L.: The Beijing Climate Center atmospheric general circulation model: description and its performance for the present-day climate, *Clim. Dyn.*, 34(1), 123–147, doi:10.1007/s00382-008-0487-2, 2008.

Wu, T., Li, W., Ji, J., Xin, X., Li, L., Wang, Z., Zhang, Y., Li, J., Zhang, F., Wei, M., Shi, X., Wu, F., Zhang, L., Chu, M., Jie, W., Liu, Y., Wang, F., Liu, X., Li, Q., Dong, M., Liang, X., Gao, Y. and Zhang, J.: Global carbon budgets simulated by the Beijing Climate Center Climate System Model for the last century, *J. Geophys. Res. Atmospheres*, 118(10), 4326–4347, doi:10.1002/jgrd.50320, 2013.

Wu, T., Lu, Y., Fang, Y., Xin, X., Li, L., Li, W., Jie, W., Zhang, J., Liu, Y., Zhang, L., Zhang, F., Zhang, Y., Wu, F., Li, J., Chu, M., Wang, Z., Shi, X., Liu, X., Wei, M., Huang, A., Zhang, Y. and Liu, X.: The Beijing Climate Center Climate System Model (BCC-CSM): the main progress from CMIP5 to CMIP6, *Geosci. Model Dev.*, 12(4), 1573–1600, doi:10.5194/gmd-12-1573-2019, 2019.

Wullschlegel, S. D., Epstein, H. E., Box, E. O., Euskirchen, E. S., Goswami, S., Iversen, C. M., Kattge, J., Norby, R. J., van Bodegom, P. M. and Xu, X.: Plant functional types in Earth system models: past experiences and future directions for application of dynamic vegetation models in high-latitude ecosystems, *Ann. Bot.*, 114(1), 1–16, doi:10.1093/aob/mcu077, 2014.

Yamada, T.: Simulations of Nocturnal Drainage Flows by a q2l Turbulence Closure Model, *J. Atmospheric Sci.*, 40(1), 91–106, doi:10.1175/1520-0469(1983)040<0091:SONDFB>2.0.CO;2, 1983.

Yin, X.: Responses of leaf nitrogen concentration and specific leaf area to atmospheric CO<sub>2</sub> enrichment: a retrospective synthesis across 62 species, *Glob. Change Biol.*, 8(7), 631–642, doi:10.1046/j.1365-2486.2002.00497.x, 2002.

Yool, A., Popova, E. E. and Anderson, T. R.: MEDUSA-2.0: an intermediate complexity biogeochemical model of the marine carbon cycle for climate change and ocean acidification studies, *Geosci. Model Dev.*, 6(5), 1767–1811, doi:10.5194/gmd-6-1767-2013, 2013.

Yoshikawa, C., Kawamiya, M., Kato, T., Yamanaka, Y. and Matsuno, T.: Geographical distribution of the feedback between future climate change and the carbon cycle, *J. Geophys. Res. Biogeosciences*, 113(G3), doi:10.1029/2007JG000570, 2008.

Zhao, M., Golaz, J.-C., Held, I. M., Guo, H., Balaji, V., Benson, R., Chen, J.-H., Chen, X., Donner, L. J., Dunne, J. P., Dunne, K., Durachta, J., Fan, S.-M., Freidenreich, S. M., Garner, S. T., Ginoux, P., Harris, L. M., Horowitz, L. W., Krasting, J. P., Langenhorst, A. R., Liang, Z., Lin, P., Lin, S.-J., Malyshev, S. L., Mason, E., Milly, P. C. D., Ming, Y., Naik, V., Paulot, F., Paynter, D., Philipps, P., Radhakrishnan, A., Ramaswamy,

3382 [V., Robinson, T., Schwarzkopf, D., Seman, C. J., Shevliakova, E., Shen, Z., Shin, H., Silvers, L. G., Wilson, J.](#)  
3383 [R., Winton, M., Wittenberg, A. T., Wyman, B. and Xiang, B.: The GFDL Global Atmosphere and Land](#)  
3384 [Model AM4.0/LM4.0: 1. Simulation Characteristics With Prescribed SSTs, J. Adv. Model. Earth Syst.,](#)  
3385 [10\(3\), 691–734, doi:10.1002/2017MS001208, 2018.](#)

3386 [Zickfeld, K., Eby, M., Matthews, H. D., Schmittner, A. and Weaver, A. J.: Nonlinearity of Carbon Cycle](#)  
3387 [Feedbacks, J. Clim., 24\(16\), 4255–4275, doi:10.1175/2011JCLI3898.1, 2011.](#)

3388 [Ziehn, T., Lenton, A., Law, R. M., Matear, R. J. and Chamberlain, M. A.: The carbon cycle in the Australian](#)  
3389 [Community Climate and Earth System Simulator \(ACCESS-ESM1\) – Part 2: Historical simulations, Geosci.](#)  
3390 [Model Dev., 10\(7\), 2591–2614, doi:10.5194/gmd-10-2591-2017, 2017.](#)

3391

3392



Page 2: [1] Deleted	Arora,Vivek [CCCMA]	06/04/2020 11:04:00 AM
---------------------	---------------------	------------------------

Page 2: [1] Deleted	Arora,Vivek [CCCMA]	06/04/2020 11:04:00 AM
---------------------	---------------------	------------------------

Page 2: [1] Deleted	Arora,Vivek [CCCMA]	06/04/2020 11:04:00 AM
---------------------	---------------------	------------------------

Page 2: [1] Deleted	Arora,Vivek [CCCMA]	06/04/2020 11:04:00 AM
---------------------	---------------------	------------------------

Page 2: [1] Deleted	Arora,Vivek [CCCMA]	06/04/2020 11:04:00 AM
---------------------	---------------------	------------------------

Page 2: [1] Deleted	Arora,Vivek [CCCMA]	06/04/2020 11:04:00 AM
---------------------	---------------------	------------------------

Page 2: [1] Deleted	Arora,Vivek [CCCMA]	06/04/2020 11:04:00 AM
---------------------	---------------------	------------------------

Page 2: [1] Deleted	Arora,Vivek [CCCMA]	06/04/2020 11:04:00 AM
---------------------	---------------------	------------------------

Page 2: [1] Deleted	Arora,Vivek [CCCMA]	06/04/2020 11:04:00 AM
---------------------	---------------------	------------------------

Page 2: [1] Deleted	Arora,Vivek [CCCMA]	06/04/2020 11:04:00 AM
---------------------	---------------------	------------------------

Page 2: [1] Deleted	Arora,Vivek [CCCMA]	06/04/2020 11:04:00 AM
---------------------	---------------------	------------------------

Page 2: [2] Formatted	Arora,Vivek [CCCMA]	21/04/2020 2:42:00 PM
-----------------------	---------------------	-----------------------

Font: 11 pt, Superscript

Page 2: [2] Formatted	Arora,Vivek [CCCMA]	21/04/2020 2:42:00 PM
-----------------------	---------------------	-----------------------

Font: 11 pt, Superscript

Page 74: [3] Deleted	Arora,Vivek [CCCMA]	19/03/2020 12:48:00 PM
----------------------	---------------------	------------------------

Figures 6 and 7 provide justification for using the BGC-COU approach, over the RAD-BGC and RAD-COU approaches, in calculating the feedback parameters as discussed below. In Figure 7, the absolute magnitude of  $\gamma_0$  when using the BGC-COU approach is about twice in CMIP5 models (and more than three times in CMIP6 models) compared to its model-mean value calculated using

the RAD-BGC and RAD-COU approaches. The reason for this is that the RAD simulation misses the suppression (due to weakening of the ocean circulation) of carbon drawdown to the deep ocean. This is because there is no buildup of a strong carbon gradient from the atmosphere to the deep ocean in the RAD simulation. This process is important when climate change is forced by increasing atmospheric CO<sub>2</sub>, and therefore feedback parameters calculated using the BGC-COU approach are more likely to include all processes relevant to application for realistic scenarios. In Figure 6, although the carbon-climate feedback parameter over land ( $\gamma_L$ ) is larger in absolute amount, it is comparatively less sensitive to the approach used, than over ocean, because over land an increase in temperature not only increases the respiratory losses but also affects photosynthetic processes especially in conjunction with increasing CO<sub>2</sub>. Warmer temperatures increase photosynthesis over mid to high latitude regions where photosynthesis is currently limited by temperature and more so with increasing CO<sub>2</sub>, but decrease photosynthesis over tropical regions where the temperatures are already too warm for optimal photosynthesis. The net result of these compensating processes plays out very differently in different models and in the model-mean sense this results in less sensitivity of the calculated value of carbon climate feedback parameter over land ( $\gamma_L$ ) to the different approaches than over ocean. This is seen in both CMIP5 and CMIP6 models. When  $\gamma_L$  is calculated using the RAD-BGC and RAD-COU approaches, it is exclusively calculated using results from the RAD simulation. However, since over land photosynthesis is also affected by temperature in addition to respiration (with widely varying responses between models) the  $\gamma_L$  values vary widely between models between the RAD-BGC/RAD-COU approach and the BGC-COU approach. This is seen, for example, for ACCESS-ESM1.5, IPSL, and CanESM5 models in Figure 6b. The very different values of  $\gamma_L$  for individual

models, when using different approaches to calculate them, are the result of the differing responses of the vegetation and soil+litter carbon pools, in the RAD and COU simulations, and this is supported by results that were presented in Section 4.3.2.